

Diss. ETH No. 13469

# **QUANTITATIVE STRAIN ANALYSIS WITH IMAGE SHEARING SPECKLE PATTERN INTERFEROMETRY (SHEAROGRAPHY)**

A dissertation submitted to the  
SWISS FEDERAL INSTITUTE OF TECHNOLOGY ZURICH

for the degree of  
Doctor of Technical Sciences

presented by  
Stephan Peter Waldner  
Dipl. Masch.-Ing. ETH  
born December 11, 1967  
citizen of Basel and Oberdorf (BL)

accepted on the recommendation of  
Prof. Dr. Paolo Ermanni, examiner  
Prof. Dr. Jürg Dual, co-examiner  
Prof. Dr. Pierre Jacquot, co-examiner

2000



# ABSTRACT

This thesis reports on the development of a quantitative method for strain analysis. The method is based on image-shearing speckle pattern interferometry, which is also known as shearography.

**Shearography** Shearography is an optical technique to measure the deformation of object surfaces. Its principal field of application is qualitative non-destructive testing, e.g. to find defects in structures made from composite materials. Shearography is less susceptible to environmental vibrations than electronic speckle pattern interferometry (ESPI) or holographic interferometry. Furthermore, shearography allows for the adjustment of the measurement sensitivity without changing the optical set-up or the laser wavelength.

The goal of this work is to develop shearography into a method for quantitative strain analysis. This development implies a theoretical analysis of shearography, a concept for the extraction of the strains from the measured images, the implementation of image processing routines, and the design of specific measurement equipment.

**Theoretical analysis** For the theoretical analysis, the relation between measured phase change and mechanical deformation is derived for a general shearography set-up and the simplifications made in the derivation are identified and analysed.

**Image processing** In order to extract the strain components from the measured images, the following image processing techniques are needed: Calculation of the phase from the intensity measurements, filtering of the phase fringe patterns, phase unwrapping, removal of the image doubling, isolation of the directional components, and the quantitative evaluation of the strain fields. A new filter technique – the multiply repeated anisotropic sine/cosine average filter – is introduced and compared with other advanced filter techniques, clearly showing the superiority of the new filter. Another new image processing technique presented herein calculates the displacement field from the original phase map that represents an approximation to the displacement derivative. This procedure takes into account the finite character of the shear distance and removes its image-doubling effect. Shearography measurements usually contain a combination of directional components of the deformation according to the directions of illumination and observation. It is shown here that from three measurements – each with a different illumination direction – it is possible to isolate the directional components of deformation. With the light sources arranged in a specific symmetry and plane wave illumination, this isolation is particularly simple.

**Specific equipment** In order to have a practical system to perform the strain measurement, a special shearography system has been designed. It consists of a compact shearography head and three illumination modules. The system is remotely controlled from the computer.

**Experimental verification** The developed measurement technique, the equipment, and the image processing are verified by means of an exemplary measurement. The strains on the surface of a flat tensile specimen with symmetric notches is determined and the results are compared with the strain distributions calculated with the finite element method.

**Results** The image processing methods developed in this work are verified individually and show a very good performance. In the final experiment for strain measurement, where all processing steps are combined, the result for the largest strain component is acceptable. The peak value is measured with an accuracy of 6 % and in the rest of the sample the strain lies within the expected range. Still, disturbances, which result from the evaluation procedure, do not allow for the accurate determination of the local strain distributions. For the other strain components, the disturbances cover the wanted strain information.

Although the accuracy and reliability of the developed strain measurement method is not yet satisfactory, this work shows the feasibility of quantitative strain analysis with shearography and provides all important tools to perform and evaluate the measurements.

# KURZFASSUNG

Diese Arbeit berichtet über die Entwicklung einer quantitativen Methode zur Dehnungsanalyse. Die Methode basiert auf der bildscherenden Specklemuster-Interferometrie, die auch unter dem Namen 'Shearographie' bekannt ist.

**Shearographie** Shearographie ist eine optische Technik zur Messung von Verformungen der Objektoberfläche. Ihr Hauptanwendungsgebiet ist die qualitative zerstörungsfreie Prüfung, z.B. das Auffinden von Defekten in Strukturen aus Verbundwerkstoffen. Shearographie ist weniger empfindlich gegenüber Vibrationen der Umgebung als die elektronische Specklemuster-Interferometrie oder die holographische Interferometrie. Zudem erlaubt die Shearographie die Anpassung der Messempfindlichkeit ohne Aenderung des optischen Aufbaus oder der Wellenlänge des Lasers.

Das Ziel dieser Arbeit ist es, die Shearographie zu einer Methode für die quantitative Dehnungsanalyse zu entwickeln. Diese Entwicklung beinhaltet eine theoretische Analyse der Shearographie, ein Konzept zur Ermittlung der Dehnungen aus den gemessenen Bildern, die Realisierung von Bildverarbeitungs-Routinen sowie die Konstruktion einer spezifischen Messausrüstung.

**Theoretische Analyse** Bei der theoretischen Analyse wird die Beziehung zwischen der gemessenen Phasenänderung und der mechanischen Verformung für einen allgemeinen Shearographie-Aufbau hergeleitet und die in der Herleitung enthaltenen Vereinfachungen werden identifiziert und analysiert.

**Bildverarbeitung** Um die Dehnungskomponenten aus den gemessenen Bildern zu ermitteln, werden folgende Bildverarbeitungstechniken benötigt: Berechnung der Phase aus den Intensitätsmessungen, Filterung der Phasenstreifenbilder, Phasenfaltung, Entfernung der Bildverdopplung, Isolation der Richtungskomponenten und die quantitative Auswertung der Dehnungsfelder. Eine neue Filtertechnik – das mehrfach wiederholte anisotrope Sinus/Cosinus-Filter – wird eingeführt und mit anderen fortschrittlichen Filtertechniken verglichen, was eine deutliche Ueberlegenheit des neuen Filters zeigt. Eine weitere neue Bildverarbeitungstechnik die hier präsentiert wird berechnet das Verschiebungsfeld aus der ursprünglichen Phasenverteilung, die eine Annäherung an die Verschiebungsableitung darstellt. Diese Prozedur berücksichtigt den finiten Charakter der Sheardistanz und entfernt den Effekt der Bildverdopplung. Shearographie-Messungen beinhalten normalerweise eine Kombination von Richtungskomponenten der Deformation, entsprechend den Beleuchtungs- und Beobachtungsrichtungen. Es wird hier gezeigt, dass es möglich ist aus drei Messungen – jede mit einer anderen Beleuchtungsrichtung – die Richtungskomponenten der Verformung zu isolieren. Wenn die Beleuchtungsquellen in einer bestimmten Symmetrie angeordnet werden und die

Beleuchtung mit ebenen Wellen erfolgt, so wird die Isolation speziell einfach.

**Spezifische Ausrüstung** Um ein praktisches System zur Dehnungsmessung zur Verfügung zu haben, wurde ein spezielles Shearographie-System entwickelt. Es besteht aus einem kompakten Shearographie-Kopf und drei Beleuchtungsmodulen. Das System wird vom Computer ferngesteuert.

**Experiment** Die entwickelte Messtechnik, die Ausrüstung und die Bildverarbeitung werden mit einer beispielhaften Messung verifiziert. Die Dehnungen an der Oberfläche einer Flachzugprobe mit symmetrischen Kerben werden bestimmt und die Resultate werden mit Dehnungsverteilungen verglichen, die mit der Methode der finiten Elemente berechnet wurden.

**Ergebnisse** Die in dieser Arbeit entwickelten Bildverarbeitungsmethoden wurden einzeln verifiziert und zeigen eine sehr gute Leistungsfähigkeit. Beim abschliessenden Experiment, wo alle Verarbeitungsschritte kombiniert werden, ist das Ergebnis für die grösste Dehnungskomponente akzeptabel. Der Spitzenwert wird auf 6 % genau gemessen und auf dem Rest der Probe liegen die Dehnungen im erwarteten Bereich. Störungen, die aus dem Auswertevorgang resultieren, verunmöglichen jedoch eine genaue Bestimmung der lokalen Dehnungsverteilung. Bei den anderen Dehnungskomponenten überdecken die Störungen die gesuchte Dehnungsinformation.

Obwohl die Genauigkeit und Zuverlässigkeit der entwickelten Dehnungsmessmethode noch nicht zufriedenstellend ist, zeigt diese Arbeit die Machbarkeit der quantitativen Dehnungsmessung mit Shearographie und liefert alle wichtigen Werkzeuge um die Messungen durchzuführen und auszuwerten.

# TABLE OF CONTENTS

ABSTRACT . . . . .	iii
KURZFASSUNG . . . . .	v
TABLE OF CONTENTS . . . . .	vii
ACKNOWLEDGEMENTS . . . . .	xi
SYMBOLS AND ABBREVIATIONS . . . . .	xiii
CHAPTER 1: INTRODUCTION . . . . .	1
1.1 Background of this Work . . . . .	1
1.1.1 State of the Art in Strain Measurement . . . . .	1
1.1.2 Historical Development of Shearography . . . . .	4
1.1.3 Shearography Today . . . . .	5
1.2 Goals of this Work . . . . .	5
1.3 Overview . . . . .	6
1.4 Main Achievements . . . . .	9
CHAPTER 2: THEORETICAL ASPECTS . . . . .	11
2.1 A Direct Approach to Speckle Interferometry and Shearography . . . . .	11
2.1.1 Classical Interferometry . . . . .	11
2.1.2 Speckle Interferometry . . . . .	14
2.1.3 Shearography . . . . .	18
2.2 Mechanical Aspects . . . . .	23
2.2.1 Displacement and Strain . . . . .	23
2.2.2 Stress . . . . .	24
2.2.3 What can we Measure? . . . . .	25
CHAPTER 3: PHASE DETERMINATION . . . . .	27
3.1 Temporal Phase Shifting . . . . .	27
3.2 Spatial Phase Shifting . . . . .	30
3.3 Dynamic Phase Shifting . . . . .	32
3.4 Selected Phase Shifting Method . . . . .	33
3.5 Operations with Phase Fringe Patterns . . . . .	34
CHAPTER 4: FILTERING OF PHASE FRINGE PATTERNS AND PHASE UNWRAPPING . . . . .	35
4.1 Introduction . . . . .	35
4.2 Conventional Filter Method . . . . .	37
4.3 Advanced Filter Methods . . . . .	39
4.4 Our Filter Method . . . . .	40
4.5 Conclusions . . . . .	41
4.6 Phase Unwrapping . . . . .	41
CHAPTER 5: REMOVING THE IMAGE DOUBLING . . . . .	45
5.1 Introduction . . . . .	45
5.2 An Illustrative Example . . . . .	47
5.3 Description of the Method . . . . .	48
5.4 Experimental Results . . . . .	50

5.5 Conclusions . . . . .	55
5.6 Alternative Methods . . . . .	55
CHAPTER 6: ISOLATION OF THE COMPONENTS . . . . .	57
6.1 Introduction . . . . .	57
6.2 Description of the Method . . . . .	59
6.3 Experimental Details . . . . .	61
6.4 Results and Discussion . . . . .	62
6.5 Concluding Remarks . . . . .	65
CHAPTER 7: QUANTITATIVE EVALUATION . . . . .	67
7.1 Measurement Strategy . . . . .	67
7.1.1 Two Shear Directions . . . . .	67
7.1.2 One Shear Direction . . . . .	69
7.1.3 Requirements for the Hardware . . . . .	70
7.2 Evaluation Procedure . . . . .	70
7.3 Details of the Evaluation . . . . .	73
7.3.1 Sensitivity Matrix . . . . .	73
7.3.2 Exact Shear Distance . . . . .	74
CHAPTER 8: DEVELOPMENT OF ADAPTED EQUIPMENT . . . . .	77
8.1 Laboratory System . . . . .	77
8.1.1 Optical Arrangement . . . . .	77
8.1.2 Computer Hardware . . . . .	78
8.1.3 Software . . . . .	79
8.1.4 Object Loading Device . . . . .	81
8.1.5 Experience Gained with the Laboratory System . . . . .	81
8.2 Why to Design our own Shearography System. . . . .	82
8.2.1 Requirements for the Shearography System . . . . .	82
8.2.2 Shearography Systems on the Market . . . . .	82
8.3 Realization of the Shearography System . . . . .	84
8.3.1 Concept . . . . .	84
8.3.2 Design of a Compact Shearography Head. . . . .	85
8.3.3 Design of Illumination Modules. . . . .	86
8.3.4 Electronic Control . . . . .	87
8.3.5 Measurement Arrangements. . . . .	88
8.3.6 Hardware and Software . . . . .	90
8.4 Self Developed Software Routines . . . . .	91
8.4.1 Pisa vs. Matlab. . . . .	91
8.4.2 Implementation . . . . .	92
CHAPTER 9: QUANTITATIVE STRAIN ANALYSIS . . . . .	93
9.1 Preliminary Experiments . . . . .	93
9.1.1 Experiments with the Laboratory System . . . . .	93
9.1.2 First Verification of the Shearography System . . . . .	93
9.2 Strain Measurement with the Shearography System . . . . .	95
9.2.1 Description of the Measurement . . . . .	95
9.2.2 Calculated Results . . . . .	97
9.2.3 Results of the Quantitative Evaluation . . . . .	99
9.2.4 Discussion . . . . .	106
9.2.5 Comparison with Other Published Work . . . . .	107



CHAPTER 10: FURTHER APPLICATIONS OF THE DEVELOPED TECHNIQUES . . . . .	109
10.1 Filtering of Phase Fringe Patterns . . . . .	109
10.2 Removing the Image Doubling . . . . .	110
10.3 Quantitative Evaluation . . . . .	111
10.4 Specific Equipment . . . . .	112
CHAPTER 11: CONCLUSIONS . . . . .	113
11.1 Summary of the Main Achievements . . . . .	113
11.1.1 Solution of the Principal Problems. . . . .	113
11.1.2 Concept for Quantitative Strain Analysis . . . . .	114
11.1.3 Development of Specific Equipment. . . . .	114
11.1.4 Experimental Demonstration. . . . .	114
11.2 Comparison with ESPI . . . . .	115
11.3 Further Work. . . . .	115
11.4 Concluding Remark . . . . .	117
CHAPTER 12: REFERENCES . . . . .	119
CURRICULUM VITAE . . . . .	125



# ACKNOWLEDGEMENTS

At this point I would like to thank all of the people who made this work possible:

The principal supervisor and examiner of my thesis, Prof. Dr. Paolo Ermanni, has supported my work and helped me to improve it with his helpful comments. Prof. Dr. Jürg Dual accepted to act as a co-examiner, gave me valuable hints for the concept and the mechanical aspects, and read the manuscript carefully. Prof. Dr. Pierre Jacquot as the second co-examiner made many constructive remarks on my manuscript and helped me to improve this work considerably during the last year of the thesis.

I also thank Prof. Dr. Markus Meier for supporting me during the definition and the starting phase of the project.

I greatly appreciated the good co-operation with the colleagues I had the chance to work with, namely Dr. Gerald Kress, Thierry Floureau, Dr. Manfred Hertwig, Dr. Torsten Flemming, Benno Stäger, Marion Uebersax, Michael Gut, Stefan Brem, Nicolas Goudemand, and Hans-Jörg Lohe. I apprized their scientific proficiency as well as the pleasant and stimulating working atmosphere.

I am especially grateful to Dr. Hubert Aebischer, with whom I worked together most closely. Without the many – sometimes controversial, but always stimulating – discussions, my thesis would look like much different. A good part of this work is the result of our fruitful co-operation and it is also due to him that I considerably improved my scientific writing. Finally, he supported me during the final phase of my thesis by reviewing the manuscript carefully.

Stefan Brem did an excellent job designing the compact shearography head and the electronic control during a student project. Two more students, Daniel Isch and Alessandro Sibilia, performed their student projects under my supervision and contributed greatly to the gain of experience of our group in the field of shearography. Furthermore, I would like to thank Peter Rechsteiner who performed many of the laboratory experiments and documented them in a perfect way.

Many other people at ETH contributed to an excellent environment to perform a Ph.D. work. I am thankful to Dr. Mark Ladd for correcting my English in some of the publications that are contained in this work.

This work was funded by ETH Zurich under grant No. 0-20-117-96 (TH project “Quantitative Dehnungsmessung mit bildscherender Speckle-Muster-Interferometrie”) and also by the Swiss Federal Office for Education and Science (BBW) under grant No. 95.0774 (BRITE-EURAM project BRPR-960152 “Pulsed Digital Holography and Shearography”).

Finally, I would like to especially thank my family and my friends for their patience and the personal support during the past years.

Zurich, December 1999

Stephan Waldner

# SYMBOLS AND ABBREVIATIONS

Symbols Throughout this work, *italics* are used for variables (except for greek letters), and ***bold italics*** are used for vectors.

$\gamma_{xy}, \gamma_{xz}, \gamma_{yz}$	Shearing strains
$\mathbf{d} = (u, v, w)$	Displacement vector
$\Delta \mathbf{d}$	Displacement difference
$\Delta \mathbf{x}$	Shear vector measured on the object surface
$\Delta \xi$	Shear distance in the image
$\Delta \phi$	Phase difference
$E$	Modulus of elasticity in tension (Young's modulus)
$\epsilon_x, \epsilon_y, \epsilon_z$	Unit elongations, strains
$G$	Modulus of elasticity in shear, modulus of rigidity
$\theta_s$	Angle between illumination direction and the $x$ axis
$I_1, I_2$	Intensities of two interfering waves
$I_0, I_m$	Background intensity and modulation
$\mathbf{k} = (k_x, k_y, k_z)$	Sensitivity vector
$\mathbf{k}_o, \mathbf{k}_s$	Wave vectors in observation and illumination direction
$\lambda$	Wavelength of the laser light
$\nu$	Poisson's ratio
$P(x, y)$	Point on the object surface
$\pi$	3.141592654...
$S_1, S_2, S_3$	Location of the sources of illumination
$\sigma_x, \sigma_y, \sigma_z$	Normal stresses
$\tau_{xy}, \tau_{xz}, \tau_{yz}$	Shearing stresses
$x, y, z$	Object co-ordinates, usually with the $z$ axis normal to the object surface
$\xi, \eta$	Image co-ordinates

Abbreviations	CAD	Computer aided design
	CCD	Charge coupled device
	CCIR	Video standard recommended by the 'Comité Consultatif International des Radiocommunications'

D/A	Digital to analog
ESPI	Electronic speckle pattern interferometry
FEM	Finite element method
FFT	Fast fourier transform
HeNe	Helium-Neon
Nd:YVO <sub>4</sub>	Neodymium-doped Yttrium Orthovanadate
PC	Personal computer
RAM	Random access memory

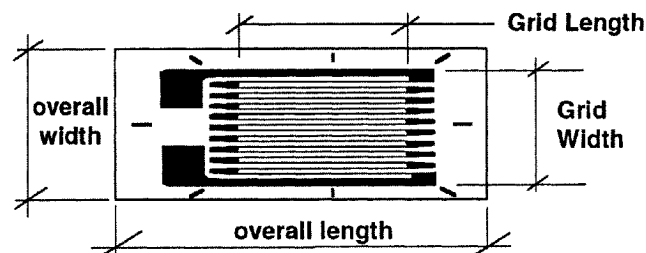
## INTRODUCTION

This first chapter introduces the context of this thesis and the structure of the thesis itself. Starting with strain gauges – the most popular technique to measure strains – different methods for the investigation of object deformation are discussed. Then the development and current status of shearography is outlined. From this basis, the goals of this work are formulated and the research that is necessary to reach the goals. Section 1.3 explains the structure of this thesis and section 1.4 summarizes its main achievements.

### 1.1 Background of this Work

#### 1.1.1 State of the Art in Strain Measurement

Figure 1.1 Geometry of a strain gauge [1].



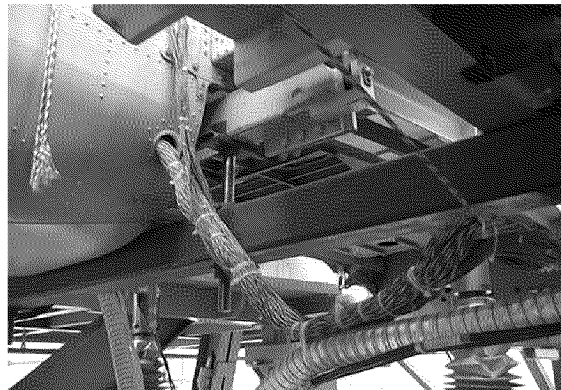
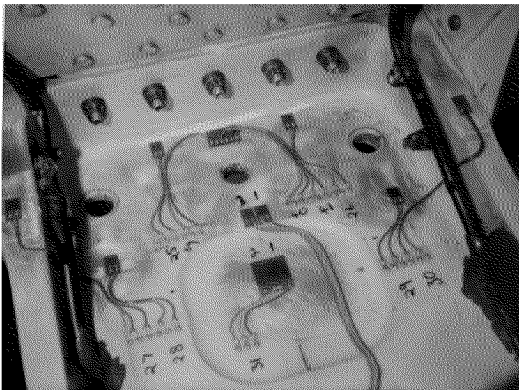
**Strain gauges** By far the most popular method to measure strain today is the application of strain gauges. Strain gauges are in fact electrical resistors, embedded in a thin plastic strip. If it is adequately glued to the surface of the component under test, the length of the strain gauge and — as a consequence — its electrical resistance varies upon deformation of the structure. From the measured change of resistance, the actual strain on the object surface can be calculated using the characteristics of the strain gauge. A large variety of strain gauges are available on the market. Parameters for selecting the suitable type are the gauge length (from miniature gauges up to 100 mm), the gauge pattern (single grid, two or three-element rosette), the resistance (120  $\Omega$  to 5000  $\Omega$ ), the elongation

capability (up to 20%), the fabrication type (semiconductor, foil, wire), and the operating temperature range (-269 °C to 425 °C) [2].

Figure 1.1 shows the geometry of a typical foil strain gauge. The large black areas are the solder tabs for connecting the wires.

- Rosettes** An interesting type is the strain gauge rosette, which consists of three grids and allows to determine the directions and magnitudes of the principal surface strains. Strain gauges are also suited to measure dynamic deformations. In this case, the electrical signal has to be recorded and evaluated over the time of interest.
- Limitations** Strain gauges developed into a useful and well accepted tool to investigate structural behaviour. For the purpose of this work it is, of course, important to point out the limitations and drawbacks of this conventional technique:
- Although considered to be a non-destructive method, strain gauges interfere with the object surface and add material to the object. This technique is therefore not suited for fragile surfaces and highly elastic materials.
  - The measured quantity in fact is not really strain, but the difference of the displacements at both ends of the grid. In other words, the strain is averaged over the grid length.
  - The measurement is relative. Not the effective strain in the material can be measured, but only the difference between the initial state and the loaded state.
  - Strain gauges measure at a distinctive point on the object. If the largest strains have to be determined, the locations of the strain gauges have to be carefully selected, which is not a trivial task for complex structures.
  - Installing strain gauges is difficult and time-consuming. Depending on the adhesive used, a special curing treatment has to be followed before the measurement.

**Figure 1.2** Structural test set-up for an airplane. Strain gauges applied to the surface (left) and cables connecting the strain gauges with the acquisition electronics (right). (Photos courtesy of British Aerospace Structural Testing Facility, Brough, Mr. Mat Manzouri.)





**Application example** An application of strain gauges is shown in figure 1.2. The airplane structure is subjected to loads simulating in-flight conditions and loads during take-off and landing. Besides periodical visual inspection by specialists, the tests are continuously monitored with strain gauges. The large number of strain gauges results in an enormous expenditure of wires and data acquisition electronics.

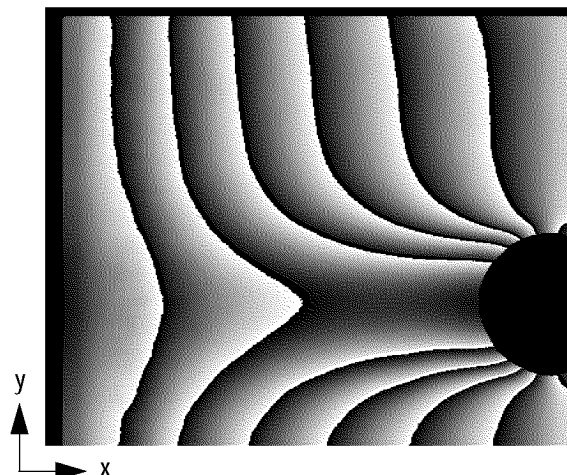
**Other techniques** Other methods like brittle coatings, caustics, projection Moiré, Moiré interferometry, speckle photography, photoelasticity, photoelastic coatings, and fibre optic sensors are also used to measure strain for various applications. A survey of strain measurement methods can be found in [3]. Here, we want to take a closer look at the interferometric techniques holography and electronic speckle pattern interferometry (ESPI) [4, 5].

**Holography and ESPI** Holographic interferometry and ESPI are optical methods to measure displacement fields. Two states of the object – a reference state and a deformed state – are recorded, resulting in a fringe pattern from which the displacement field can be determined. As recording media, holography needs holographic or thermoplastic film, whereas ESPI uses a CCD camera or conventional photographic film. These two methods overcome some of the limitations of the strain gauge technique:

- The measurement is non-contacting and a special preparation of the surface is not necessary.
- The whole imaged surface can be investigated simultaneously and critical locations can be identified without a-priori knowledge.

Figure 1.3 shows the measurement of a flat tensile specimen (containing a hole) with in-plane sensitive ESPI. The fringes display lines of equal displacement  $u$  in  $x$ -direction caused by a load applied to the specimen in the same direction.

**Figure 1.3** In-plane displacement field measured with ESPI.



The quality of the results of this technique has substantially improved in the past years. From our laboratory, Floureaux [6] and Hertwig et al. [7, 8] contributed essentially to this progress. Qualitatively, the strain  $du/dx$  can be estimated from the fringe spacing; high strain occurs where the fringes

are narrow. For a quantitative evaluation, the phase fringe pattern shown in figure 1.3 has to be further processed. This method of strain determination is used in a commercial product to monitor tensile tests on testing machines [9, 10].

Today, ESPI is recognized as a tool for quantitative displacement measurement, whereas the importance of holographic interferometry decreases. The limitations of holography and ESPI are the following:

- Because of their high sensitivity and because the interfering light waves travel along paths that are relatively distant from each other, holography and ESPI are very susceptible to vibrations and air currents. Therefore, measurements are mostly performed in dedicated laboratories with special vibration isolation.
- Holograms have to be recorded on material with a very high spatial resolution. This type of photographic material offers only a low photo-sensitivity, which makes it necessary to use strong lasers or long exposure times. Speckle interferometry does not require special recording material, it works with normal photographic material as well as with electronic cameras.
- The sensitivity is given by the wavelength of the laser and the illumination geometry. With a given optical set-up, the deformation therefore has to be matched to the measurement range, i.e. a load has to be applied that causes a reasonable number of fringes.

*Shearography* is another technique from the family of speckle interferometric methods (see chapter 2 for a description). It is able to alleviate these limitations and forms the basis of this work.

### 1.1.2 Historical Development of Shearography

---

The first publications on shearography date from 1973. Leendertz and Butters entitled their paper ‘An image-shearing speckle-pattern interferometer for measuring bending moments’ [11]. The authors measured the surface slope with shearography and determined the bending moments in a thin plate. In the same year, Hung and Taylor published ‘Speckle-Shearing Interferometric Camera – A Tool for Measurement of Derivatives of Surface Displacement’ [12, 13] presenting a technique to measure displacement derivatives. From 1973 until today, many papers appeared describing applications of this technique to special problems and improvements as well as investigations of the measurement technique itself.

Terminology	Different names appear in literature for the same technique. ‘Image-shearing speckle pattern interferometry’ [11] describes the method most accurately, but more frequent are the terms ‘speckle shearing interferometry’ and ‘shearography’, which was first used by Hung in 1982 [14].
Digital image processing	Initially, the images were recorded on photographic and holographic films. The first publication using an electronic camera and digital image

processing appeared in 1980 [15]. In 1991, Kadono et al. introduced the phase shifting technique in shearography [16].

**Applications** Qualitative detection of flaws is by far the most popular application of shearography. Only a few authors tried to evaluate their experiments quantitatively (e.g. [17, 18, 19]) and these are restricted to simple out-of-plane experiments. Although Hung and Taylor [12, 13] proposed their method for measuring the derivatives of out-of-plane displacement  $w$  as well as in-plane displacements  $u$ ,  $v$ , they did not carry out in-plane measurements. At that time, measurements were recorded on photographic film and the evaluation would have to be done ‘by hand’ and point by point (see also section 6.1). The research focused on the out-of-plane case. In fact, no publication on the measurement of the in-plane displacement derivatives appeared until 1995.

### 1.1.3 Shearography Today

---

**Advantages** Shearography has the same advantages as holographic interferometry and ESPI: it is a non-contacting whole-field technique. Additionally, the interfering light waves travel along almost the same path, which reduces the susceptibility to vibration and noise, relaxes the demand for a long coherence length, and allows for adjusting the measurement sensitivity directly by altering the shear distance. This made shearography a well accepted tool for qualitative non-destructive testing with a wide range of applications in the optical laboratory as well as in industrial environment.

**Industrial applications** Today, various shearography systems for qualitative non-destructive testing are commercially available (see section 8.2.2, “Shearography Systems on the Market”). Additionally, dedicated testing systems based on shearography serve for tyre inspection [26] or for automated testing of helicopter rotor blades and parts of the ARIANE rocket [27, 28].

**Motivation for our work** In a preliminary study, we found it feasible to apply shearography to other fields than qualitative out-of-plane measurements: an automatic quantitative evaluation of the results is possible as well as in-plane measurements. Both combined lead to a technique for strain analysis. This was the motivation to develop shearography into a non-contacting method to measure strains on object surfaces.

## 1.2 Goals of this Work

---

The principal goal is the development and realization of a quantitative strain analysis method based on shearography.

**Strain analysis** With *strain analysis* we mean the determination of the components of surface strain  $\epsilon_x$ ,  $\epsilon_y$ , and  $\gamma_{xy}$  (see section 2.2.1). These are the same components that can be determined with strain gauges or other methods measuring on the surface.

**Quantitative** *Quantitative* here means that the result is a numerical value for every image point and not only a qualitative indication of strain concentrations. In a mathematical sense, a quantitative evaluation would include a

complete error analysis providing the tolerance of the result. Such an error analysis is beyond our goals and therefore not included in this work. In fact, we do not know a publication, where a result of an ESPI or shearography measurement is given with an error tolerance.

Experimental demonstration	Besides the development of the strain analysis method, a further goal is the experimental demonstration of the method. For this demonstration, a prototype system is to be developed, which is optimized for the task of strain measurement.
Research needs	<p>At the beginning of this work, the following problems existed that had to be solved for developing shearography into a method for quantitative strain analysis:</p> <ul style="list-style-type: none"><li>• Theoretical analysis is necessary to define an optimized optical arrangement and evaluation technique in order to obtain accurate quantitative results.</li><li>• Shearography measurements contain a high level of noise, which has to be suppressed for evaluation.</li><li>• Due to the optical arrangement, a doubled image appears in shearography results which not only confuses the observer but also imposes severe problems for the evaluation.</li><li>• The measurement result generally contains a mixture of mechanical quantities. In order to obtain the strain values we are interested in, these have to be isolated from the measurement results.</li></ul>
Experimental approach	In order to reach the goals that are defined above, an experimental approach is chosen. Although a sound theoretical basis is necessary to solve the existing problems, the emphasis of this work lies in the experiments with optical arrangements and image processing functions.

## 1.3 Overview

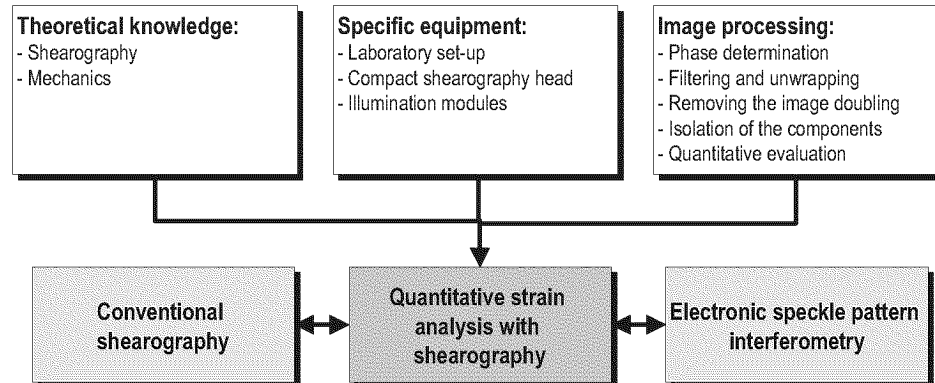
---

The following concept is chosen to reach the aimed goal: First a practical theoretical description of shearography and its relation to the mechanical deformation of the object has to be formulated. From this theoretical formulation, an adapted optical set-up can be developed as well as the image processing that is necessary for the quantitative evaluation. After verifying the general performance of the method by means of a laboratory set-up, a special system is developed. This includes a computer controlled shearography head, illumination modules and the software for evaluating the acquired images. Some software routines can be selected from available ones, others have to be improved or newly developed. Finally, the developed measurement system is verified on a simple test sample and compared with calculations.

**Thesis structure** The work documented in this thesis is structured as shown in figure 1.4. In order to solve the task of quantitative strain analysis with shearography, three main fields have to be mastered, i.e. the *theory*

(chapter 2), the *equipment* (chapter 8), and the *image processing* (chapter 3 to chapter 7).

**Figure 1.4** Structure of the work documented in this thesis.



- Chapter 2 Chapter 2 introduces in its first part the important terms and formulae to explain speckle interferometry and shearography. Then the equation that relates the mechanical deformation of the object with the phase difference measured with shearography is derived and the simplifications made in this derivation are listed. The last part of the chapter is dedicated to basic terms of mechanics, which are important in the context of this work.
- Chapter 3 The purpose of Chapter 3, “Phase Determination”, is to introduce the principal techniques used in speckle interferometry and shearography to determine the phase from the measured intensity images.
- Chapter 4 Chapter 4, “Filtering of Phase Fringe Patterns and Phase Unwrapping” presents the further processing steps of phase fringe patterns for quantitative evaluation. A new filtering technique is presented, which effectively removes the noise, without affecting the details of the fringe pattern. The method is demonstrated on a shearography example and compared with other filtering techniques. The last section of the chapter then explains the process of phase unwrapping.
- Chapter 5 In Chapter 5, “Removing the Image Doubling” a technique that solves the problem of image doubling in shearography is developed. The method calculates the displacement field from the shearography result by taking into account the finite shear distance. Experiments on a simulated as well as on a measured fringe pattern demonstrate the efficiency of this method.
- Chapter 6 Chapter 6, “Isolation of the Components”, presents a simple optical set-up and an associated procedure which allows to accurately isolate all six displacement derivatives which can contribute to the formation of fringes in shearography. The method is demonstrated on the deformation of a rectangular tensile specimen with a central hole. The measured in-plane strain components are qualitatively compared with the results of a finite element analysis. High quality fringe patterns are obtained, which reveal even localized strain concentrations.
- Chapter 7 In the previous chapters, theoretical aspects and various image processing techniques were described, developed, or investigated. These techniques will be adapted in Chapter 7, “Quantitative Evaluation” to reach the goal

of this work, i.e. the quantitative measurement of strains with shearography. First, the strategies to acquire the images that are necessary for the strain measurement are discussed. A method, which records images with two shear directions is compared with a method, which only needs one shear direction and reduces the number of images by a factor of two. Then the evaluation procedure is presented, which extracts the components of strain from the acquired images, and the details of some steps of the evaluation are explained.

- Chapter 8 Chapter 8, “Development of Adapted Equipment” presents and explains in detail the equipment we used for the experiments throughout this work. A first section describes the laboratory system, which is flexible but difficult to handle, and the device for loading tensile specimens. Then, the requirements for a practical 3D shearography system are compiled and the commercially available shearography systems are shortly introduced. The comparison of our requirements with what is available motivates our decision to develop our own shearography system. A description of the developed system consisting of a shearography head and three illumination modules and of the developed electronics and software concludes the chapter.
- Chapter 9 In Chapter 9, “Quantitative Strain Analysis”, the developed measurement equipment, the image processing, and evaluation method are validated with measurements. In a first part of the chapter, the measurements with the laboratory system are briefly reviewed and the ability of the compact shearography system to provide quantitative results is tested on a simple out-of-plane example. In the second part, the quantitative strain analysis is performed with the shearography system. The test sample and the measurement conditions are described. Then, the strain distributions are calculated by finite element analysis for comparison with the measurement. The measured images are processed and quantitatively evaluated, which results in the strain distributions. Finally, the calculated and measured results are compared and discussed.
- Chapter 10 As indicated in the lower part of figure 1.4, the developed methods not only serve for the quantitative strain analysis with shearography, but may also be useful in other applications, e.g. in conventional shearography and in ESPI. Chapter 10, “Further Applications of the Developed Techniques” shows uses of the new filter method, of the removal of the image doubling, of the quantitative evaluation, and of the equipment developed in this work.
- Chapter 11 The “Conclusions” in chapter 11 summarize the main achievements that were realized in this work. Then the advantages and drawbacks of the developed method in comparison with ESPI are discussed. Finally, the points that appeared as being critical are identified and suggestions are made, how the method could be further improved.
- Chapter 12 The references to publications in books, journals and conference proceedings are marked in the text as numbers in square brackets. These references can be found at the end of this work in Chapter 12, “References” on page 119 ff.

## 1.4 Main Achievements

---

The principal achievement of this thesis lies in the realization of a method to quantitatively analyse strain distributions with shearography. In Chapter 7, “Quantitative Evaluation”, we propose a detailed concept for the measurement of the strain components  $\varepsilon_x$ ,  $\varepsilon_y$  and  $\gamma_{xy}$ . Starting from the measured phase images, extensive image processing is necessary to obtain quantitative results. The methods for filtering, for the removal of the image doubling, and the isolation of components, which are developed in the scope of this work, are all integrated in this evaluation procedure. In chapter 9, the strain measurement is performed on a test sample and the result of the evaluation is quantitatively compared with a calculated strain distribution. These first results show that quantitative strain analysis with shearography is feasible.

In order to reach the goal of quantitative strain analysis with shearography, several improvements of existing techniques or new developments were necessary.

- |                             |  |
|-----------------------------|--|
| Theoretical analysis        | The equation relating the mechanical deformation of the object with the phase difference measured with shearography is derived in a new way, opening the door to the accurate analysis of the simplifications contained in this derivation. This theoretical analysis forms the basis for the quantitative evaluation.   |
| Filtering                   | In order to successfully perform the image processing operations necessary for the strain analysis, the measured phase fringe patterns have to contain a maximum of information and a minimum of noise. We have developed a new, highly effective filtering method that leads to clearly better results than the filter methods used so far in speckle interferometry and shearography.  |
| Removing the image doubling | The effect of image doubling, which is caused by the finite image shear, severely impedes the interpretation and evaluation of shearographic measurements. The common way to reduce this effect is to minimize the shear distance, which – on the other hand – also reduces the measurement sensitivity. In chapter 5 we present a new method that calculates the displacement field from a shearography measurement and – at the same time – removes the image doubling. Applying this method facilitates the quantitative evaluation of shearography measurements. |
| Isolation of components     | The isolation of components is also an original work of our group. Shearography was exclusively used for out-of-plane measurements (deformation normal to the object surface). No publication on in-plane measurements has appeared at the time when we developed our method (Chapter 6, “Isolation of the Components”), which allows for the simple determination of in-plane as well as out-of-plane contributions from three measurements.  |
| Quantitative evaluation     | The evaluation of our shearography measurements is not based on a simple estimation of the measurement sensitivity, but takes into account the variation of the sensitivity from pixel to pixel and the amount of  |

shear, i.e. the image doubling. A quantitative evaluation to this depth has not been published before.

**Equipment** The shearography system developed in this work is also innovative. It is the first portable 3D shearography system and all functions – i.e. the adjustment of amount and direction of shear, the switching between the illumination sources, and the phase-shift – are working computer-controlled.

**Software** It is clear that these developments well beyond the state of the art are not achievable by simply applying available software. Many new functions have been programmed to control the shearography system, to record the images, and to process and evaluate them.



## THEORETICAL ASPECTS

The first part of this chapter introduces the important terms and formulae in order to explain speckle interferometry and shearography. Then the equation that relates the mechanical deformation of the object with the phase difference measured with shearography is derived in an elegant way and the simplifications made in this derivation are listed. The last part of this chapter is dedicated to basic terms of mechanics, which are important in the context of this work.

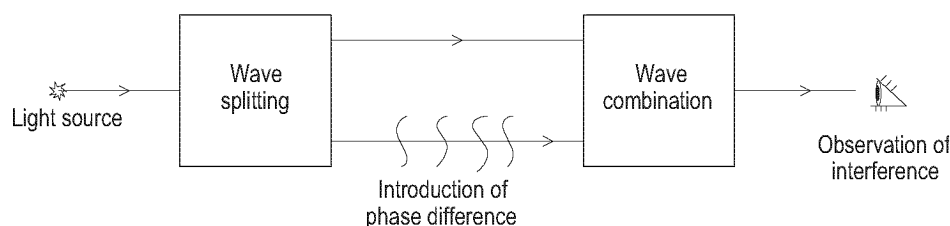
### 2.1 A Direct Approach to Speckle Interferometry and Shearography

In order to understand the theory of shearography, it is useful to know the principles of speckle interferometry. These can be explained with the help of classical interferometry. This section is therefore structured in three parts: *classical interferometry*, *speckle interferometry*, and *shearography*.

General  
interferometer

Figure 2.1 shows the elements of a generalized interferometer. The light emitted by a source of coherent light (i.e. light with the ability to interfere, usually laser light), is split in two waves propagating along different paths. These waves are then combined again causing interference, which is observed by a camera, a detector, or the naked eye.

**Figure 2.1** General scheme of an interferometer [29].



#### 2.1.1 Classical Interferometry

In the Michelson interferometer shown in figure 2.2, the laser beam crosses two lenses which effect a beam expansion. The plane wave generated in this way is then split into two waves by the beamsplitter *BS*.

The first wave is reflected at mirror  $M_1$ , the second at mirror  $M_2$ . Both reflected waves impinge again on the beamsplitter  $BS$ , where they combine again. Part of the light falls on a screen where we can observe the interference (we are not interested in the part of the light travelling back in the direction of the laser).

Intensity The intensity caused by the interference of two waves is given by [29, 30]

$$I = I_1 + I_2 + 2\sqrt{I_1 I_2} \cdot \cos \Delta\phi, \quad (2.1)$$

where  $I_1$  and  $I_2$  are the intensities of the two light waves and  $\Delta\phi$  is the phase difference between the two light paths.

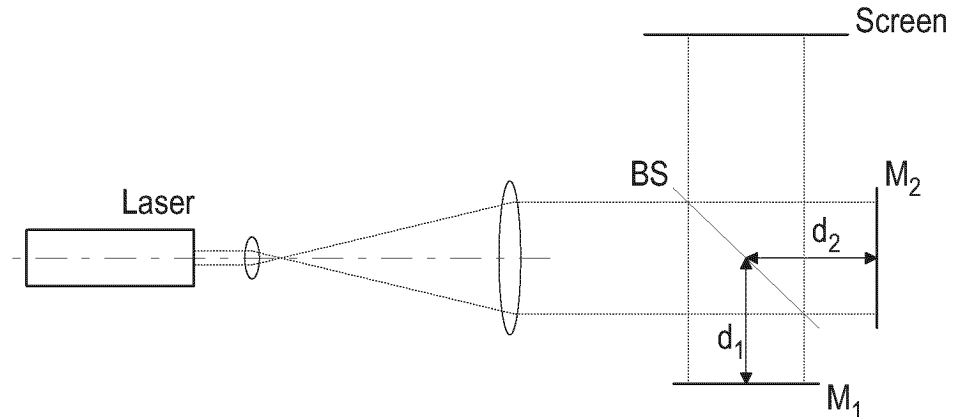
If the Michelson interferometer would be perfectly aligned using perfect lenses, mirrors, an ideal beamsplitter and laser, the interference of the two smooth wavefronts would create a constant intensity across the screen. The phase difference is given by

$$\Delta\phi = 2\pi \cdot \frac{2d_1 - 2d_2}{\lambda}, \quad (2.2)$$

with  $\lambda$  being the laser wavelength. The intensities  $I_1$  and  $I_2$  can be determined by blocking the other arm of the interferometer. For equal intensities  $I_1 = I_2$  and equal distances  $d_1 = d_2$  (i.e.  $\Delta\phi = 0$ ) we obtain

$$I = 4I_1. \quad (2.3)$$

**Figure 2.2** Michelson interferometer with collimated illumination.



Constructive/  
destructive  
interference

If we now translate one of the mirrors so that the phase difference  $\Delta\phi = \pi$ , the intensity  $I$  in eq. (2.1) is zero. Translating the mirror further in the same direction, we will observe maximum intensity again when  $\Delta\phi = 2\pi$ . This occurrence of maximum intensity is called *constructive interference* and appears provided that

$$\Delta\phi = 2n\pi; n \in Z. \quad (2.4)$$

*Destructive interference*, where the intensity is zero, occurs when

$$\Delta\phi = (2n + 1) \cdot \pi; n \in Z. \quad (2.5)$$

Coherence length With a real laser source, the number  $n$  is limited by the coherence length of the laser [29]. If the path difference between the two arms of the interferometer exceeds the coherence length, interference occurs no longer and the intensity remains constant at  $I = 2I_1$ .

Shape measurement If we replace one of the plane mirrors in the well balanced Michelson interferometer by a spherical mirror, we do not observe a constant intensity  $I$  across the screen, but concentric *fringes* as shown in figure 2.3. The difference in shape  $\Delta z$  between the flat mirror and the spheric mirror causes a phase difference

$$\Delta\varphi = \frac{2\pi}{\lambda} \cdot 2\Delta z. \quad (2.6)$$

According to eq. (2.1), this effects the intensity distribution visible on the screen.

**Figure 2.3** Simulated interferogram from a Michelson interferometer with one plane and one spherical mirror. The image size is 50 mm  $\times$  50 mm, the radius of the sphere is 100 m and  $\lambda = 632.8$  nm (HeNe laser).

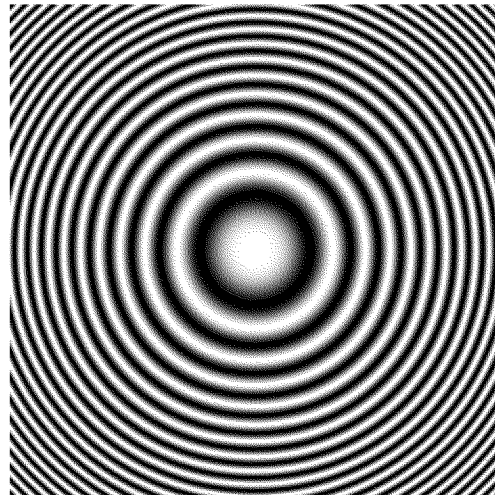
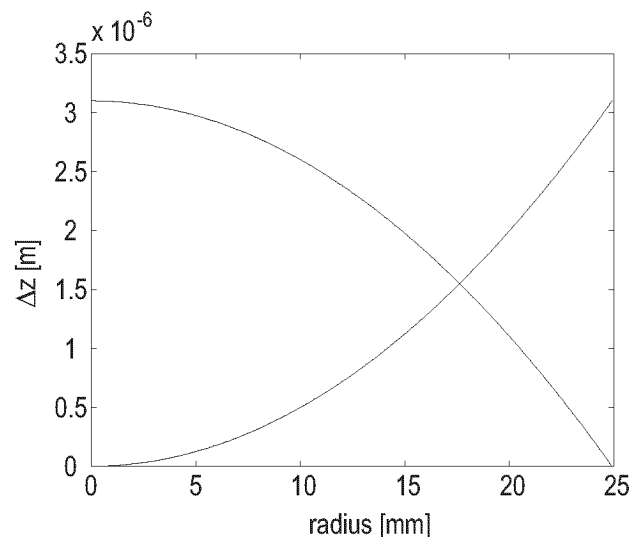


**Figure 2.4** Evaluation of figure 2.3 along a radius. The mirror shape can not be determined unambiguously [31].



**Quantitative Evaluation** Figure 2.4 shows an attempt to quantitatively evaluate the interference pattern along the radius. Since we know that  $\Delta\phi$  from one fringe to the neighbouring one is equal to  $\pm 2\pi$ , we can determine  $\Delta z$  across the mirror (intermediate phase values are determined by the inverse cosine operation). But as we have no information about the sign of the phase difference, both shapes shown in figure 2.4 are possible: a convex and a concave mirror. By recording three or more interferograms with one mirror translated by defined steps between the measurements, it is possible to determine the phase unambiguously. This ‘temporal phase shifting technique’ is described in section 3.1.

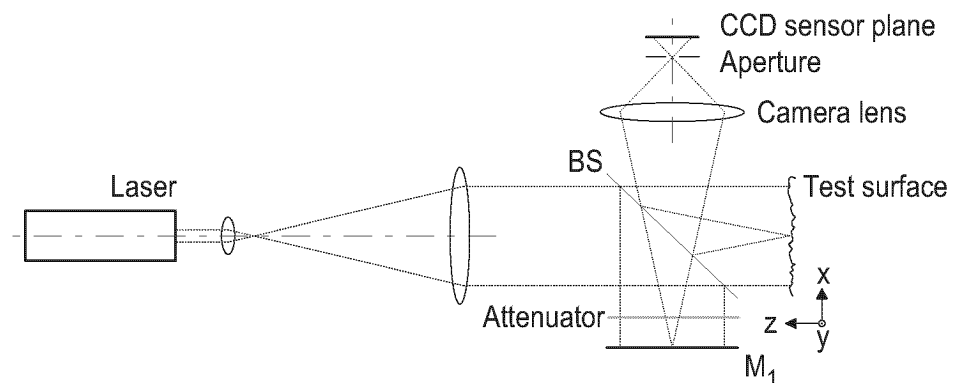
**Applications** With this method it is therefore possible to measure the shape and quality (e.g. flatness, roughness) of a surface. As the wavelength of laser light lies in the order of magnitude of  $0.5 \mu\text{m}$ , the method is very sensitive – too sensitive for many industrial applications. Additionally, it is necessary to work with smooth wave fronts, which limits the application of this classical interferometry to objects with polished surfaces like optical mirrors and lenses.

Now we go a step further from optical elements producing smooth wavefronts to objects with a rough surface, and hence the step from *classical interferometry* to *speckle interferometry*.

## 2.1.2 Speckle Interferometry

We change the interferometer set-up as shown in figure 2.5. We replace the spherical mirror by an *optically rough* test surface. Optically rough means that the surface roughness is in the order of magnitude of the laser wavelength or larger [32], which is the case for most surfaces in technical applications as well as in nature. May it be machined metals, fibre-reinforced plastics, wood or concrete structures, all of them exhibit an optically rough surface.

**Figure 2.5** Simple speckle interferometer. The surface of the test object is optically rough.

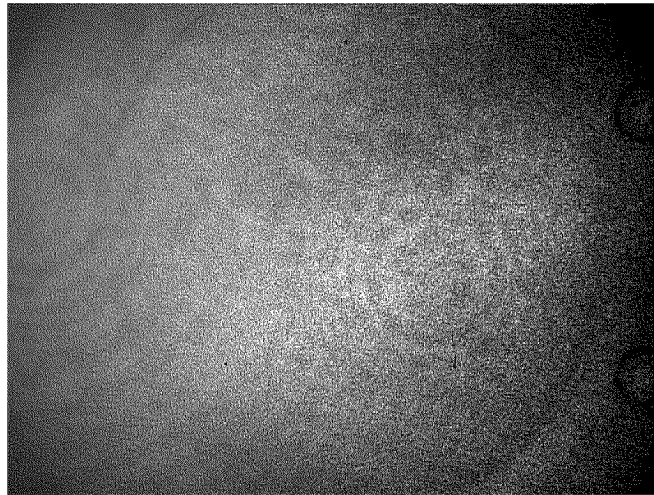


Since the intensity of the reflection of such a surface is much smaller than the specular reflection of the mirror, an attenuator is inserted in front of  $M_1$ . Instead of the screen, we use an electronic camera with a lens, which images the test surface onto the sensor plane of the camera.

**Speckles** The image seen by the camera is no longer a smooth interferogram (figure 2.3), but a *speckle pattern* as shown in figure 2.6.

Considered as a distribution of intensity, a speckle pattern appears as a set of small, random, uncorrelated areas of fluctuating intensity. The same is true for the distribution of the phase of the speckle pattern. Intensity and phase are statistically independent distributions. These fluctuations are caused by the random interference of multiple light waves reflected from a large number of points on the object surface – i.e. the points which are unresolved because of the finite aperture of the imaging system [33].

**Figure 2.6** Image of a circular plate with an optically rough surface. The reflected laser light produces a speckle pattern in the image plane of the camera.



Such a speckle pattern (consisting of many speckles) can not be treated analytically, but only with statistical methods. In that way it is possible to determine the distributions of intensity, phase, and size of the speckles. The average speckle size  $d_s$  is given by [32]

$$d_s = 1.22 \cdot \frac{\lambda z}{a}, \quad (2.7)$$

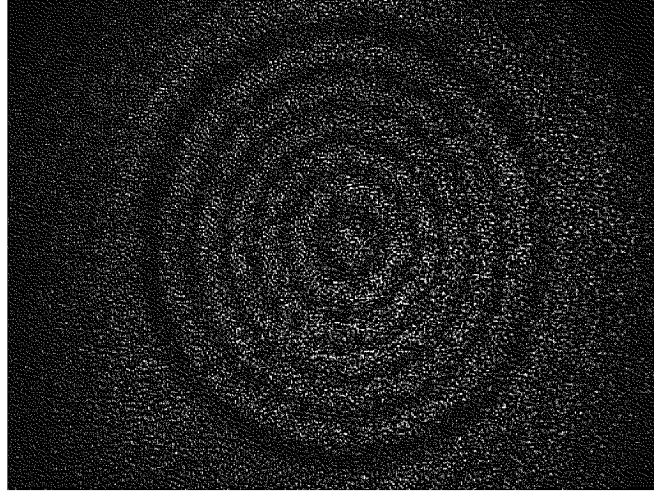
where  $z$  is the distance between lens and image plane and  $a$  is the diameter of the lens aperture. This formula shows that a reduction of the aperture leads to larger speckles and vice versa. Further details about speckles and their properties can be found in literature [32, 34, 35, 36].

**Correlation** It is clear that a single speckle pattern does not show the information we are interested in, i.e. the deformation of the object or its surface shape. But we can use such a pattern for measurement purposes, if we *correlate* it with a speckle pattern recorded under slightly modified conditions. The modification consists of a deformation of the test object, a change in the optical set-up (e.g. illumination angle), the laser frequency, or the refractive index in the optical path.

Figure 2.7 shows the result of the correlation (here a subtraction of the intensity values with subsequent scaling) of two speckle patterns. Between the recording of the images, the object – a clamped circular plate

– was deformed by applying a load in the centre of the plate normal to its surface. The fringes show places of equal out-of-plane displacement.

**Figure 2.7** Correlation of two speckle patterns recorded before and after loading of a circular plate. The fringes represent places of equal out-of-plane displacement.



**Phase change** In eq. (2.6) we determined the *phase difference* in the classical interferogram, which is defined by the difference of the path lengths in the interferometer. In the speckle interferometry experiment, we are interested in the *phase change* between the two object states. For a speckle interferometer with one laser wave, illuminating the object, and a reference wave (*single beam illumination*), the phase change is [37, 4, 34]

$$\Delta\varphi = (\mathbf{k}_o - \mathbf{k}_s) \cdot \mathbf{d}, \quad (2.8)$$

where  $\mathbf{k}_o$  and  $\mathbf{k}_s$  are the *wave vectors* – i.e. vectors oriented in direction of light propagation with length  $2\pi/\lambda$  – in observation and illumination direction, respectively.

$$\mathbf{d} = [u \ v \ w] \quad (2.9)$$

is the *displacement vector* of the object surface. Of course, these variables are functions of the position in the image and therefore of the coordinates  $x,y,z$  of the object surface (or  $x,y$  if we consider nearly flat objects). In the set-up shown in figure 2.5,

$$\mathbf{k}_o = \frac{2\pi}{\lambda} \cdot [0 \ 0 \ 1] \text{ and } \mathbf{k}_s = \frac{2\pi}{\lambda} \cdot [0 \ 0 \ -1] \quad (2.10)$$

for all  $x,y$ . Thus eq. (2.8) simplifies to

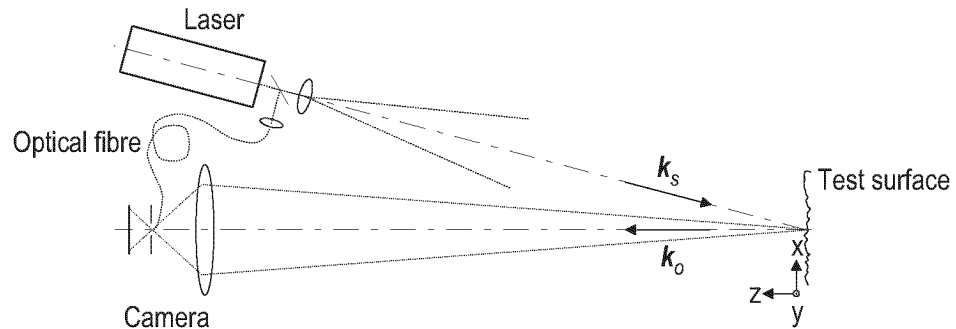
$$\Delta\varphi = \frac{2\pi}{\lambda} \cdot 2w. \quad (2.11)$$

The phase change is therefore proportional to the displacement in  $z$  direction, the so-called *out-of-plane* direction.

Out-of-plane  
speckle  
interferometer

An alternative set-up for the measurement of out-of-plane displacements is shown in figure 2.8. Here the reference wave is coupled into an optical fibre and guided to the aperture of the camera, where it interferes with the light reflected from the object surface. This design allows for an integration of all optical elements in one housing and is hence suitable for compact portable systems.

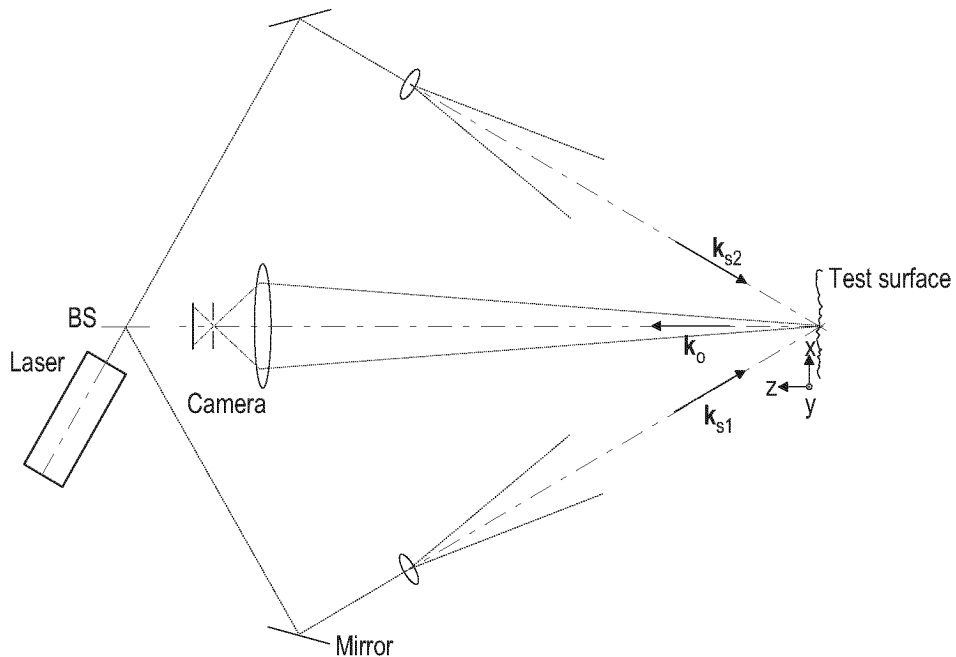
**Figure 2.8** Speckle interferometer for out-of-plane measurements. The reference wave is guided through an optical fibre to the camera aperture.



In-plane  
speckle  
interferometer

In contrast to the previous set-ups (figure 2.5 and figure 2.8), where we can distinguish between an object and a reference wave, this is not the case in the set-up shown in figure 2.9. Both interfering waves are reflected at the object surface and we therefore observe interference between two speckle fields (*two-beam illumination*).

**Figure 2.9** Speckle interferometer for the measurement of in-plane displacements.



The phase change measured with this kind of speckle interferometer is given by [37, 4, 34]

$$\Delta\varphi = (\mathbf{k}_{s1} - \mathbf{k}_{s2}) \cdot \mathbf{d}, \quad (2.12)$$

where  $\mathbf{k}_{s1}$  and  $\mathbf{k}_{s2}$  are the wave vectors of the two illumination directions. With symmetric illumination, the out-of-plane component cancels out,

which allows for the measurement of the *in-plane* component of the displacement.

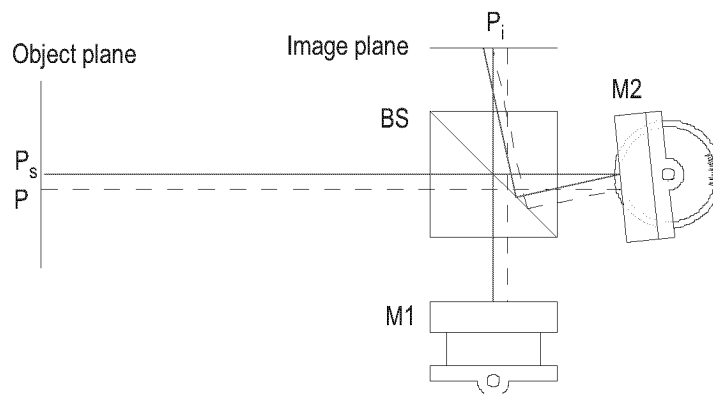
**3D systems** Today, commercial ESPI systems are available that incorporate an out-of-plane and two in-plane interferometers. With such a system, the three-dimensional displacement field can be determined, i.e. the components  $u$ ,  $v$ , and  $w$  of the displacement vector  $d$ .

For both out-of-plane and in-plane ESPI, the light of the illuminating laser is split and travels along different paths before reaching the image plane. The optical length of these paths has to be balanced such that the difference lies within the coherence length of the laser. The different paths are also responsible for the susceptibility of ESPI to vibrations, noise, and air currents. Here shearography shows a clear advantage: The illuminating light is *not* split; the light reflected from the object is split only near the camera.

### 2.1.3 Shearography

**Optical set-up** The main difference between the optical set-up for shearography and the speckle interferometers described above is that shearography uses a single illumination beam and no reference beam. The interference is created in the observing part of the set-up and not in the illuminating part. An ‘image-shearing device’, located between object and camera, superposes two laterally sheared images of the object. This effects that the light reflected from two object points with a certain *shear* between them interferes in one image point. This image shear can be realized in different ways, e.g. by positioning a glass wedge in front of half of the camera lens [39], or by using a double aperture [40].

**Figure 2.10** The effect of image shearing with the Michelson interferometer. The light from the object points  $P$  and  $P_s$  is interfering in the same point  $P_i$  in the image plane.



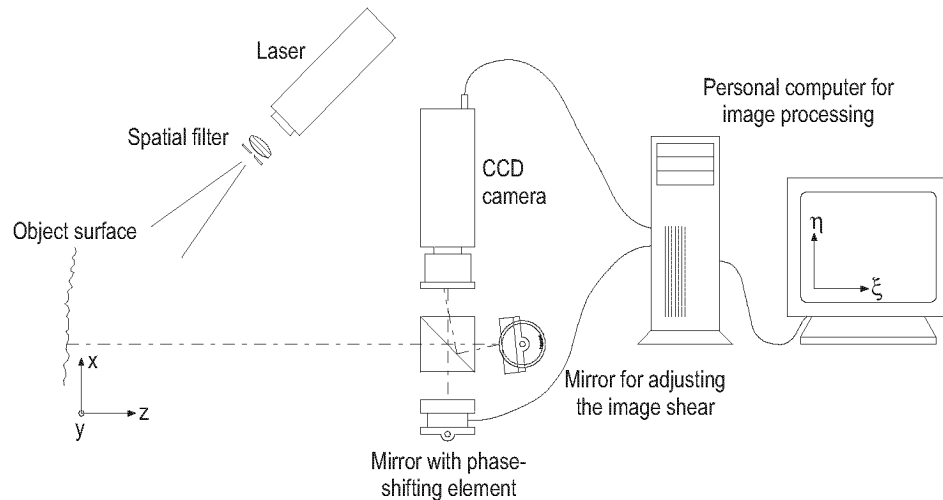
**Michelson interferometer** Still the most popular image-shearing device for shearography is the Michelson interferometer, where the shear is realized by tilting one of the mirrors. Figure 2.10 shows the image shearing effect in the Michelson interferometer (the lens for imaging the object onto the image plane is omitted). The light reflected at the object points  $P$  and  $P_s$  is passing through the beamsplitter BS and is reflected by the mirrors M1 and M2 before reaching the image plane. Since mirror M2 is tilted, each object



point appears twice in the image plane, which is the effect known as *image doubling*. On the other hand, the light from  $P$  and  $P_s$  (separated by the shear distance  $\Delta x$ ) reaches the same image point  $P_i$  and – with coherent light – *interferes* there.

Figure 2.11 shows a sketch of a practical shearography set-up with the Michelson interferometer, i.e. the one we used for the laboratory experiments (see section 8.1 for a detailed description).

**Figure 2.11** Optical set-up for shearography. The camera observes the object through a Michelson interferometer, which creates two laterally sheared images.



Below we will derive the relation between the mechanical deformation of the object and the phase difference measured with shearography. Of course, more or less complete derivations of this relation can be found in literature (e.g. [11, 14, 41]), but this description – first proposed by H. Aebischer [42] – is elegant and shows the simplifications that will later be analysed. We first derive the ‘standard’ equation which is most often used for the interpretation of shearographic results. Afterwards, we identify the simplifications made in the derivation.

**Range of analysis** The phase difference corresponds to the difference of the optical path lengths of the two waves interfering in one image point. In shearography, these are the paths through the two object points that are separated by the shear  $\Delta x$ .

We will calculate the phase difference between the path via a general point  $P$  and the path through its sheared counterpart  $P_s$  for both the *reference state* and the *deformed state*. The subtraction of these phase differences will then lead to the phase difference caused by the deformation of the object.

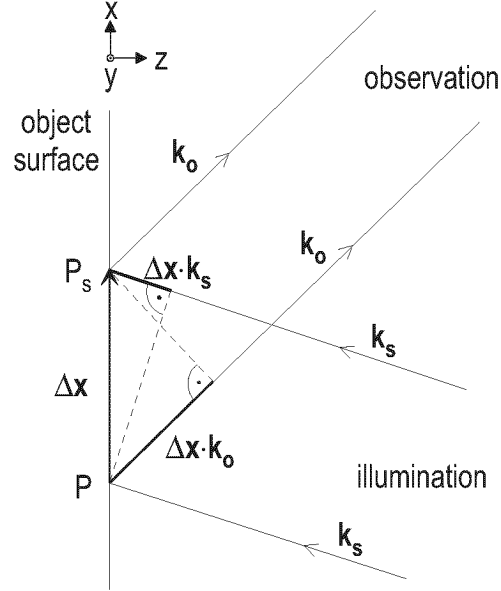
**Reference state** We consider the light paths from the light source to the image plane via the points  $P$  and  $P_s$ , which are imaged onto one point in the image plane by the image shearing device. These light paths do not have the same length.

In a first state of the object, which we call *reference state*, the phase difference resulting from this unequal length is

$$\Delta\phi_r = \Delta\mathbf{x} \cdot \mathbf{k}_s - \Delta\mathbf{x} \cdot \mathbf{k}_o = \Delta\mathbf{x} \cdot (\mathbf{k}_s - \mathbf{k}_o), \quad (2.13)$$

where  $\Delta\mathbf{x}$  is the shear vector (note that the vector is not necessarily oriented in  $x$  direction, it may have components in  $y$  and  $z$  direction).  $\mathbf{k}_s$  and  $\mathbf{k}_o$  are the vectors of illumination and observation, respectively, with vector length  $2\pi/\lambda$ .

**Figure 2.12** Geometry in the reference state. The points  $P$  and  $P_s$  are imaged onto the same image point.



**Deformed state** Due to the deformation of the object, point  $P$  is displaced to  $P'$  (displacement vector  $\mathbf{d}(P)$ ), and  $P_s$  to  $P'_s$  (displacement vector  $\mathbf{d}(P'_s)$ ). The vector between these displaced points is

$$\Delta\mathbf{x}' = \Delta\mathbf{x} + \mathbf{d}(P'_s) - \mathbf{d}(P) \quad (2.14)$$

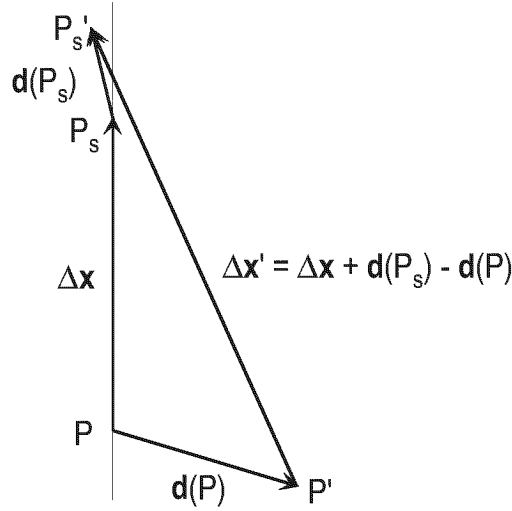
and the phase difference in this second, *deformed* state, is by analogy to eq. (2.13)

$$\begin{aligned} \Delta\phi_d &= \Delta\mathbf{x}' \cdot \mathbf{k}_s - \Delta\mathbf{x}' \cdot \mathbf{k}_o = \Delta\mathbf{x}' \cdot (\mathbf{k}_s - \mathbf{k}_o) \\ &= \{\Delta\mathbf{x} + \mathbf{d}(P'_s) - \mathbf{d}(P)\} \cdot (\mathbf{k}_s - \mathbf{k}_o) \end{aligned} \quad (2.15)$$

**Resulting phase difference** The phase difference resulting from the deformation of the object is calculated by subtracting the phase difference of the reference state (eq. (2.13)) from the phase difference of the deformed state (eq. (2.15))

$$\Delta\phi = \Delta\phi_d - \Delta\phi_r = \{\mathbf{d}(P'_s) - \mathbf{d}(P)\} \cdot (\mathbf{k}_s - \mathbf{k}_o). \quad (2.16)$$

**Figure 2.13** Geometry in the deformed state.



We define the sensitivity vector

$$\mathbf{k} = \mathbf{k}_s - \mathbf{k}_o = \begin{bmatrix} k_x & k_y & k_z \end{bmatrix} \quad (2.17)$$

(in contrast to the wave vectors, the length of the sensitivity vector is usually not  $2\pi/\lambda$ ) and the displacement difference

$$\Delta \mathbf{d} = \mathbf{d}(P_s) - \mathbf{d}(P). \quad (2.18)$$

The term  $\Delta \mathbf{d}$  can be developed into a Taylor series in the shear distance  $\Delta x = |\Delta \mathbf{x}|$  which results in

$$\Delta \mathbf{d} = \frac{\partial \mathbf{d}}{\partial x} \cdot \Delta x + \frac{1}{2} \cdot \frac{\partial^2 \mathbf{d}}{\partial x^2} \cdot \Delta x^2 + \frac{1}{6} \cdot \frac{\partial^3 \mathbf{d}}{\partial x^3} \cdot \Delta x^3 + \dots \quad (2.19)$$

By neglecting the higher-order terms of the Taylor series we obtain

$$\Delta \varphi = \mathbf{k} \cdot \frac{\partial \mathbf{d}}{\partial x} \cdot \Delta x = \left( k_x \cdot \frac{\partial u}{\partial x} + k_y \cdot \frac{\partial v}{\partial x} + k_z \cdot \frac{\partial w}{\partial x} \right) \Delta x, \quad (2.20)$$

where  $\mathbf{d} = \begin{bmatrix} u & v & w \end{bmatrix}$  is the displacement vector in  $P$ . Although not explicitly marked,  $\Delta \varphi$ ,  $\mathbf{k}$ , and  $\mathbf{d}$  are functions of their location  $P(x,y)$  on the object surface.

**Discussion** Equation (2.20) shows that three parts contribute to the phase difference measured with shearography. The deformation of the object appears in form of the derivative in shear direction of the displacement vector  $\mathbf{d}$ . The direction of illumination and observation and the laser wavelength determine the sensitivity vector  $\mathbf{k}$ . The third contribution is the shear distance  $\Delta x$ . In contrast to ESPI, where this possibility is missing, shearography offers the convenience to adjust the measurement sensitivity within a wide range by altering the shear distance. On the other hand, the shear distance has to be accurately determined for a quantitative evaluation of the measurements.

- Assumptions and simplifications
- For the derivation of the ‘standard equation’ (2.20) we made several assumptions and simplifications:
- 1 We assumed that the object surface is macroscopically (in the order of magnitude of the shear distance) plane, strictly speaking that the shear vector lies in the  $x$ - $y$  plane.
  - 2 In eqs. (2.13) and (2.15) we neglected that the sensitivity vector  $\mathbf{k}$  might not be the same in  $P$  and  $P_s$ . This is the case if a spherical wave is used for illumination instead of a plane wave.
  - 3 In contrast to  $\mathbf{k}$  and  $\mathbf{d}$ , which may vary across the object surface, the shear vector  $\Delta\mathbf{x}$  is assumed to be constant.
  - 4 Due to the image shear,  $P$  and  $P_s$  are imaged onto the same image point. We assumed that the displaced points  $P'$  and  $P_s'$  still interfere in the same image point.
  - 5 In eq. (2.20) we only considered the first order term of the Taylor series and neglected the higher order terms. With this approximation, the phase difference depends on the displacement derivative, which is a clearly defined quantity in mechanics. The displacement difference of eq. (2.16), on the other hand, is difficult to imagine for an observer of a shearogram.
  - 6 A *speckle* is the effect of the interference of light reflected from many object points. In the derivation, we only considered the light paths through the points  $P$  and  $P_s$  and neglected the other light paths.
- Analysis
- These assumptions and simplifications were analysed in a project report [43]. The summarized results are:
- 1 If the object surface is not plane, the evaluation is preferably done with the method described in chapter 5. This allows for the accurate determination of the displacement field. However, for the correct matching of the image points with the object points, the 3D object geometry has to be known.
  - 2 The difference between the sensitivity vectors in  $P$  and  $P_s$  is a second order effect, which can not be considered in the evaluation. This will be explained in section 7.3.
  - 3 The practical significance of the error introduced by assuming a constant shear distance across the object is small. The Michelson interferometer as a shear element has been thoroughly analysed by Aebischer and Rechsteiner [44]. Based on their results, the calculation of the exact shear distance could be integrated in an image processing software.
  - 4 The displacements in the image plane caused by the deformation of the object are very small compared with the pixel size. The approximation therefore does not cause a significant error.
  - 5 The error caused by neglecting the higher order terms depends on the relation between the shear distance and the size of the details to be resolved. This simplification can be avoided by using the method described in chapter 5.

- 6 The phase difference can be determined in good approximation by considering only the light path through the centre of the lens. The effect of speckle decorrelation and the resulting phase errors [36] can not be explained with this theory. Still, the filtering process we introduce in chapter 4 effectively reduces the phase errors caused by speckle decorrelation.

Simplifications 3, 5, and 6 will be considered for the quantitative evaluation in chapter 7.

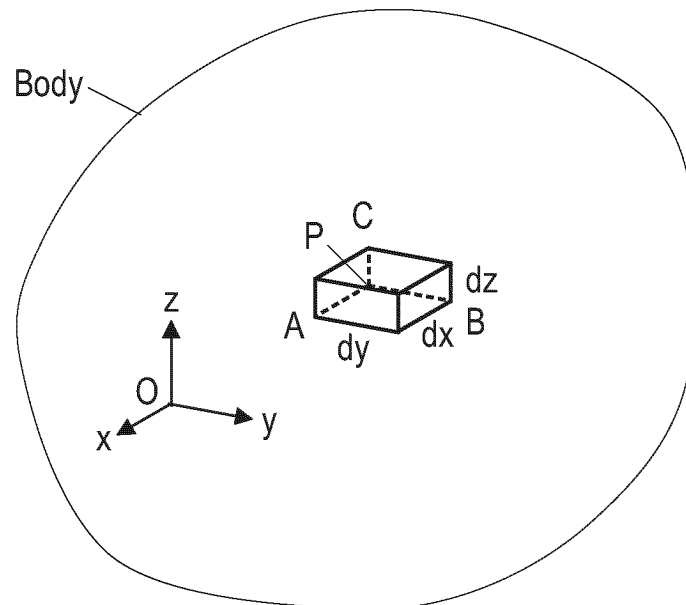
## 2.2 Mechanical Aspects

Throughout this work, terms like *displacement*, *strain*, *displacement derivative* and the corresponding symbols for variables, vectors and tensors are used. This section serves for introducing these terms. Detailed descriptions can be found in good textbooks like Timoshenko's 'Theory of Elasticity' [45].

### 2.2.1 Displacement and Strain

Figure 2.14 shows schematically a solid body with a point  $P$  within this body and a small volume with dimensions  $dx$ ,  $dy$ ,  $dz$ .

**Figure 2.14** A small volume  $dx$ ,  $dy$ ,  $dz$  within a body is chosen to illustrate the deformation of the body.



**Displacement** Upon deformation of the body, the point  $P$  moves relative to the origin  $O$  of the co-ordinate system, it is *displaced*. The displacement vector  $\mathbf{d}$  can be split into the components  $u$ ,  $v$ ,  $w$  parallel to the axes of the co-ordinate system.  $u$  is the component in  $x$  direction,  $v$  in  $y$  direction, and  $w$  in  $z$  direction. In vector representation, the displacement becomes

$$\mathbf{d} = [u \ v \ w]. \quad (2.21)$$

Unit elongation At a point  $A$ , which is located at a distance  $dx$  in  $x$  direction from  $P$ , the displacement amounts to (to the first order in  $dx$ )

$$u + \frac{\partial u}{\partial x} \cdot dx. \quad (2.22)$$

$\partial u / \partial x$  – the derivative of the displacement  $u$  in  $x$  direction – is called *unit elongation*. In this work sometimes also the term ‘strain’ is used for this quantity. Accordingly, with the points  $B$  and  $C$ , the unit elongations in  $y$  and  $z$  direction are derived.

The symbol  $\epsilon$  stands for the unit elongation, such that

$$\epsilon_x = \frac{\partial u}{\partial x}, \epsilon_y = \frac{\partial v}{\partial y}, \epsilon_z = \frac{\partial w}{\partial z}. \quad (2.23)$$

Shearing strain In addition to the unit elongations, also distortions of the angles may occur. The angle between  $PA$  and  $PB$ , for example, may be diminished by the angle  $\partial v / \partial x + \partial u / \partial y$ . This *shearing strain* is represented by the symbol  $\gamma$ , where

$$\gamma_{xy} = \frac{\partial u}{\partial y} + \frac{\partial v}{\partial x}, \gamma_{xz} = \frac{\partial u}{\partial z} + \frac{\partial w}{\partial x}, \gamma_{yz} = \frac{\partial v}{\partial z} + \frac{\partial w}{\partial y}. \quad (2.24)$$

The six quantities  $\epsilon_x, \epsilon_y, \epsilon_z, \gamma_{xy}, \gamma_{xz}, \gamma_{yz}$  are called the *components of strain* and can be represented in tensor form:

$$\begin{bmatrix} \epsilon_x & \gamma_{xy}/2 & \gamma_{xz}/2 \\ \gamma_{xy}/2 & \epsilon_y & \gamma_{yz}/2 \\ \gamma_{xz}/2 & \gamma_{yz}/2 & \epsilon_z \end{bmatrix} \quad (2.25)$$

## 2.2.2 Stress

Components of stress Stress is the amount of force per unit area of the surface on which it acts [45]. For the small volume  $dx, dy, dz$ , we introduce the stress components acting on the sides of the volume in directions of the co-ordinate system. The components of stress normal to these surfaces are called *normal stresses* and are represented by the symbol  $\sigma$ . The stresses in the plane of the surface are the *shearing stresses*  $\tau$ . Considering the equilibrium of the element, six components suffice to describe the stress state:  $\sigma_x, \sigma_y, \sigma_z, \tau_{xy}, \tau_{xz}, \tau_{yz}$ . The stress tensor in cartesian co-ordinates is

$$\begin{bmatrix} \sigma_x & \tau_{xy} & \tau_{xz} \\ \tau_{xy} & \sigma_y & \tau_{yz} \\ \tau_{xz} & \tau_{yz} & \sigma_z \end{bmatrix}. \quad (2.26)$$

Hooke's law If the relation between stress and strain is linear elastic, which is a good approximation for many engineering materials if they are subjected to small deformations, *Hooke's law* can be applied. In the case of isotropic

materials, it says that the components of strain and stress are related by the material constants  $E$ ,  $\nu$ , and  $G$ :

$$\epsilon_x = \frac{\sigma_x}{E}, \quad \epsilon_y = -\nu \frac{\sigma_x}{E}, \quad G = \frac{E}{2(1+\nu)}. \quad (2.27)$$

$E$  is the *modulus of elasticity in tension* (also known as *Young's modulus*). The constant  $\nu$  is called *Poisson's ratio* and describes the lateral contraction of a body under tension. The *modulus of elasticity in shear* or *modulus of rigidity* is the constant  $G$ .

### 2.2.3 What can we Measure?

---

**ESPI** As explained in section 2.1.2, ESPI serves for the measurement of displacements. With adequate equipment, all three components  $u$ ,  $v$ , and  $w$  can be determined. Of course, this is only possible for the points on the object surface.

**Shearography** In section 2.1.3, the relation between the measured phase and the deformation was derived. With shear in  $x$  direction, approximations to the displacement derivatives  $\partial u/\partial x$ ,  $\partial v/\partial x$ , and  $\partial w/\partial x$  contribute to the measured result. Accordingly, with shear in  $y$  direction,  $\partial u/\partial y$ ,  $\partial v/\partial y$ , and  $\partial w/\partial y$  are contained in the result. How single components can be isolated from the measurements is shown in Chapter 6, "Isolation of the Components". The derivatives in  $z$  direction can not be determined with a method measuring on the surface.

From the components of strain, it is therefore possible to measure  $\epsilon_x$ ,  $\epsilon_y$ , and  $\gamma_{xy}$ , i.e. the unit elongations and the shearing strain on the surface.

Additionally,  $\partial w/\partial x$  and  $\partial w/\partial y$  can be determined. These can be used to calculate the bending moments in plates of uniform thickness, where  $\partial^2 w/\partial x^2$  and  $\partial^2 w/\partial y^2$  are the important quantities [45, 11].





## PHASE DETERMINATION

The quantity measured with a video camera is the light *intensity*. As shown in the previous chapter, the mechanical information we are interested in is coded in the *phase difference*. It is therefore the purpose of this chapter to introduce the principal techniques used in speckle interferometry and shearography to determine the phase from the intensity images.

### 3.1 Temporal Phase Shifting

The equation for the intensity measured by a pixel (eq. (2.1)) can be written in the form

$$\begin{aligned} I &= I_0 + I_m \cdot \cos \Delta\phi_r \\ I' &= I_0' + I_m' \cdot \cos \Delta\phi_d \end{aligned} \quad (3.1)$$

for the reference state and the deformed state respectively, where  $I_0$  is called *background intensity* and  $I_m$  is the *modulation* [36]. By assuming that  $I_0 = I_0'$  and  $I_m = I_m'$ , the number of unknowns is reduced to four, i.e.  $I_0$ ,  $I_m$ ,  $\Delta\phi_r$ , and  $\Delta\phi_d$ . It is common practice in speckle interferometry and shearography to treat the reference and deformed state individually, with three unknowns in each state.

Multiple  
intensity  
measure-  
ments

The idea of temporal phase shifting is to determine the unknowns by performing multiple intensity measurements with introduction of an additional phase difference, the so-called *phase shift*. This is effected by changing the length of one light path relative to the other by fractions of the laser wavelength. The intensity measurements are recorded sequentially in time, which explains the name “temporal phase shifting”. The most common scheme for the image processing based on the temporal phase shifting method is depicted in figure 3.1. In the reference state, four images with a phase shift of  $\pi/2$  between them are recorded:

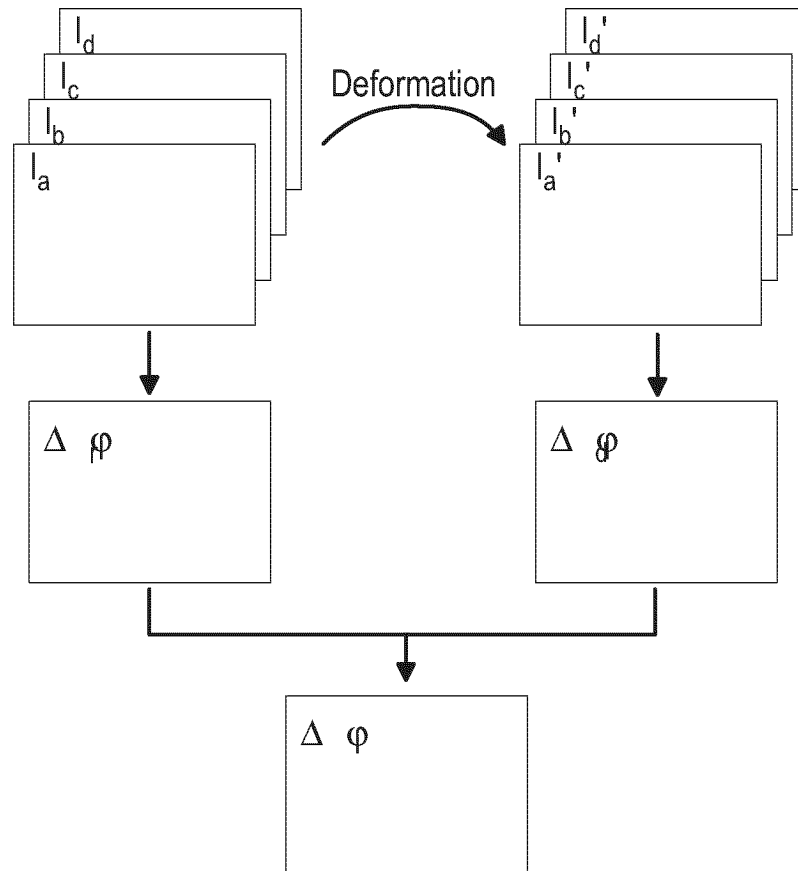
$$\begin{aligned}
I_a &= I_0 + I_m \cdot \cos \Delta\phi_r \\
I_b &= I_0 + I_m \cdot \cos(\Delta\phi_r + \pi/2) \\
I_c &= I_0 + I_m \cdot \cos(\Delta\phi_r + \pi) \\
I_d &= I_0 + I_m \cdot \cos(\Delta\phi_r + (3\pi)/2)
\end{aligned}
\tag{3.2}$$

As can be shown easily by using trigonometric relations, the tangent of the phase difference is

$$\tan \Delta\phi_r = \frac{I_d - I_b}{I_a - I_c}
\tag{3.3}$$

The phase difference  $\Delta\phi_r$  is now determined with the four quadrant inverse tangent which yields a phase value in the range  $[-\pi, +\pi]$ .

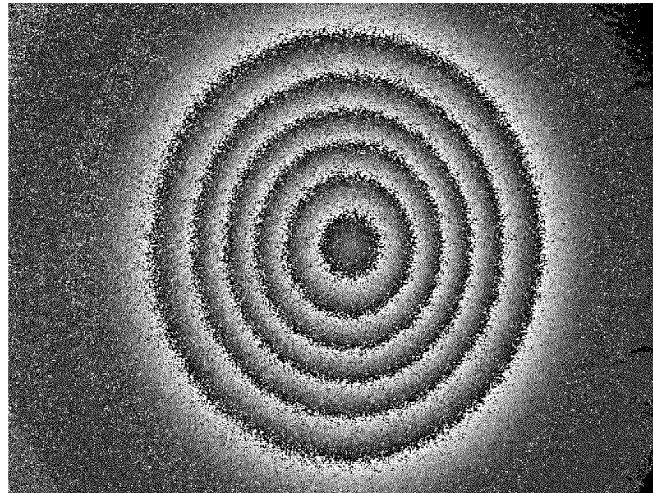
**Figure 3.1** Image processing using the temporal phase shifting method with 4+4 images.



In the same way, the phase difference in the deformed state  $\Delta\phi_d$  can be calculated from the four images  $I'_a$ ,  $I'_b$ ,  $I'_c$ , and  $I'_d$ . The subtraction modulo  $2\pi$  of the two phases  $\Delta\phi_r$  and  $\Delta\phi_d$  then yields the wanted phase difference  $\Delta\phi$ , the *phase fringe pattern*. Additionally, the modulations  $I_m$  and  $I'_m$  could be determined from eqs. (3.2) and used for the further processing of the fringe pattern, e.g. by giving more weight to well modulated pixels for filtering and phase unwrapping.

Figure 3.2 shows the result of the same experiment as the one shown in figure 2.7. But here, the phase was evaluated according to the scheme described above. Although the image is noisy, the quality of this result seems to be much better than the one of figure 2.7. As the phase modulo  $2\pi$  is measured here, a characteristic distribution of the grey levels appears: From the border of the image to the centre, the grey levels change from black via grey gradually to white and then abruptly to black again.

**Figure 3.2** Phase fringe pattern of the out-of-plane displacement field of a clamped circular plate.



- Other algorithms** Various temporal phase shifting algorithms which use from 3+1 (three images recorded in the reference state plus one in the deformed state) to 5+5 and more images with known or unknown phase shifts were published in the past years. Reviews of their properties and comparisons can be found in literature [46, 48, 49].
- Realization** In order to realize the phase shift between the two interfering waves, the path length in one arm of the interferometer has to be altered by fractions of the laser wavelength [46]. With the shearography set-up shown in figure 2.11, temporal phase shifting can easily be implemented by mounting one mirror in the Michelson interferometer on a piezo-electric element. Applying a voltage to the piezo-electric element effects a translation of the mirror, which causes a change in the path length. For automated acquisition of the phase-shifted images, the voltage can be controlled by a personal computer. This was realized in both the laboratory set-up (section 8.1) and the prototype system (section 8.3).
- Limitations** A drawback of the temporal phase shifting method is that several images have to be recorded in at least one of the object states. It has therefore to be secured that the object and the set-up are at rest for the recording of the images. With pulsed lasers, temporal phase shifting can not be used, when only two laser pulses are available. In these cases, temporal phase shifting is not the method of choice.

## 3.2 Spatial Phase Shifting

Phase from one image Spatial phase shifting offers the possibility to evaluate the phase from a single image. Two plane wave fronts reaching the CCD chip with a small angle between them (see figure 3.3) effect a linear phase change from pixel to pixel. According to eq. (2.1), the intensity will follow the cosine function. This regular intensity variation is called *carrier fringes*. Carrier fringes are appropriate for the phase evaluation with spatial phase shifting if their spatial frequency is considerably higher than the spatial frequency of the desired phase information [50]. To obtain two tilted wave fronts in shearography, a Mach-Zehnder interferometer can be used [25].

**Figure 3.3** Interference of two wave fronts with a small angle between them effects carrier fringes on the CCD chip.

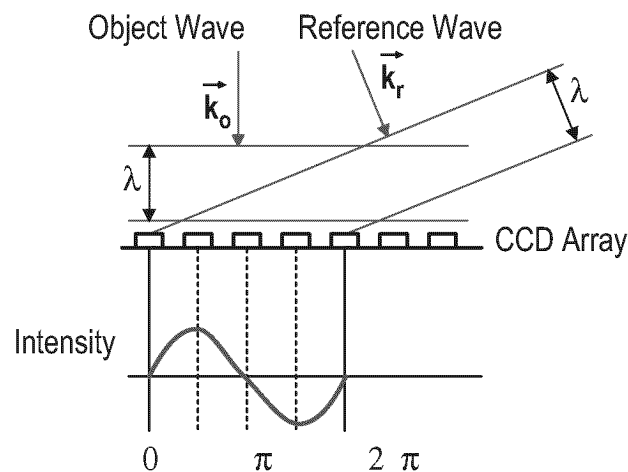
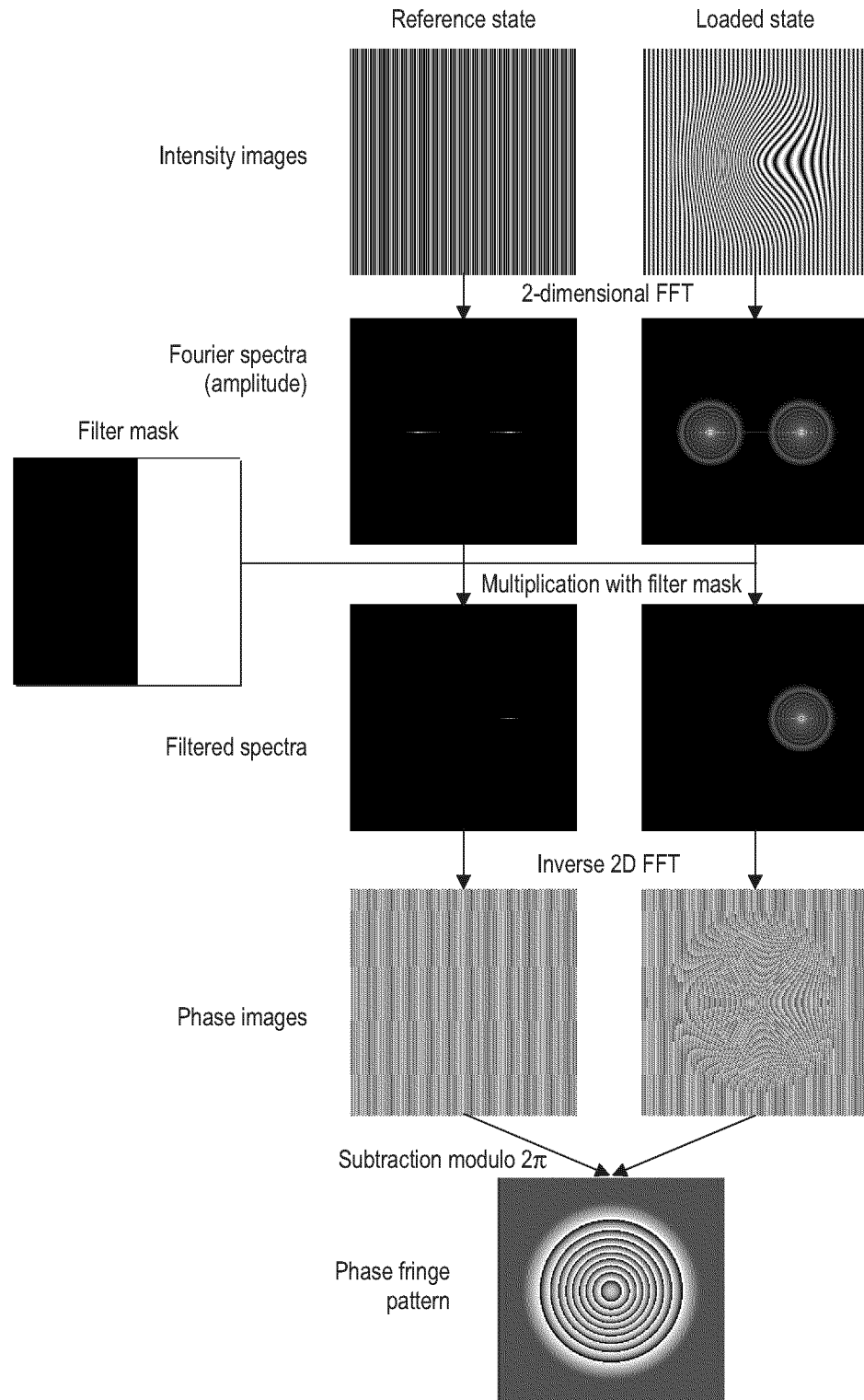


Image processing In figure 3.4 the processing of the images is illustrated on the example of the deformation of a clamped circular plate (see also section 5.4). This example was simulated with a plate diameter of 160 mm, the wavelength  $\lambda$  was 632.8 nm, the deformation at the plate center was 3  $\mu\text{m}$ , and the carrier fringes are chosen such that  $2\pi$  corresponds to 5 pixels. The intensity image of the reference state shows just the carrier fringes, the loaded state shows a deformation of the object superposed on the carrier fringes. Both intensity images are Fourier-transformed. In the resulting Fourier spectra, a filter mask is then applied to single out one of the two side bands. The inverse Fourier transforms of the two filtered spectra are complex, and their phases directly represent the desired phase information (i.e. the phase difference between the image of the object and the reference wave in speckle interferometry or between the sheared images in shearography), apart from an additive term [50, 51]. The difference of these two phases yields the phase fringe pattern related to the deformation of the object, whereby the additive term cancels out [50, 52].

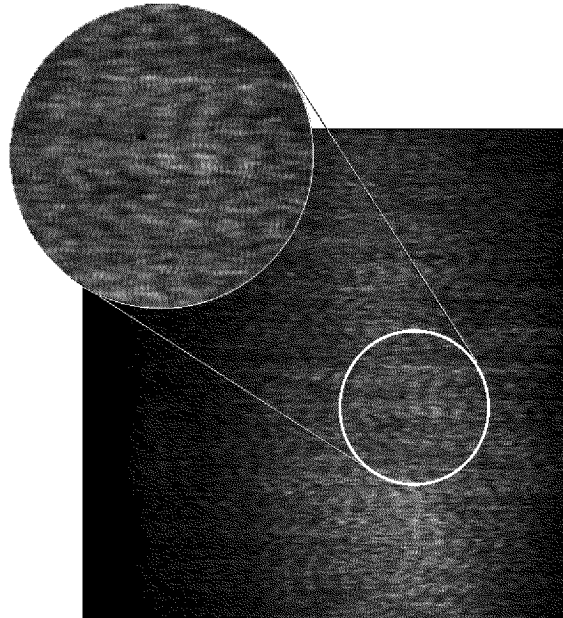
Carrier fringes with speckles In speckle interferometry and shearography, the intensity fluctuates from speckle to speckle. In order to generate a carrier fringe pattern that can be evaluated with spatial phase shifting, the speckles have to cover several pixels. As shown in eq. (2.7), these large speckles can be produced by reducing the aperture size in the imaging system. Figure 3.5 shows an

intensity image recorded with a shearography set-up adjusted for spatial phase shifting [51]. The aperture was a vertical slit, which enlarges the speckles in horizontal direction. As can be seen in the magnified area, the speckles are modulated by fine vertical carrier fringes.

**Figure 3.4** Image processing for spatial phase shifting.



**Figure 3.5** Intensity image recorded with a shearography set-up for spatial phase shifting. The magnified area shows that the speckles are enlarged in horizontal direction and modulated by fine vertical carrier fringes [51].



**Limitations** The fact that only two images have to be recorded has to be paid with a high level of noise – especially in shearography, where two speckle patterns interfere in the image plane – and a loss of resolution. This could be avoided by using a high-resolution camera or with an arrangement where the phase shifted images are recorded simultaneously with three or four cameras.

**Other methods** An alternative method is to introduce the carrier between the recording of the two images by changing the geometric conditions (e.g. by tilting one wave front) [19, 33]. This method does not need large speckles, but a system to change the illumination geometry between the two recordings. Various types of spatial methods and their theoretical description were compiled by Kujawinska [53].

**Shearography** Aside from the application of the carrier fringe method [25] mentioned above, a shearography system with two CCD cameras recording four phase-shifted images simultaneously was presented recently [54].

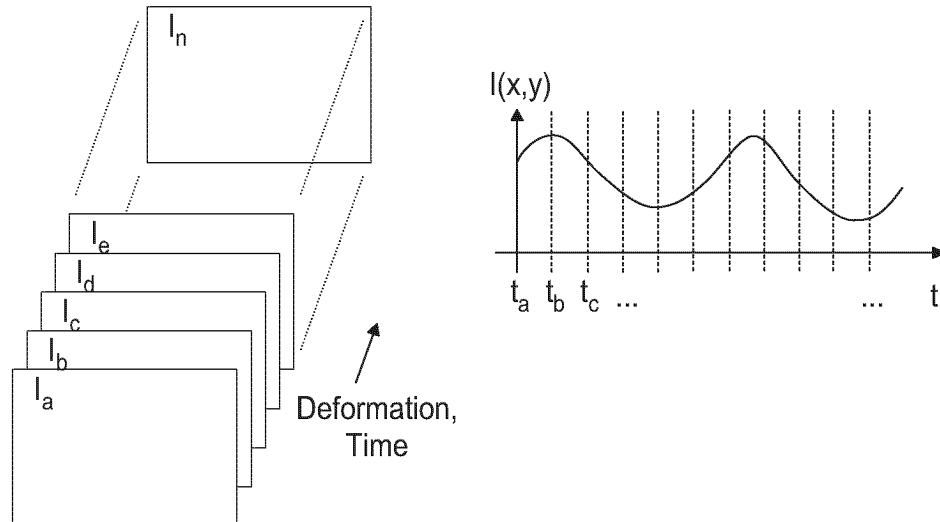
### 3.3 Dynamic Phase Shifting

The third phase evaluation method has a big potential in applications where the deformation of the object is continuous and limited in speed. The method was developed in the thesis of X. Colonna de Lega [55] and other publications [56-61].

**Many intensity images** The method requires the recording of many intensity images during the deformation of the object. Then the phase can be evaluated from the intensity variation in each pixel (see figure 3.6). A linear phase change would cause a sinusoidal intensity change with a specific frequency; a non-linear phase change accordingly changes the intensity curve. This

evaluation can be done by Fourier [59, 60, 61] or wavelet analysis [55, 57]. In order to determine the sign of the deformation and to obtain results at areas that are not deformed, an additional temporal phase shift has to be introduced from image to image.

**Figure 3.6** Scheme for the recording and evaluation of images for the dynamic phase shifting method.



Advantages/  
limitations

The advantages of this method are that the result is the absolute phase change, which is not wrapped modulo  $2\pi$ . No phase unwrapping (see section 4.6) and determination of the fringe order is necessary. Additionally, the object loading does not have to be stopped for the measurement as for temporal phase shifting. This is important in materials testing, where relaxation effects may occur. From the recorded images it is also possible to investigate the temporal evolution of the deformation. One of the main difficulties consists in tuning the speed of the object deformation to the acquisition rate of the images. This is necessary to obtain a sufficient sampling rate without a too big expenditure of memory and processing time. Depending on the targeted deformation speed, special hardware like a high-speed camera and image acquisition electronics is necessary.

### 3.4 Selected Phase Shifting Method

From the above methods of phase determination, our laboratory is experienced in the temporal and the spatial phase shifting method. It would have been a extensive effort to introduce the dynamic phase shifting, as no commercial system is available up to now.

Temporal  
phase shifting

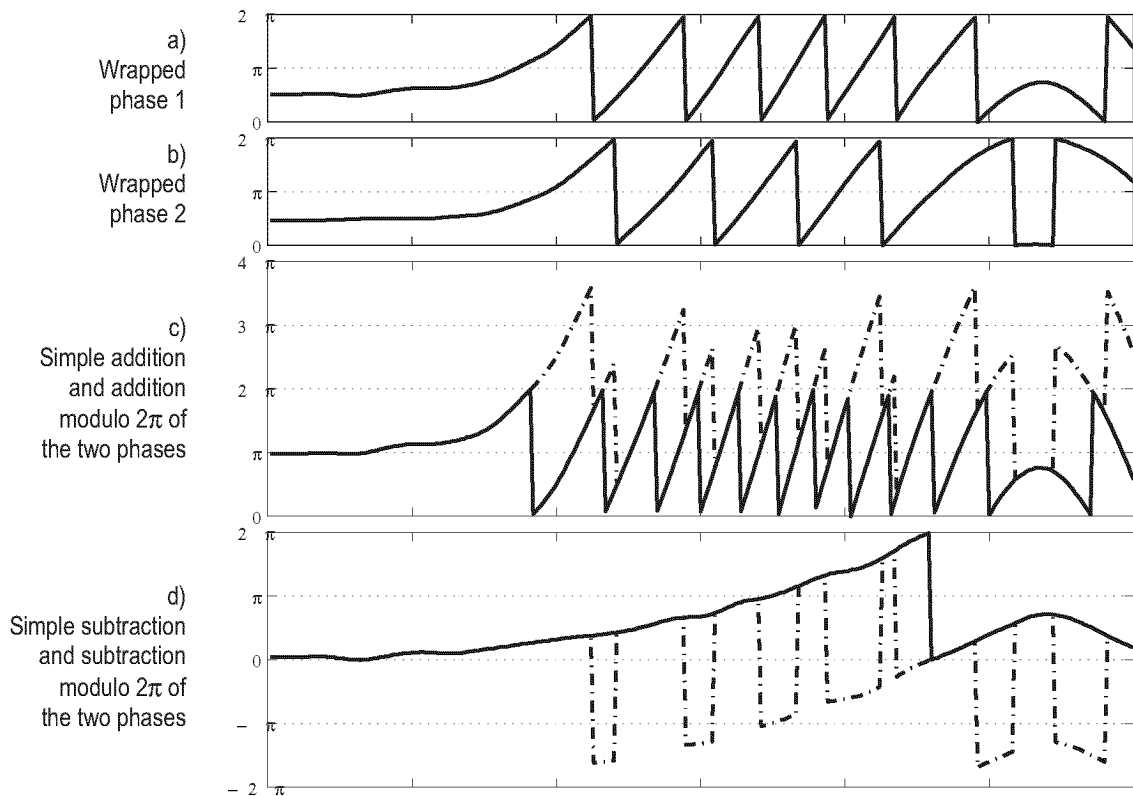
Since we restricted ourselves for this work to quasi-static deformations, both spatial and temporal phase shifting can be applied. Because of the good quality of the results and the reliability of the technique, we chose the *temporal phase shifting method* for the work documented in the following chapters.

### 3.5 Operations with Phase Fringe Patterns

For both the temporal and the spatial phase shifting method, the result is the phase wrapped modulo  $2\pi$ , the so-called *phase fringe pattern*.

In the following chapters, the operations of addition and subtraction modulo  $2\pi$  will often be used. So we shortly explain these operations here using the illustration in figure 3.7. The curves a) and b) show two cuts through a phase fringe pattern with the typical  $2\pi$  phase discontinuities.

**Figure 3.7** Demonstration of the phase correct addition and subtraction. a) and b) Two wrapped phases; c) Simple addition of the phases of a) and b) (dash-dotted line) and the addition modulo  $2\pi$  (solid line); d) Simple subtraction of a) and b) (dash-dotted line) and the subtraction modulo  $2\pi$  (solid line).



**Addition modulo  $2\pi$**  In figure 3.7 c), the simple addition of the two curves is drawn with a dash-dotted line, covering a range from  $0$  to  $4\pi$ . The addition modulo  $2\pi$  is drawn with a solid line. This is the addition, where we subtract  $2\pi$  from all results larger than  $2\pi$ . For two similar fringe patterns, this addition leads to a higher fringe density [6].

**Subtraction modulo  $2\pi$**  Analogously, the simple subtraction would lead to results in the range from  $-2\pi$  to  $+2\pi$ , as drawn with a dash-dotted line in figure 3.7 d). The subtraction modulo  $2\pi$  adds  $2\pi$  to all values smaller than zero and is plotted with a solid line.

If more than two fringe patterns are involved, the operation has to be accordingly adapted, such that the result is in the range from  $0$  to  $2\pi$ .



# FILTERING OF PHASE FRINGE PATTERNS AND PHASE UNWRAPPING

For the quantitative evaluation of ESPI and shearography measurements, the phase fringe pattern has to be further processed. This chapter presents a new filtering technique, which effectively removes the noise, without affecting the details of the fringe pattern. The method is demonstrated on a shearography example and compared with other filtering techniques. The last section of this chapter then explains the process of phase unwrapping.<sup>1</sup>

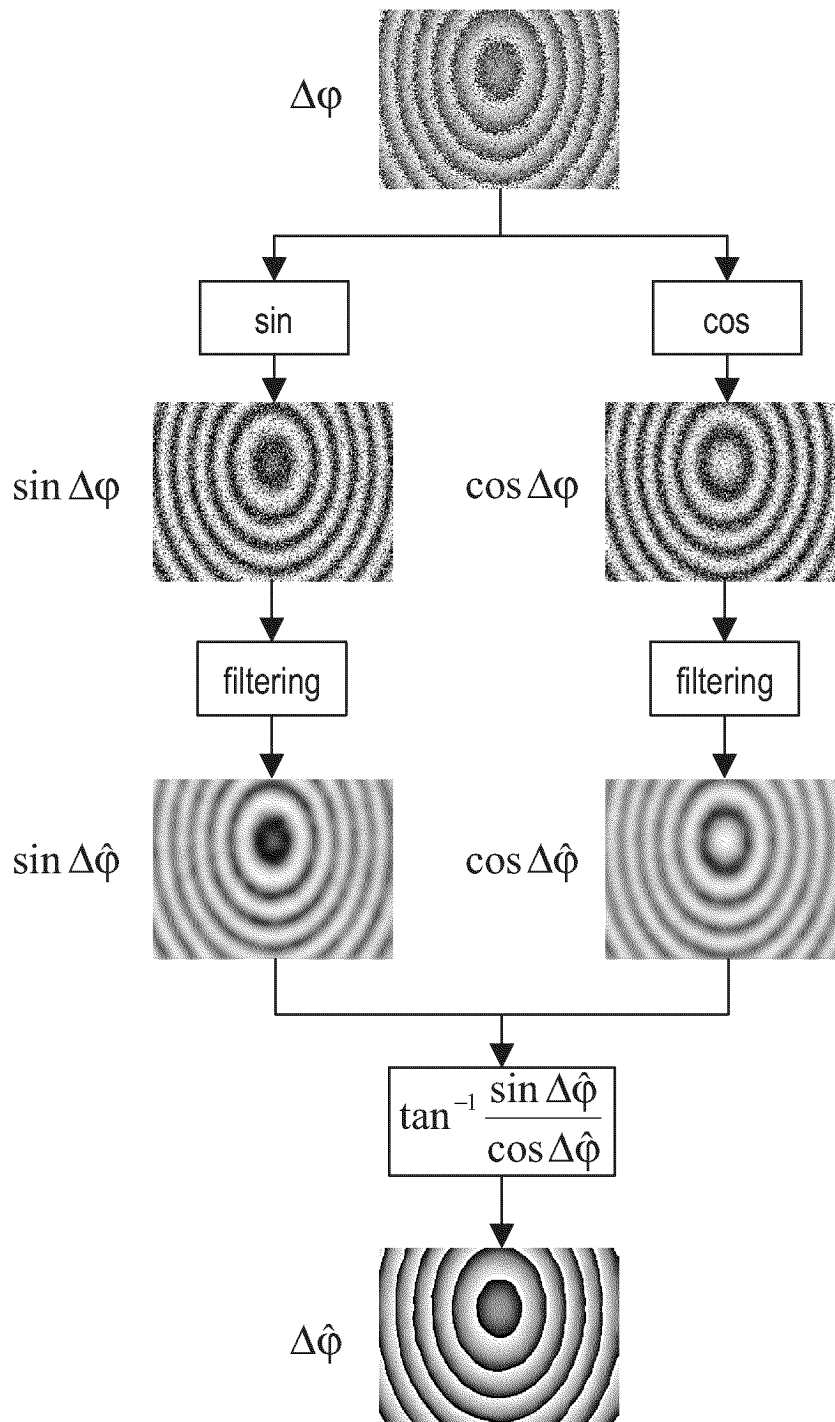
## 4.1 Introduction

---

Noisy phase fringe pattern	The result of speckle interferometry and shearography measurements using temporal or spatial phase shifting is represented in the form of a phase map. This phase map is wrapped modulo $2\pi$ and is called <i>phase fringe pattern</i> . Mainly due to speckle decorrelation effects [36], the resulting phase fringe patterns are strongly affected by noise. This noise must somehow be dealt with in order to be able to evaluate the measured phase fringe patterns.
Conventional filtering	The common way of evaluating phase fringe patterns is to apply a sine/cosine average filter (see section 4.2) with a kernel size ranging from $2 \times 2$ to $7 \times 7$ one to three times, and then to unwrap the filtered phase fringe pattern. This procedure suggests itself by the algorithms for filtering and unwrapping phase fringe patterns which are available in commercial software packages like OPTOCAT, PISA, ISTR <sup>2</sup> etc. Since the results from this procedure are much less than satisfactory in most of the cases, a lot of effort has been put into improving the filtering and unwrapping algorithms in the last two decades.

1. Most of the material about filtering is taken from the publication “A simple and effective method for filtering speckle-interferometric phase fringe patterns” by H. A. Aebischer and S. Waldner [62] (Copyright © 1999 Elsevier Science B.V.).
2. OPTOCAT: Breuckmann GmbH, Meersburg, Germany; PISA: GOM mbH, Gesellschaft für optische Meßtechnik, Braunschweig, Germany; ISTR: Dr. Ettemeyer GmbH & Co., Neu-Ulm, Germany.

**Figure 4.1** Scheme for the sine/cosine filtering of phase fringe patterns. This scheme is not only applied for the conventional filter method, but also for all other methods described in this chapter.



Advanced filtering or advanced unwrapping?

In our opinion, and according to our own experience in the field, the problem of evaluating phase fringe patterns can be attacked from two extreme points of view: In the first one, all the effort is put into improving the filter algorithm. If a sufficiently high degree of quality can be achieved, then the unwrapping of the resulting (nearly) perfectly filtered phase fringe pattern is trivial – there is no need for a fancy unwrapping algorithm. In the second point of view, all the effort is put into improving

the unwrapping algorithm. If this algorithm can directly unwrap unfiltered phase fringe patterns, then the resulting phase maps contain only a small remaining amount of additive noise, which can easily be eliminated with a primitive average filter. There is then no need for a special algorithm for filtering phase fringe patterns.

We don't want to discuss the relative merits of these two points of view. We simply adopt the first point of view here, and we present a filter method which, it seems, comes close to the above-mentioned ideal. We show that, despite of its simplicity, our method clearly outperforms the best currently available filter algorithms, like the scale-space filter [63] and Pfister's partially recursive filter [64]. The basic idea of our method is to apply a weak sine/cosine average filter 20 to 30 times rather than only two or three times as is common practice. Depending on the pattern to be filtered we allow for an anisotropic average filter for best results. It is vital that in-between the single repetitions of the filter steps, the phase is always recomputed before the next filter step is initiated. If this rule is observed, then the continuous repetition of the process automatically leads to an adapted filter effect: sparse fringes are filtered with increasing strength from step to step, whereas dense fringes are not filtered any further after the first few steps and are thus not smeared out.

## 4.2 Conventional Filter Method

---

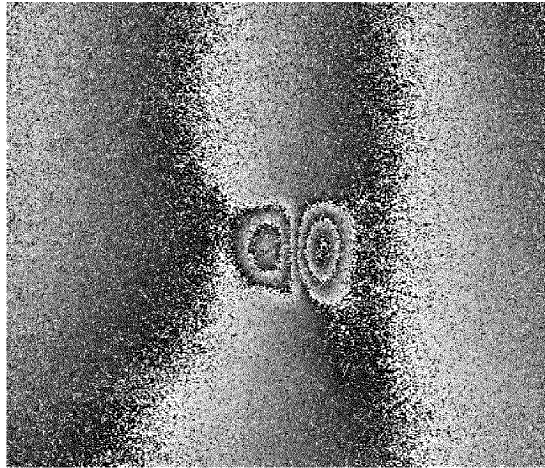
Sine/cosine  
average  
filtering

Since both the speckle noise and the  $2\pi$  discontinuities in phase fringe patterns are characterized by high spatial frequencies, applying a low-pass filter not only reduces the noise, but also smears out the discontinuities. This problem is solved by calculating the sine and cosine of the wrapped phase fringe pattern  $\Delta\varphi$ , which leads to the continuous fringe patterns  $\sin\Delta\varphi$  and  $\cos\Delta\varphi$  (see figure 4.1). These sine and cosine fringe patterns are filtered individually by applying an average filter. This filter averages the values in an  $n \times n$  neighbourhood of each pixel in the image, where  $n$  is an odd whole number. From the filtered sine and cosine fringe patterns  $\sin\Delta\hat{\varphi}$  and  $\cos\Delta\hat{\varphi}$  the phase fringe pattern  $\Delta\hat{\varphi}$  is calculated by the four-quadrant inverse tangent of the sine and cosine patterns. This process is usually repeated two or three times.

Shearography  
example

We chose a shearography measurement as an example to compare the conventional with the new filter method. The test object was a plate made from layers of glass fibre reinforced plastic (GFRP). Between two layers, a Teflon patch was inserted in order to simulate a delamination. The sample was heated shortly before the measurement was taken in order to produce a deformation of the surface. In the delaminated area, the deformation was significantly larger than in the rest of the plate, so that the simulated flaw could easily be detected. The resulting phase fringe pattern shown in figure 4.2 consists of areas where the fringes are sparse (where no delamination occurred), as well as of areas where they are dense (where delamination occurred).

**Figure 4.2** Original result of a shearography measurement. The phase fringe pattern is strongly affected by noise.

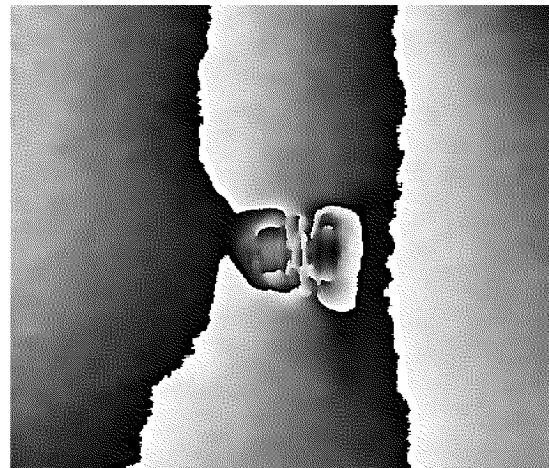
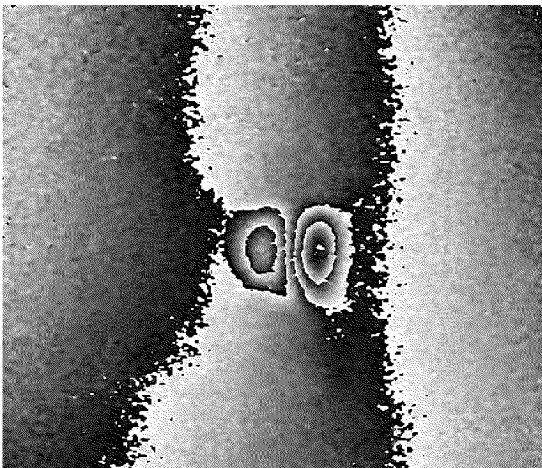


Results of  
conventional  
filtering

Figure 4.3 a) is the result of conventional filtering applying a  $3 \times 3$  average filter twice. In the delaminated area the filtering effect is quite good, whereas the remaining part of the image is still considerably noisy.

In principle, this noise can be further reduced by using a stronger filter. As an example, figure 4.3 b) shows the result of applying a  $15 \times 15$  average filter once. Obviously, the noise is more effectively suppressed, but in the delaminated area the dense fringes are smeared out, i.e. part of the information content of the image has unintentionally been destroyed. The conclusion is that fringe patterns of varying fringe density (which represents the usual case) cannot satisfactorily be filtered with the conventional technique.

**Figure 4.3** a) The twofold application of a  $3 \times 3$  average filter on figure 4.2 leads to a phase fringe pattern which is still very noisy. b) A  $15 \times 15$  average filter applied to figure 4.2 filters the wide fringes effectively, whereas the dense fringes are smeared out.

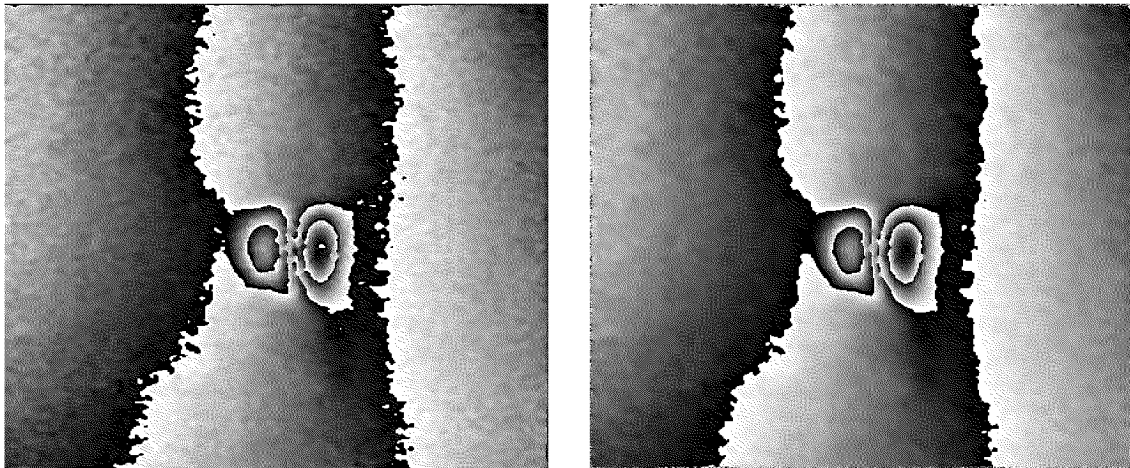


The filtering of the measured fringe pattern was performed on a UNIX workstation (IBM RS6000) using programs written in C. The time needed for the filtering was 7.7 sec. to produce figure 4.3 a) and 5.0 sec. for figure 4.3 b).

## 4.3 Advanced Filter Methods

**Scale-space filter** Kaufmann et al. [63] analysed and compared Lee, Frost, geometric, scale-space, wavelet, and Fourier filters. Most of these filtering methods originate from synthetic aperture radar (SAR) imagery. For speckle interferometry, the authors found the scale-space filter to be the most promising. The input parameters for this adaptive filter are the number of repetitions and the scale factor  $\alpha$ . The smaller  $\alpha$ , the larger the neighbourhood that contributes to the filtering of a pixel. We applied the scale-space filter to the sine and cosine fringe pattern individually and obtained the best result using  $\alpha = 1/4$  after five iterations<sup>3</sup>. The result shown in figure 4.4 a) is significantly better than the results of conventional filtering, as expected. It took 80.4 sec. to filter this image on the IBM RS6000.

**Figure 4.4** a) Five iterations of scale-space filtering [63] with  $\alpha = 1/4$  leads to a result which is better than those shown in figure 4.3. b) Pfister's semi-recursive filter [64] with a  $5 \times 5$  kernel yields an even better result than the scale-space filter.



**Partially recursive filter** Another advanced filter is the partially recursive filter developed by B. Pfister [64]. Here, unfiltered and filtered data are stored in the same image matrix. The filter kernel moving from pixel to pixel gives more weight to the neighbouring pixels that have already been filtered than to the unfiltered ones. We used a filter kernel of the form

$$h = \begin{bmatrix} 1 & 2 & 3 & 2 & 1 \\ 2 & 3 & 4 & 3 & 2 \\ 3 & 4 & 1 & 1 & 1 \\ 1 & 1 & 1 & 1 & 1 \\ 1 & 1 & 1 & 1 & 1 \end{bmatrix} \quad (4.1)$$

and applied it twice to obtain the image shown in figure 4.4 b). The result is even better than the one obtained with scale-space filtering. An

3. We would like to thank Dr. Abundio Davila (Centro de Investigaciones en Optica, Leon, Mexico) for placing at our disposal the program code of the scale-space filter.

advantage of this filter is its fast processing: the filtering was performed within 7.7 seconds.

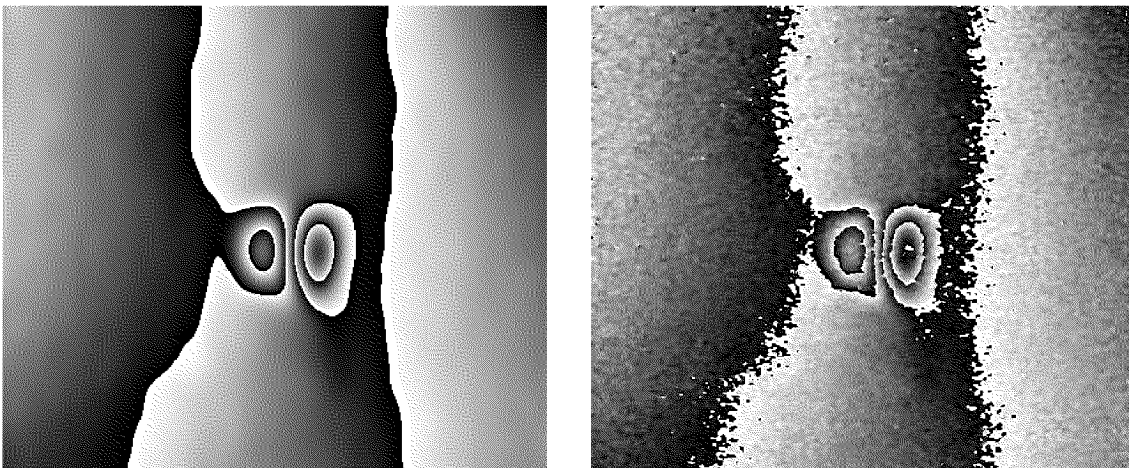
## 4.4 Our Filter Method

Our method differs from the conventional one as outlined in section 4.2 in only two simple points: (1) the inclusion of anisotropic filtering, and (2) the increased number of repetitions of the process.

### Anisotropic filtering

The anisotropic filtering is realized by allowing the filter strength to be unequal in the vertical and horizontal direction. We average over an  $n \times m$  neighbourhood, where  $n$  (the vertical filter strength) and  $m$  (the horizontal filter strength) are odd whole numbers.

**Figure 4.5** a) Our filter method – a  $7 \times 3$  average filter applied 30 times with intermediate phase recalculation – applied to figure 4.2 yields an excellently filtered image: The noise is effectively suppressed and all fringes are perfectly preserved. b) For comparison, the result of conventional filtering (a  $3 \times 3$  average filter applied twice) is shown again.



### Multiple repetition

If the process of sine and cosine calculation, filtering, and inverse tangent calculation is repeated 20 to 30 times, we observe the following effect: Dense fringes, which are perfectly filtered after a few repetitions, are not affected by the later iterations, but sparse fringes continue to be filtered more strongly from iteration to iteration. In other words, the process produces the effect of an automatic adaptive filter.

### Phase recalculation

It is essential to recalculate the phase after each filter step and to calculate the sine and cosine fringe patterns from this new phase before the next filter step is initiated. Multiple filtering with a small strength without intermediate recalculation of the phase would have the same effect as the single application of a strong filter, leading to a result as shown in figure 4.3 b) with the dense fringes smeared out.

### Excellent result

Since the highest fringe density in our exemplary phase fringe pattern (figure 4.2) occurs in the horizontal direction, we chose the horizontal filter size to be smaller than the vertical filter size. In order to obtain the phase fringe pattern of figure 4.5 a), we filtered the original image 30 times with a strength of  $7 \times 3$ . The result is an excellently filtered image.

All fringes are perfectly preserved, and the noise is very effectively suppressed. Obviously, the result shown in figure 4.5 a) represents a clear improvement over the ones shown in figure 4.3 (conventional filter) and figure 4.4 (scale-space filter and partially recursive filter).

Longer  
processing  
time

This excellent quality has to be paid with a longer processing time. The filtering took 117.6 seconds. We observed that about 70% of the calculation time was needed for the phase recalculation and calculation of the sine/cosine fringe patterns. Using look-up tables instead of the trigonometric functions has the potential of reducing the processing time considerably.

While the qualitative superiority of this filter is obvious, a quantitative assessment of the filter has not been performed so far. A detailed explanation why the filter works so well is also missing and is not performed within this work.

## 4.5 Conclusions

---

We have described a simple and very efficient method for filtering speckle-interferometric phase fringe patterns, such as arise in speckle interferometry as well as in holographic interferometry. Our method consists of the multiply repeated application of an anisotropic sine/cosine average filter. On an exemplary shearographic measurement result, the superiority of this filter over the best currently known algorithms, i.e. the scale-space filter and the partially recursive filter, has been shown.

## 4.6 Phase Unwrapping

---

The goal of phase unwrapping is to reconstruct the phase information from the phase fringe pattern, i.e. to transform the phase wrapped modulo  $2\pi$  into a phase map without  $2\pi$  discontinuities. The unwrapped phase map contains information on the *fringe order* that is not explicitly contained in the wrapped phase fringe pattern. The task of unwrapping is therefore not trivial and can only be solved using assumptions and boundary conditions. The most important assumption is that the phase changes continuously over most of the image. Discontinuities in the wrapped phase are therefore treated as a change in the fringe order.

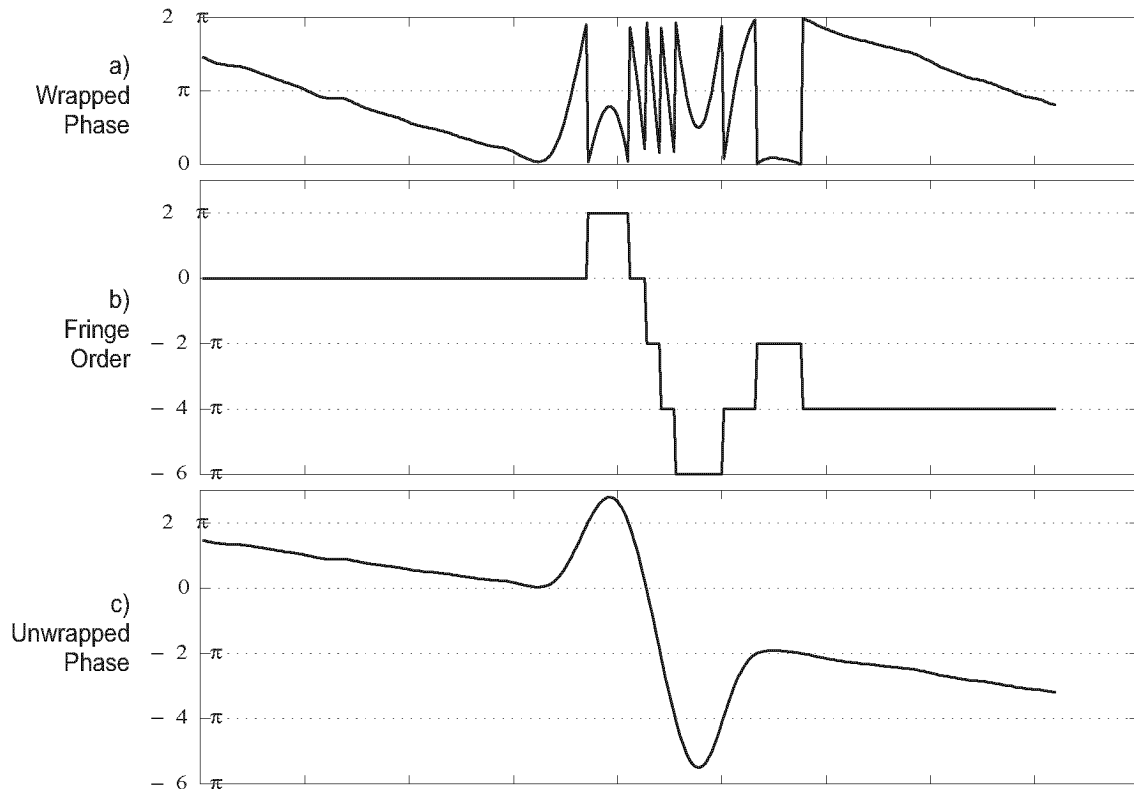
Line by line  
processing

Figure 4.6 illustrates the simplest phase unwrapping algorithm, where the image is processed line by line. The wrapped phase (figure 4.6 a) is a horizontal cut through the middle of figure 4.5 a). This curve is analysed by calculating the difference of neighbouring pixels. If the difference exceeds a certain threshold (e.g.  $\pm\pi/2$ ), the fringe order (figure 4.6 b) is increased or decreased by  $2\pi$ , depending on the sign of the difference. The curve of the unwrapped phase (figure 4.6 c) is then determined by adding the wrapped phase to the fringe order curve.

Evidently, this simple algorithm would fail if it was applied to more complex and less well filtered phase fringe patterns. If an object surface

contains a crack or a hole, the effective phase difference between the left and the right side may amount to several times  $2\pi$ . Still, the algorithm changes the fringe order by only  $\pm 2\pi$ , resulting in an error propagating along the rest of the line.

**Figure 4.6** Phase unwrapping along a horizontal line through figure 4.5. a) The wrapped phase; b) the fringe order determined from the  $2\pi$  phase discontinuities; c) the unwrapped phase resulting from the addition of the wrapped phase and the fringe order curve.



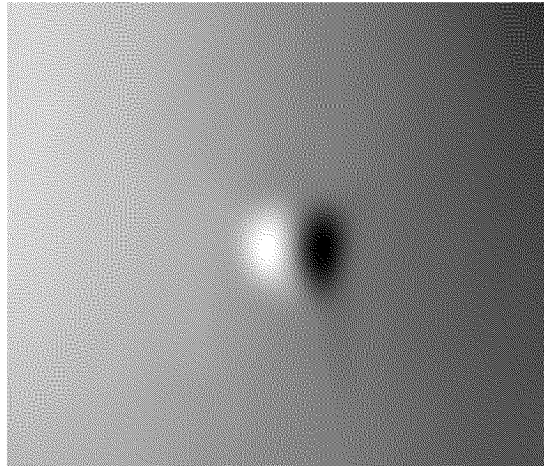
**Advanced algorithms** To overcome this problem, many advanced phase unwrapping algorithms have been developed. Reviews by Robinson [65], Osten and Jüptner [66], and Strand and Taxt [67] present interesting techniques, some of which are able to unwrap even noisy phase fringe patterns.

**Used for our experiments** To evaluate our measurements, we did not develop a particular unwrapping algorithm. We used the “Puzzle” algorithm implemented in PISA, which yielded good results on our phase fringe patterns. This algorithm divides the image into quadratic regions, called “Blocks”. The phase is first unwrapped within the individual blocks. Then, the phase of the whole block is adjusted such that the difference to the neighbouring blocks along its edges is minimized. In this way, unwrapping errors remain limited to one block and do not propagate further. It is also possible to mask out parts of the image which would cause unwrapping errors. The masked pixels are then ignored in the unwrapping process. The principal parameter for the unwrapping function is the size of the blocks. A small block size is recommended for noisy phase fringe patterns with corrupted fringes, a large block size can be applied to well filtered patterns.



Figure 4.7 shows the result of applying the Puzzle algorithm to figure 4.5. With an image size of  $410 \times 480$  pixels (width  $\times$  height), the block size was chosen to be 64 pixels. As the source image was almost perfectly filtered, the result shows no unwrapping errors.

**Figure 4.7** Result of unwrapping figure 4.5 using PISA's "Puzzle" algorithm.



**Scaling** For a quantitative analysis, the phase has to be converted to the physical quantity that was measured. For this purpose, the relation between phase change and mechanical deformation has to be known. These relations are given in sections 2.1.2 for speckle interferometry and section 2.1.3 for shearography and depend on the optical set-up (angles of illumination and observation, shear distance) and the laser wavelength. With the correct scaling, which may vary from pixel to pixel, the displacements in  $\mu\text{m}$  or the displacement derivatives in  $\%$  can directly be visualised and evaluated.

**Further processing** Is this all we have to know about quantitative evaluation? No, it is not! As shown in the derivation, the standard shearography equation (2.20) is based on simplifications, which have to be considered for accurate quantitative evaluation. Especially the approximation of the displacement difference by the displacement derivative is rather rough. Furthermore, we usually obtain a mixture of mechanical quantities from one measurement. It is not easy to interpret a result that consists of 40 %  $\partial u/\partial x$  and 60 %  $\partial w/\partial x$ . To these two problems we will address ourselves in the next two chapters "Removing the Image Doubling" and "Isolation of the Components".



# REMOVING THE IMAGE DOUBLING

This chapter presents a technique that solves the problem of image doubling in shearography. The method calculates the displacement field from the shearography result by taking into account the finite shear distance. Experiments on a simulated as well as on a measured fringe pattern demonstrate the efficiency of this method.<sup>1</sup>

## 5.1 Introduction

Shearography makes use of the interference of two images of the object, as outlined in section 2.1.3. This effects both advantages and drawbacks. Here, we want to mention two principal drawbacks:

- 1 The measured quantity is an approximation to the *displacement derivative* (according to eq. (2.20)), which is not as intuitively to interpret as the displacement field in speckle interferometry.
- 2 The two sheared images cause a *doubling of the image*, which impedes the matching of the measured phase map to the object geometry.

Problems for  
quantitative  
evaluation

These two arguments are the main reason, why – until today – shearography was used almost exclusively for qualitative purposes. The image doubling causes problems, as soon as details have to be resolved whose dimensions are comparable to  $\Delta x$ . This is the case in non-destructive testing if the size and location of relatively small flaws have to be determined [18, 70]. In experimental mechanics, the region of interest is often located around a crack tip, a notch, or a hole. In the experiments of Petzing and Tyrer [71] the crack tip appears twice in the image. This is not only confusing, it also makes it impossible to calculate the displacement derivatives precisely.

1. Most of the material in this section is taken from the publications “Removing the Image-Doubling in Shearography by Reconstruction of the Displacement Field” by S. Waldner [68] (Copyright © 1996 Elsevier Science B.V.) and “Removing the Image-Doubling in Shearography by Reconstruction of the Displacement Field – Theory and Application” by S. Waldner [69] (Copyright © 1996, The Society of Photo-Optical Instrumentation Engineers).

In this chapter, we present a simple procedure that allows for the reconstruction of the original displacement field, and which removes the doubling of the image.

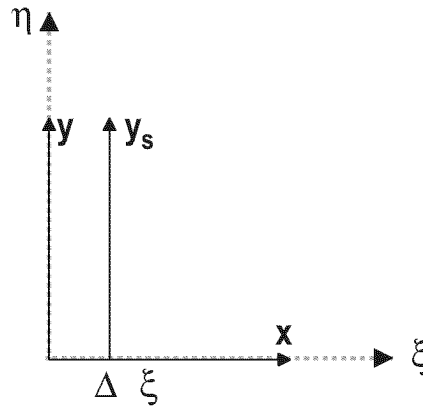
Two  
co-ordinate  
systems

To explain the nature of the image doubling and the technique of its removal, we introduce a second co-ordinate system. The *image co-ordinate system*  $(\xi, \eta)$  has its origin at the lower left corner of the image with the axes  $\xi$  in horizontal and  $\eta$  in vertical direction, respectively. The *z-axis* of the *object co-ordinate system*  $(x, y, z)$  is normal to the flat and diffusely reflecting object surface and its origin is defined in the following way: If the magnitude of the image shear is zero, the point  $x = y = z = 0$  is imaged at  $\xi = \eta = 0$ . The two co-ordinate systems are then related by

$$(\xi, \eta) = (x \cdot m_x, y \cdot m_y), \quad (5.1)$$

where  $m_x$  and  $m_y$  are the magnifications of the imaging system in  $x$  and  $y$  directions, respectively. By rotating one of the mirrors in the Michelson interferometer about the  $y$ -axis, the object point  $x = y = z = 0$  is imaged twice: at  $\xi = \eta = 0$  and at  $\xi = \Delta\xi, \eta = 0$ , where  $\Delta\xi$  is the shear distance in the image.  $\Delta x$  is the shear distance on the object related to  $\Delta\xi$  by the magnification  $m_x$ . Figure 5.1 illustrates how the object co-ordinate system is related to the image co-ordinate system.

**Figure 5.1** Illustration of the object and the image co-ordinate system. The origin of the object co-ordinate system appears twice in the image: at  $(\xi, \eta) = (0, 0)$  and at  $(\xi, \eta) = (\Delta\xi, 0)$ .



From the electronically recorded speckle patterns before and after the object is deformed, a phase change  $\Delta\phi(\xi, \eta)$  can be calculated, which, in the case of shearing in the  $x$ -direction, is given by

$$\Delta\phi(\xi, \eta) = k \cdot \{d(x, y) - d(x - \Delta x, y)\}, \quad (5.2)$$

in analogy to eq. (2.16). Usually eq. (5.2) is expanded into a Taylor series and then approximated to first order in  $\Delta x$  (see section 2.1.3 and [11, 39]), which yields eq. (2.20). In this way, the displacement difference is approximated by the displacement derivative.

Magnitude of  
the shear  
distance

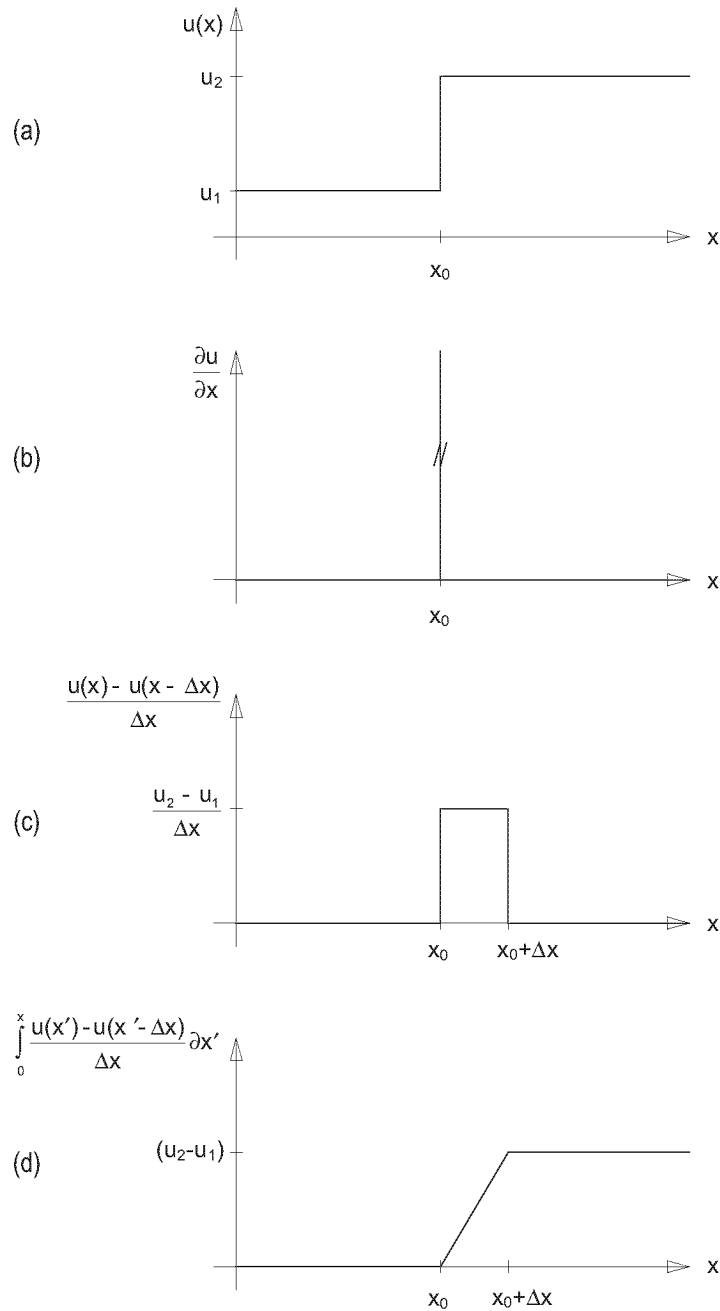
For a good approximation, the shear distance  $\Delta x$  has to be small; but by reducing the shear distance we also reduce the phase difference  $\Delta\phi(\xi, \eta)$ , i.e. the number of fringes. Depending on the experiment, the magnitude

of the shear distance is chosen to lie in the range of a few percent of the image width [72-74].

## 5.2 An Illustrative Example

The following example illustrates the effect of the image shear on the quantitative evaluation of shearographic measurements.

**Figure 5.2** An example to illustrate the effect of shear distance: (a) displacement of an idealized tensile specimen, (b) displacement derivative, (c) approximation to the displacement derivative as it would be measured by shearography, (d) integral of (c) showing that the step function in (a) is converted to a ramp.



**Idealized specimen** We assume a tensile specimen consisting of two very stiff parts (Young's modulus  $E \rightarrow \infty$ ) joined by a highly compliant part ( $E \rightarrow 0$ ) that is infinitesimally small.

If this idealized specimen is subjected to a force in the  $x$ -direction, the displacement  $u(x)$  will be as shown in figure 5.2(a). Figure 5.2(b) shows the corresponding strain in the  $x$ -direction. It is represented by a delta-function that is located at the interface of the two rigid parts. This would also be the result of a shearographic measurement if eq. (2.20) was valid. In reality, shearography does not measure the displacement derivative but an *approximation*: the difference of the displacements at two points on the object which are separated by the finite shear distance  $\Delta x$ , according to equation (5.2). In our example, this has the effect that the delta-function of figure 5.2(b) is converted to a rectangle function with the width of the shear distance, as shown in figure 5.2(c). Obviously, the discontinuity, which is located at  $x_0$ , appears twice.

According to equation (2.20), it should be possible to determine the displacement field (cf. figure 5.2(a)) by *integrating* the shearogram in the  $x$ -direction. As equation (2.20) is only an approximation to the phase differences measured in shearography (figure 5.2(c)), the result of the integration (figure 5.2(d)) is also approximative with the effect of the finite shear distance still present. Instead of the step function of figure 5.2(a), a ramp with the length  $\Delta x$  appears.

In the following section a solution to this problem is presented.

## 5.3 Description of the Method

The phase difference measured with shearography in a certain image point  $(\xi, \eta)$  is given by eq. (5.2). This means that the displacements of the object points  $(x, y)$  and  $(x - \Delta x, y)$  contribute to the phase change. At the image point  $(\xi - \Delta \xi, \eta)$ , the phase difference becomes

$$\Delta\varphi(\xi - \Delta\xi, \eta) = k \cdot \{d(x - \Delta x, y) - d(x - 2\Delta x, y)\}. \quad (5.3)$$

By adding the two phase differences of eqs. (5.2) and (5.3), the displacement  $d(x - \Delta x, y)$  that appears in both equations is eliminated and the result is

$$\Delta\varphi(\xi, \eta) + \Delta\varphi(\xi - \Delta\xi, \eta) = k \cdot \{d(x, y) - d(x - 2\Delta x, y)\}. \quad (5.4)$$

Adding the phase values of *all image points* lying at an integral multiple of  $\Delta \xi$  away from  $\xi$  between  $\xi$  and zero in the negative  $\xi$ -direction, as illustrated in figure 5.3, we obtain

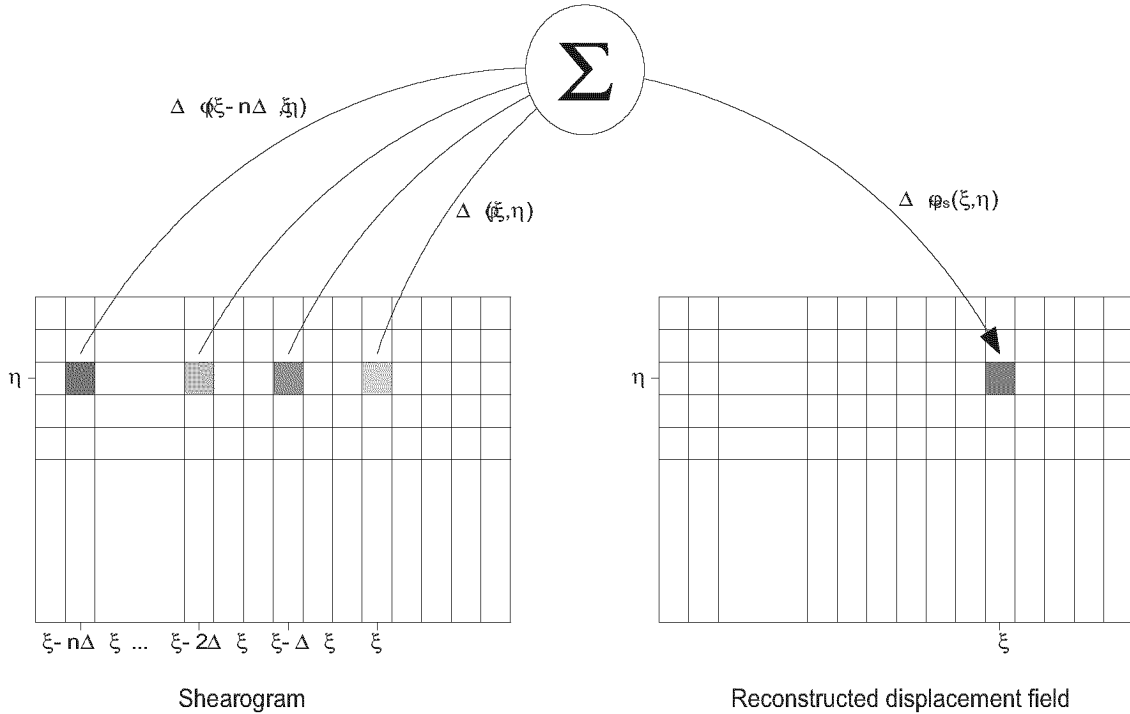
$$\sum_{j=0}^n \Delta\varphi(\xi - j\Delta\xi, \eta) = k \cdot \{d(x, y) - d(x - (n+1)\Delta x, y)\};$$

$$n = [\xi/(\Delta\xi)]. \quad (5.5)$$

where  $[\xi/(\Delta\xi)]$  means rounding to the closest integer to  $(\xi/(\Delta\xi))$  between zero and  $(\xi/(\Delta\xi))$ . In other words:  $n$  is the number of shear

distances  $\Delta\xi$  that can be placed between  $\xi$  and zero. Only the displacements of the object points  $(x, y)$  and  $(x - \{n+1\}\Delta x, y)$  contribute to the result of the summation, whereas the displacements of all the object points in between are *eliminated*. In other words: What we obtain is the displacement of point  $(x, y)$  relative to point  $(x - \{n+1\}\Delta x, y)$ , i.e. to a point near the image border.

**Figure 5.3** The phase value at the image co-ordinate  $(\xi, \eta)$  in the displacement field is reconstructed by adding the phase values at  $(\xi, \eta)$ ,  $(\xi - \Delta\xi, \eta)$ ,  $(\xi - 2\Delta\xi, \eta)$ , ...,  $(\xi - n\Delta\xi, \eta)$  in the shearographic source image.  $n$  is the number of shear distances that can be placed between  $\xi$  and the image border.



**Further simplification**

In order to further simplify the result of the summation, the term  $d(x - (n+1)\Delta x, y)$  has to be zero. This can be achieved if the area between zero and  $-\Delta x$  in the object co-ordinate system (as defined in the introducing section) is not deformed, as illustrated in figure 5.4. This is the case if the specimen is *clamped* along one edge and positioned such that only the part at  $x > 0$  is deformed. If clamping along one edge of the object can not be ensured, it is possible to put a *reference plane* that is not loaded – and consequently not deformed – right in front of the object at the position indicated in figure 5.4.

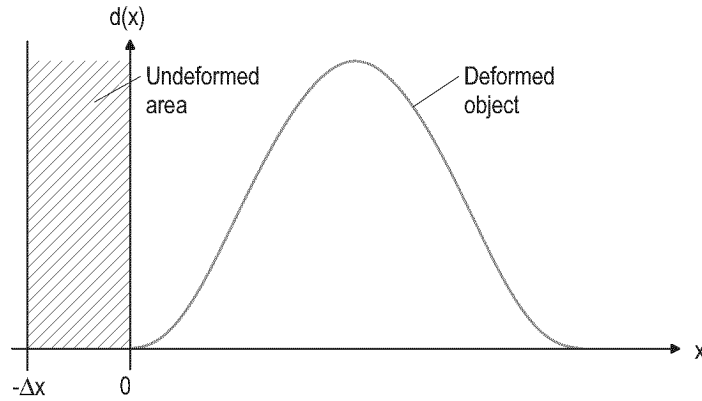
With this boundary condition fulfilled, eq. (5.5) simplifies to

$$\begin{aligned} \Delta\varphi_{res}(\xi, \eta) &= \sum_{j=0}^n \Delta\varphi(\xi - j\Delta\xi, \eta) = \mathbf{k} \cdot \mathbf{d}(x, y) \\ &= k_x \cdot u(x, y) + k_y \cdot v(x, y) + k_z \cdot w(x, y) \end{aligned} \quad (5.6)$$

**Displacement – independent of shear distance**

It is obvious that the result of the summation  $\Delta\varphi_{res}(\xi, \eta)$  contains the components of the displacement vector and not the displacement gradient, and that this displacement is independent of the shear distance.

**Figure 5.4** The area between zero and  $-\Delta x$  in the object co-ordinate system must not be deformed.



For the implementation of the method in a computer program, the summation in eq. (5.6) has to be programmed, as illustrated in figure 5.3. The value of the phase difference at the point  $(\xi, \eta)$  in the reconstructed displacement field is the sum of the phase values of the corresponding point in the shearogram and at all the points that are located at a distance equal to an integral multiple of the shear distance  $\Delta\xi$  away from  $\xi$  between  $\xi$  and zero in the negative  $\xi$ -direction. Applying this summation to each image point  $(\xi, \eta)$ , the whole displacement field is reconstructed.

To reconstruct the displacement field from a digitally stored shearogram, one has to know the shear distance  $\Delta\xi$  that was used for the recording and the relation between the phase values and the grey levels in the image (e.g. in figure 5.6, grey level 127 corresponds to phase 0).

**Special case**  
 $n = 0$  As a special case of this method, the shear distance  $\Delta\xi$  can be chosen to be larger than the image width [75]. Then the object is superposed on a reference plane and the measurement yields the displacement information directly, since  $n$  is equal to zero in eq. (5.5). This arrangement is equivalent to a speckle interferometer as shown in figure 2.5. This approach has the drawbacks that an area twice as large as the object has to be illuminated and that the measurement sensitivity can not be influenced by the shear distance.

## 5.4 Experimental Results

The first experiment was performed with a calculated phase fringe pattern. A program was written that simulates the shearographic measurement of the out-of-plane deformation of a clamped circular plate. Assuming the directions of observation and illumination being normal to the object surface, eq. (5.2) becomes

$$\Delta\phi(\xi, \eta) = \frac{4\pi}{\lambda} \cdot \{w(x, y) - w(x - \Delta x, y)\}. \quad (5.7)$$

The out-of-plane displacement  $w(x, y)$  of a clamped circular plate which is displaced by a distance  $w_{max}$  at the centre is given by [76]



$$w(r) = \frac{2w_{max}}{a^2} \left\{ r^2 \cdot \log \frac{r}{a} + \frac{1}{2} \cdot (a^2 - r^2) \right\}, \quad (5.8)$$

with  $r^2 = x^2 + y^2$  and  $a$  the radius of the plate.

Simulated  
phase fringe  
pattern

The phase fringe pattern shown in figure 5.5 was calculated by evaluating eqs. (5.7) and (5.8) for  $512 \times 512$  pixels. The constants  $a = 70$  mm,  $w_{max} = 1 \mu\text{m}$ ,  $\lambda = 632.8$  nm,  $\Delta x = 50$  mm, an imaged width of 200 mm and an imaged height of 150 mm were used. The phase modulo  $2\pi$  was coded in 256 grey levels. The shear distance was chosen to be exceptionally large ( $1/4$  of the image width) in order to demonstrate the effect of the proposed method.

**Figure 5.5** Simulated shearographic phase fringe pattern of a clamped circular plate loaded at its centre. The shear distance is  $1/4$  of the image width.

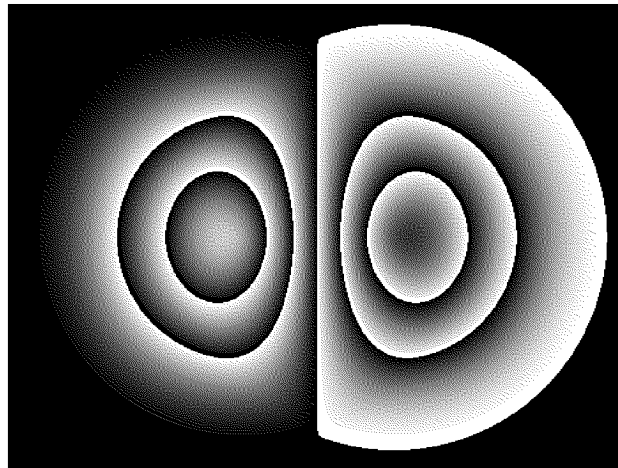
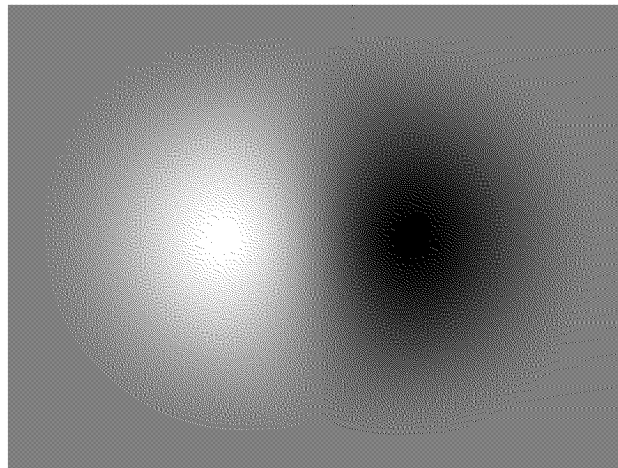


**Figure 5.6** The unwrapped phase image of the phase fringe pattern in figure 5.5.

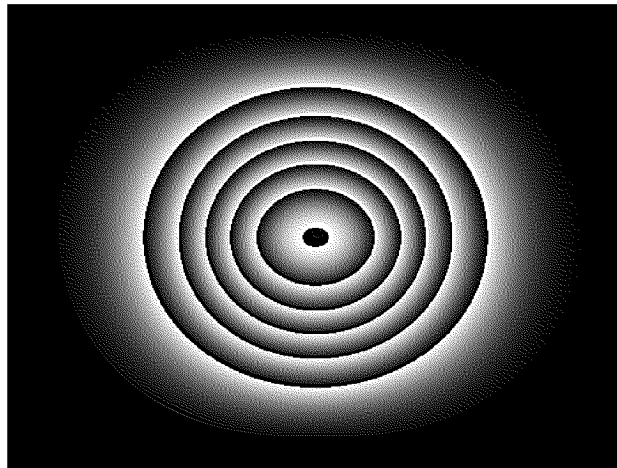


Applying a phase unwrapping algorithm (see section 4.6) to the phase fringe pattern in figure 5.5 resulted in figure 5.6. The method would also work without phase unwrapping, but the sensitivity (the number of fringes) in the resulting image is then defined by the ESPI formulas (2.8), (2.12). The variation of the sensitivity by altering the shear distance, which is a big advantage of shearography, is then neutralized by the

method. This can be circumvented by unwrapping the original shearography result.

By numerically integrating the unwrapped image of figure 5.6 in the  $\xi$ -direction and representing the integrated phase modulo  $2\pi$ , figure 5.7 is obtained. The phase fringe pattern resembles the out-of-plane displacement, but its outline is distorted by the image shear. Instead of being a circle, the outline is an ellipse that has the size of the doubled circular plate. Thus, the displacement fringes cannot be exactly related to the geometry of the plate.

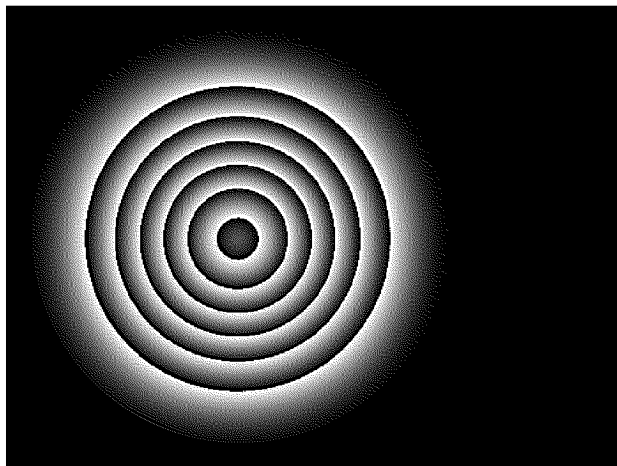
**Figure 5.7** Integration of the phase image (figure 5.6) in the  $\xi$ -direction results in an approximation to the displacement field. The finite shear distance causes the stretching of the fringes in the  $\xi$ -direction (the wrapped phase is shown for better visualization).



Nearly perfect  
displacement  
field

As theoretically shown in the previous section, our new method does not have this drawback. Applying the method to the unwrapped image (figure 5.6) results in the phase distribution of figure 5.8 (the wrapped phase is shown). It is an almost perfect reconstruction of the out-of-plane displacement field of the clamped circular plate.

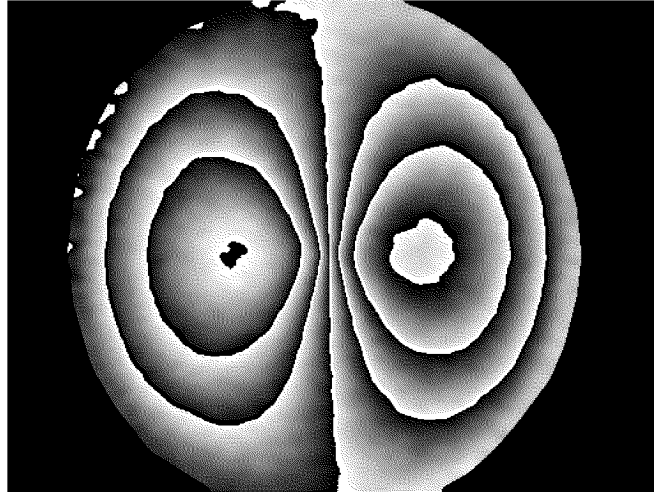
**Figure 5.8** Result of the procedure described above applied to the unwrapped phase image in figure 5.6: The displacement field is exactly reconstructed and the influence of the shear distance is no longer visible, i.e. the image-doubling has disappeared.



Measured  
phase fringe  
pattern

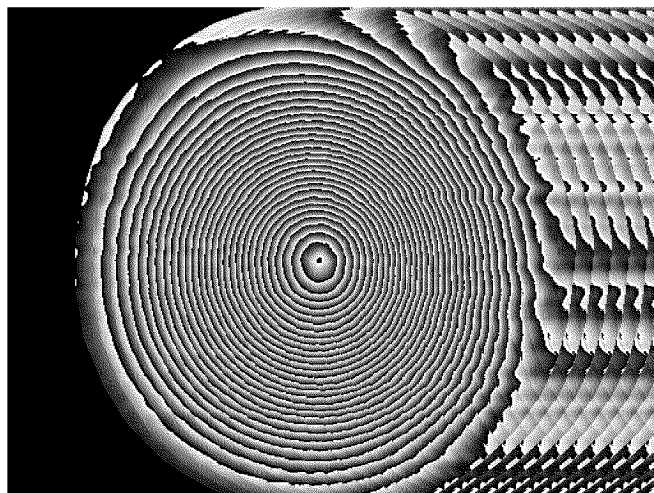
For the second experiment we made the step from the idealized simulated shearogram to a real shearographic measurement. A clamped circular plate with the same parameters as for the calculated fringe pattern was used, except the shear distance was reduced to  $\Delta x = 5$  mm and the displacement at the centre was increased to  $w_{max} = 10$   $\mu\text{m}$ . This corresponds to a practical measurement set-up.

**Figure 5.9** Measured shearographic phase fringe pattern of a clamped circular plate loaded at its centre after filtering and masking. The shear distance is 5 mm.



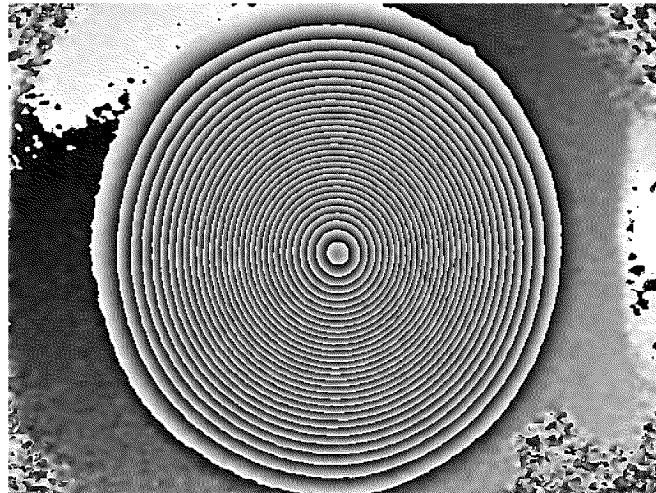
A set-up similar to that shown in figure 2.11 was used. The direction of observation was perpendicular to the object surface, whereas the angle between the directions of illumination and observation in our experiment was  $10^\circ$ . Figure 5.9 shows the measured phase fringe pattern after moderate filtering and masking. The filtering improved the fringe quality, but left some speckle noise and the masking set the grey levels of all the pixels outside the plate diameter to zero. (A simple isotropic filter was used, because this work was done before we developed the filter presented in chapter 4.)

**Figure 5.10** Reconstruction of the displacement field from the unwrapped phase image according to the proposed method. Within the diameter of the plate the result is qualitatively good.



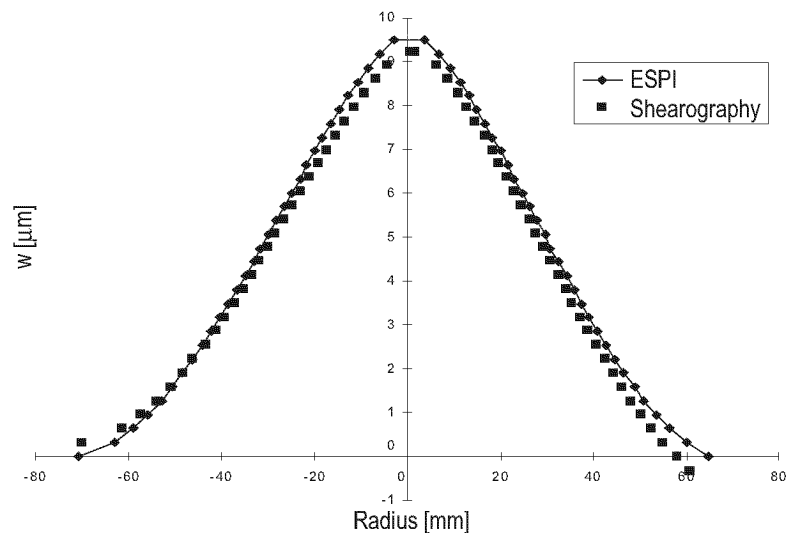
After unwrapping of the phase fringe pattern, the displacement field was reconstructed as described above. Figure 5.10 shows the result: The out-of-plane displacement is represented by concentric fringes of high quality. Due to the summation procedure, errors in the phase image are passed on to the right and appear repeatedly in the resulting image.

**Figure 5.11** ESPI displacement measurement on the same plate.



For comparison, the same object was measured with out-of-plane ESPI. The phase fringe pattern is shown in figure 5.11. Now the displacement field calculated from the shearographic measurement (figure 5.10) can be compared with the one resulting from ESPI measurement (figure 5.11). In both images the displacement along the horizontal line through the centre of the plate was determined. Figure 5.12 shows the good agreement of the two methods. The maximum difference between the two results amounts to 5 % of the peak displacement.

**Figure 5.12** Comparison of the shearographic measurement (figure 5.10) and the ESPI measurement (figure 5.11). The displacement was evaluated along a horizontal line through the centre of the plate.



## 5.5 Conclusions

---

We have described a method that calculates the displacement field from shearographic recordings. The first experiments showed that the displacement field is correctly reconstructed and that the effect of the shear distance (i.e. the doubling of the image) is eliminated.

The proposed method combines some advantages of electronic speckle pattern interferometry (ESPI) with those of shearography:

- As in ESPI the resulting fringe pattern represents the displacement and not an approximation to the displacement derivative. Therefore, it is easier to interpret and to quantitatively evaluate the fringes.
- As in shearography, only a single illuminating beam is necessary. This means that the susceptibility to vibrations is much smaller than in ESPI and that the coherence length of the laser does not need to be large.
- The measurement sensitivity of the shearographic recording can be adapted to the measurement problem by varying the shear distance. As shown in the experiments, the displacement field can be reconstructed from shearograms with a large as well as with a small shear distance.

In other words, shearography in combination with the method to reconstruct the displacement field is the realisation of “single-beam ESPI”.

## 5.6 Alternative Methods

---

**Two direction algorithm** In his thesis [77], T. Lamarque implemented our method and proposed an improved version. His algorithm works from both left and right side towards the centre of the image. The errors on one side of the image (see figure 5.10) can be avoided in this way. To achieve this, an additional boundary condition is necessary: The object may not be deformed (or has to be masked) on both sides.

**Frequency domain method** Maas and Somers chose a different approach [78]: They modelled the phase change measured with shearography as the convolution of a displacement measurement with a ‘phase point spread function’. Via transformation to the frequency domain, the displacement field can be determined. The boundary condition of an undeformed border is not necessary for this technique, but two measurements with different shear directions (but with the same deformation) have to be performed.

These two methods as well as our method serve for the same purpose: They calculate the displacement field from a shearography measurement and remove the effect of image-doubling. In this way, shearography results can be quantitatively evaluated in the same way as ESPI results.



## ISOLATION OF THE COMPONENTS

This chapter presents a simple optical set-up with three light sources arranged in a particular symmetry and an associated procedure which allows to isolate all six displacement derivatives which can contribute to the formation of fringes in shearography. The method uses the phase-shifting technique and is demonstrated on the deformation of a rectangular tensile specimen with a central hole. The measured in-plane strain components are compared with the results of a finite element analysis. High quality fringe patterns are obtained which reveal even localized strain concentrations.<sup>1</sup>

### 6.1 Introduction

As derived in section 2.1.3, the first order approximation to the phase difference  $\Delta\varphi(x, y)$  measured between the deformed and the undeformed state of the object can be written in the form

$$\Delta\varphi = \mathbf{k} \cdot \frac{\partial \mathbf{d}}{\partial \mathbf{x}} \cdot \Delta \mathbf{x} = \left( k_x \cdot \frac{\partial u}{\partial x} + k_y \cdot \frac{\partial v}{\partial x} + k_z \cdot \frac{\partial w}{\partial x} \right) \Delta x. \quad (6.1)$$

The components of the sensitivity vector  $\mathbf{k}$  do not depend on  $x$  and  $y$  if the object is illuminated by a plane wave.

Variation of the illumination angle

If we choose the wave vector  $\mathbf{k}_s$  of the illuminating plane wave to lie in the  $x$ - $z$  plane (with its angle of incidence relative to the surface normal denoted by  $\theta_s$ ), and the observing direction to lie in the  $z$  direction, then we get

$$\Delta\varphi = \frac{2\pi}{\lambda} \cdot \left[ \pm \sin \theta_s \cdot \frac{\partial u}{\partial x} + (1 + \cos \theta_s) \cdot \frac{\partial w}{\partial x} \right] \cdot \Delta x. \quad (6.2)$$

1. Most of the material in this section is taken from the publication “Strain Distributions Made Visible with Image-Shearing Speckle Pattern Interferometry” by H. A. Aebischer and S. Waldner [20] (Copyright © 1996 Elsevier Science Ltd.).

It is clear from eq. (6.2) that, if  $\theta_s$  is chosen to be small, then  $\Delta\phi$  will approximately be proportional to the out-of-plane displacement derivative  $\partial w/\partial x$ , while the in-plane term  $\sin\theta_s(\partial u/\partial x)$  can be neglected. On the other hand, whatever value for the incident angle  $\theta_s$  we choose between  $-90^\circ$  and  $90^\circ$ , we can never neglect the out-of-plane term in favour of measuring the in-plane displacement derivative  $\partial u/\partial x$ . This being said, it is not surprising that shearography has so far mainly been used to measure *out-of-plane* displacement derivatives [11, 12, 18, 19, 79, 80], and that only few authors have tried to visualize or even measure *in-plane* displacement derivatives.

**Hung & Taylor method** The standard method to isolate a particular derivative was originally proposed by Hung and Taylor [12]. Three measurements have to be taken at three different directions of illumination. These result in a system of three equations for the three phase differences in the three unknowns  $\partial u/\partial x$ ,  $\partial v/\partial x$ , and  $\partial w/\partial x$  for every pixel. By solving these systems of equations pixel by pixel, the phase fringe patterns representing the distributions of the three derivatives  $\partial u/\partial x$ ,  $\partial v/\partial x$ , and  $\partial w/\partial x$  can be constructed. It should be stated here that at the time when Hung and Taylor published this method, the technique for measuring the phase was not known yet. The phase had to be estimated from intensity fringe patterns by counting fringe orders, which had to be done “by hand”, image point by image point, before the systems of equations could be solved. Nowadays, with the phase measuring technique available, the phase data can be acquired by means of a computer which then solves the corresponding systems of equations. To our knowledge, however, this method has not been applied so far. It still is desirable to have a simpler and quicker method for the measurement of in-plane displacement derivatives.

**Steinchen method** Steinchen et al. [81] tried to isolate the in-plane displacement derivative  $\partial u/\partial x$  using oblique directions for both the illumination and the observation. But the suppression of the out-of-plane component that can be achieved in this way is rather limited: In their experiments,  $k_x$  was only about three times as large as  $k_z$ . Besides, viewing the object at an oblique angle has the disadvantage of shortening the width of the image.

**Petzing & Tyrer method** Petzing and Tyrer [71] tried to reduce the sensitivity to the out-of-plane displacement derivative by simultaneously illuminating the specimen symmetrically with respect to the  $y$ - $z$  plane, and observing the object in the  $z$  direction. This method is easy to realize and, in fact, it had the desired effect of suppressing the out-of-plane component, but it also reduced the fringe contrast to the very limit of visibility.

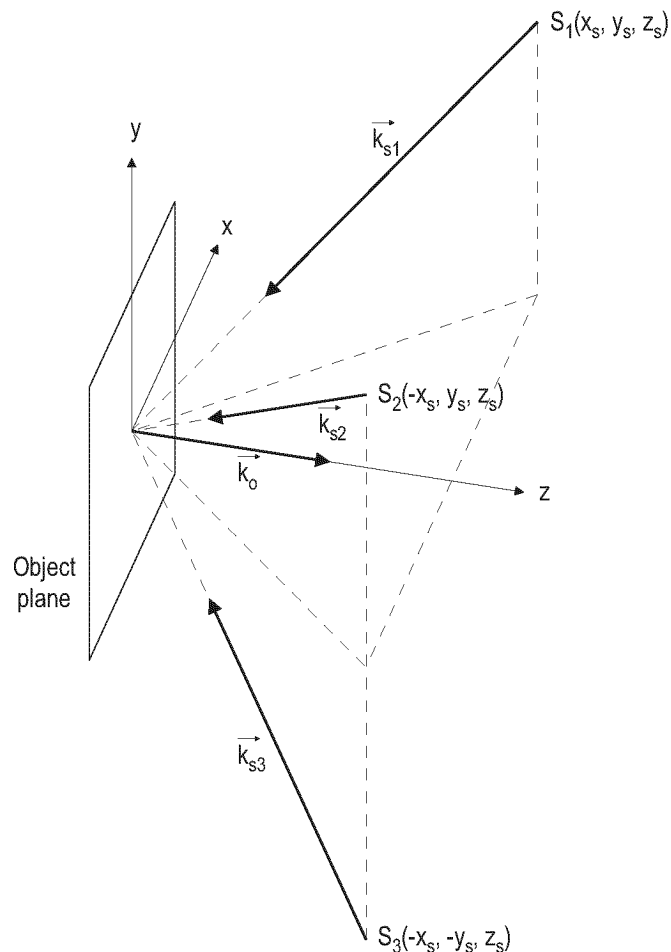
In this chapter we present a simple method which allows to isolate any of the displacement derivatives  $\partial u/\partial x$ ,  $\partial v/\partial x$ , and  $\partial w/\partial x$  quickly and accurately and which does not degrade the contrast of the fringe patterns. If the image shear is applied in the  $y$  direction, then  $\partial u/\partial y$ ,  $\partial v/\partial y$ , and  $\partial w/\partial y$  can be isolated in the same way. In section 6.2, the method is described in detail. In section 6.3, we explain the actual set-up and the test specimen we used to carry out our experiments. We used a simplified



version here with only two light sources instead of three. Consequently, only a subset of all six displacement derivatives could be isolated, but nevertheless, these experiments demonstrate without loss of generality that the isolation procedure works. In section 6.4 we discuss our experimental results and validate them by comparison with distributions of strain obtained with finite element calculations. At the end of this chapter we expose our conclusions.

## 6.2 Description of the Method

**Figure 6.1** The geometrical arrangement of the three light sources and their corresponding wave vectors in the general optical set-up.



The basic idea behind our method [20] originates from a special case of the standard method of isolation (Hung & Taylor). Here, the directions of illumination are chosen in a particular symmetry so that the resulting system of equations can be solved by simply adding and subtracting its equations as evidenced by the formulas (6.6) and (6.7). Due to the technique of recording phase fringe patterns [82] (rather than simple intensity fringe patterns) it is possible to evaluate these equations very efficiently (by simply adding and subtracting whole phase fringe patterns modulo  $2\pi$ ). Our method also resembles the one used by Petzing and

Tyrer [71], only that in our case the illuminating beams are switched on consecutively and not simultaneously.

We choose the direction of observation to lie in the z-direction:

$$\mathbf{k}_o = (0, 0, k_{oz}) \quad (6.3)$$

We introduce three different sources  $S_1$ ,  $S_2$ , and  $S_3$  of plane waves which consecutively illuminate the object with light of the same wavelength, see figure 6.1. These light sources are arranged in a particular symmetry based on the coordinates  $x_s$ ,  $y_s$ , and  $z_s$ , namely  $S_1(x_s, y_s, z_s)$ ,  $S_2(-x_s, y_s, z_s)$ , and  $S_3(-x_s, -y_s, z_s)$ . The central light beams of all three sources are directed towards the origin of the coordinate system. The wave vectors then display the following symmetry:

$$\begin{aligned} \mathbf{k}_{s1} &= (-k_{sx}, -k_{sy}, -k_{sz}) \\ \mathbf{k}_{s2} &= (k_{sx}, -k_{sy}, -k_{sz}) \\ \mathbf{k}_{s3} &= (k_{sx}, k_{sy}, -k_{sz}) \end{aligned} \quad (6.4)$$

The resulting sensitivity vector  $\mathbf{k}_i$  belonging to the light source  $S_i$  is given by

$$\mathbf{k}_i = \mathbf{k}_{si} - \mathbf{k}_o; (i = 1, 2, 3) \quad (6.5)$$

**Sensitivity vectors** For each  $i = 1, 2, 3$  a phase fringe pattern  $B_i$  is recorded with the corresponding sensitivity vector  $\mathbf{k}_i$  (where  $k_x = -k_{sx}$ ,  $k_y = -k_{sy}$ , and  $k_z = -k_{sz} - k_{oz}$ ) by turning on the light source  $S_i$ :

$$\begin{aligned} B_1: \quad \mathbf{k}_1 &= (k_x, k_y, k_z) \\ B_2: \quad \mathbf{k}_2 &= (-k_x, k_y, k_z) \\ B_3: \quad \mathbf{k}_3 &= (-k_x, -k_y, k_z) \end{aligned} \quad (6.6)$$

**Isolation** By simply adding and subtracting the phase fringe patterns  $B_i$  modulo  $2\pi$ , it is now possible to isolate any of the approximated displacement derivatives  $\partial u/\partial x$ ,  $\partial v/\partial x$ , and  $\partial w/\partial x$  in the following way:

$$\begin{aligned} B_1 - B_2: \quad (\Delta\varphi)_x &= 2k_x \cdot \frac{\partial u}{\partial x} \cdot \Delta x \\ B_2 - B_3: \quad (\Delta\varphi)_y &= 2k_y \cdot \frac{\partial v}{\partial x} \cdot \Delta x \\ B_1 + B_3: \quad (\Delta\varphi)_z &= 2k_z \cdot \frac{\partial w}{\partial x} \cdot \Delta x \end{aligned} \quad (6.7)$$

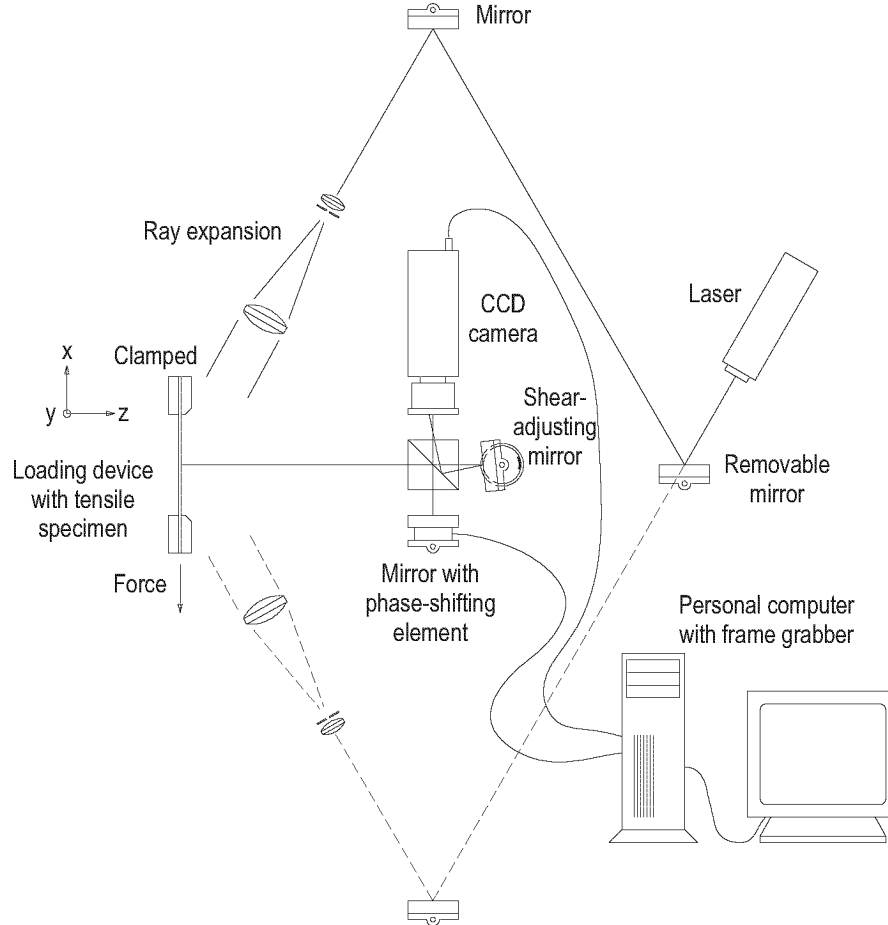
In a way, our method is a synthesis of the methods of Hung & Taylor and of Petzing & Tyrer. It provides the advantages of both without inheriting their disadvantages.

**Shear in y direction** In order to measure the derivatives  $\partial u/\partial y$ ,  $\partial v/\partial y$ , and  $\partial w/\partial y$ , no change in the optical set-up is required. It suffices to apply the image

shear in the  $y$  direction. This can be accomplished by slightly rotating one of the mirrors in the interferometer about the second axis.

## 6.3 Experimental Details

**Figure 6.2** The optical set-up used in our experiments. The object is illuminated consecutively from the right- and the left-hand side to record the phase fringe patterns  $B_1$  and  $B_2$ , respectively.



**Simplified set-up** The optical set-up used in our experiments is shown in figure 6.2. It is a simplified version of the general set-up which is shown in figure 6.1. In contrast to the general method of isolation as described in the preceding section, only two light sources were used in our experiments, so that the sensitivity vector component  $k_y = 0$ . This set-up allowed to isolate  $\partial u / \partial x$  and  $\partial w / \partial x$  in the following way:

$$\begin{aligned}
 B_1 - B_2: (\Delta\phi)_x &= 2k_x \cdot \frac{\partial u}{\partial x} \cdot \Delta x \\
 B_1 + B_2: (\Delta\phi)_z &= 2k_z \cdot \frac{\partial w}{\partial x} \cdot \Delta x
 \end{aligned}
 \tag{6.8}$$

By rotating the object (with the coordinate system fixed to it) and the camera (but not the shearing device) by  $90^\circ$  about the optical axis, also

the derivative  $\partial v/\partial y$  could be isolated. Equations (6.8) accordingly change to

$$\begin{aligned} B_1 - B_2: (\Delta\varphi)_y &= 2k_y \cdot \frac{\partial v}{\partial y} \cdot \Delta y \\ B_1 + B_2: (\Delta\varphi)_z &= 2k_z \cdot \frac{\partial w}{\partial y} \cdot \Delta y \end{aligned} \quad (6.9)$$

Note that in the case where the full set-up with three light sources is used, no change in the optical set-up like rotating the object etc. is required for isolating the derivatives by  $y$ , as was described in the previous section.

- Set-up details** A HeNe-Laser with a power of 35 mW illuminated the object either from the right- or the left-hand side (for recording the phase fringe pattern  $B_1$  or  $B_2$ , respectively), depending on the presence or absence of a removable mirror (see figure 6.2). The object was observed by means of a CCD camera with a resolution of  $512 \times 512$  pixels through a Michelson interferometer, which acted as the shearing device and consisted of two mirrors and a beam splitter. By slightly rotating one of the mirrors about the vertical axis, the amount of shear could be adjusted. The second mirror was fixed to a piezo element to induce the phase shift. A personal computer acquired and processed the images and controlled the phase-shifting element.
- Test object** The test object was a tensile specimen of 75 mm length, 40 mm width and 1.8 mm thickness, containing a central hole with a diameter of 10 mm. It was made from carbon fibre reinforced plastic (CFRP) T300/PEI with a stacking sequence  $((0, 90)_2)_s$ . A pneumatic tensile device applied a force on the left-hand side of the specimen predominantly (but not exclusively) in the negative  $x$  direction, while the other end of the specimen was clamped (see figure 6.2). To obtain high fringe quality, the addition of incremental images as described by Floureur [6] was applied (see also section 7.1.1). The test specimen was deformed in six steps. The resulting phase fringe patterns were all filtered and added modulo  $2\pi$  (a simple isotropic filter was used, because this work was completed before we developed the filter presented in chapter 4). For clarity the holes were masked black in the phase fringe patterns. In our experiments the loading-force was about 2000 N in all cases. The shear distances  $\Delta x$  and  $\Delta y$  on the object were 5 mm, and the angle of incidence  $\theta_s$  was  $\pm 60^\circ$ .

## 6.4 Results and Discussion

- Isolation of in-plane strain** Figure 6.3 shows the phase fringe pattern  $B_1$ , and figure 6.4 shows  $B_2$ , both according to equations (6.6). They represent fringes resulting from a superposition of the two displacement derivatives  $\partial u/\partial x$  and  $\partial w/\partial x$ . The part  $\partial v/\partial x$  is absent in the patterns  $B_1$  and  $B_2$  owing to the special case of illumination where the component  $k_y$  of the sensitivity vectors  $\mathbf{k}_1$  and  $\mathbf{k}_2$  is zero.  $B_1$  and  $B_2$  represent fringe patterns as may occur in a real industrial measuring situation where the application of a practical load causes deformations of the specimen in different directions. In our case,

the tensile device caused a deformation that was not entirely in-plane with the specimen, but it produced a rather large component in the out-of-plane direction as well. The two superposed displacement derivatives can be accurately isolated according to equations (6.8). Figure 6.5 shows the isolated distribution of the approximation to  $\partial u/\partial x$ . The shape of the fringes can be compared with the result of the finite element analysis [83, 84] of the strain in  $x$  direction in figure 6.6, which shows a good agreement.

**Figure 6.3** The phase fringe pattern  $B_1$  of a deformed rectangular specimen with a central hole, illuminated from the right-hand side (i.e. from the half-space with positive  $x$  coordinate).

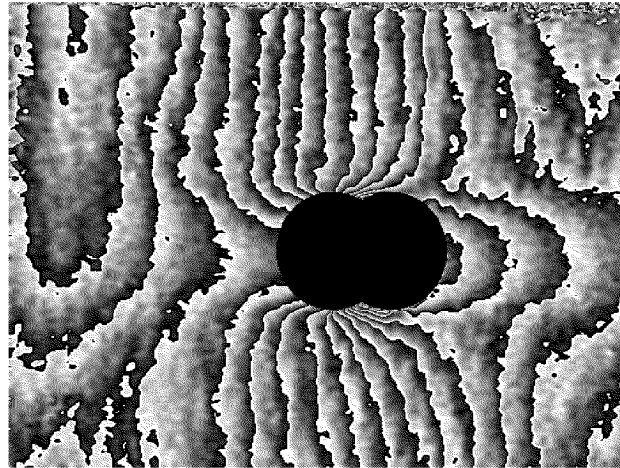
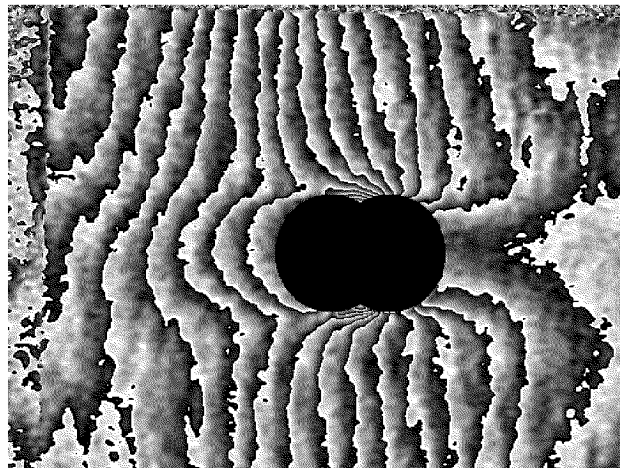


**Figure 6.4** The phase fringe pattern  $B_2$  of the same specimen as in figure 6.3, illuminated from the left-hand side.

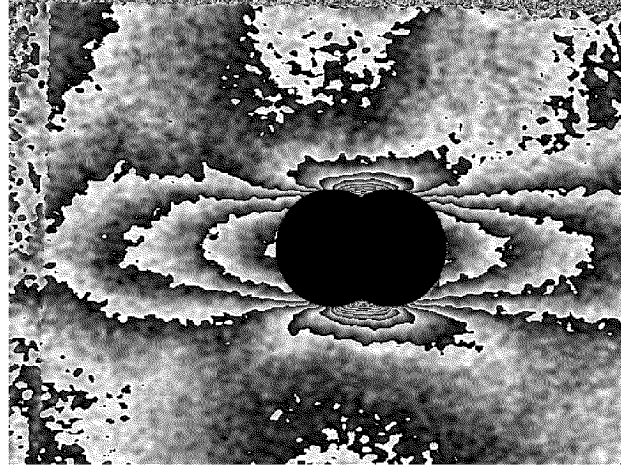


The influence of the hole on the strain distribution shows up clearly in figure 6.5 and figure 6.6. High values of strain are concentrated immediately above and below the hole, whereas the zones to the left and right of the hole are relieved from stress. The calculated maximum strain is about four times as high as in the regions that are not influenced by the hole, i.e. on the bottom and at the top of the specimen. To the left and right of the hole the strain tends towards zero as one approaches the hole.

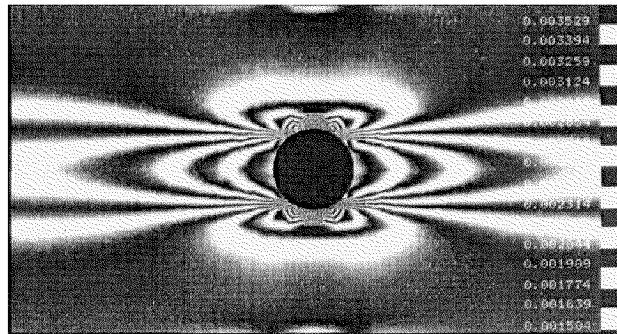
Out-of-plane  
contribution

Figure 6.7 represents the isolated distribution of  $\partial w/\partial x$  which, in our case, is a side effect of our pneumatic tensile device (see section 8.1.4).

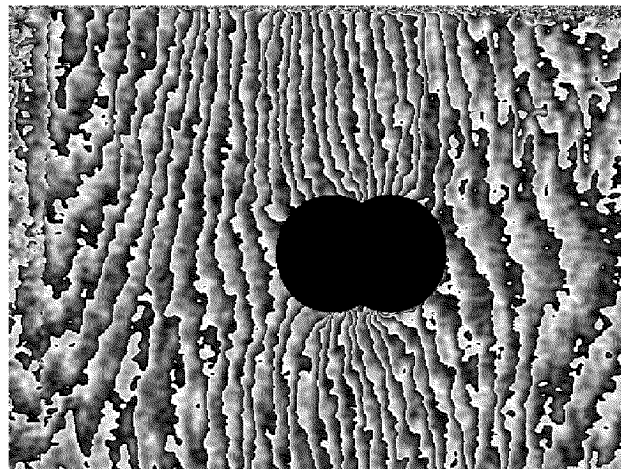
**Figure 6.5** This phase fringe pattern shows the distribution of the approximation to the displacement derivative  $\partial u/\partial x$ . It was isolated from the patterns  $B_1$  and  $B_2$  in figure 6.3 and figure 6.4. It represents the strain in the specimen in  $x$  direction.



**Figure 6.6** The calculated distribution of the strain  $\epsilon_x$  in  $x$  direction (Finite element calculations courtesy of Dr. Torsten Flemming).



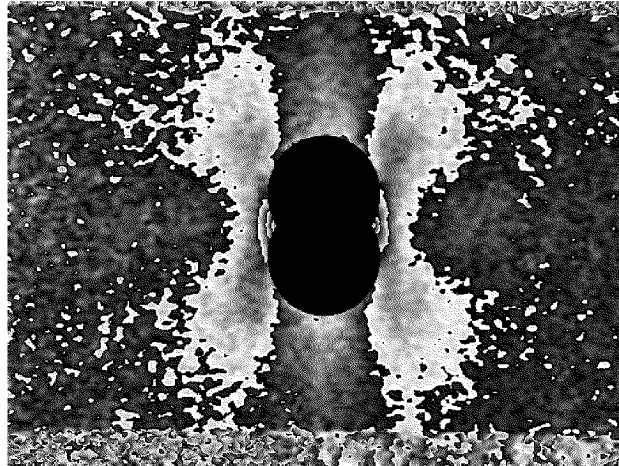
**Figure 6.7** This phase fringe pattern shows the distribution of the out-of-plane displacement derivative  $\partial w/\partial x$  as it was isolated from the patterns  $B_1$  and  $B_2$  in figure 6.3 and figure 6.4.



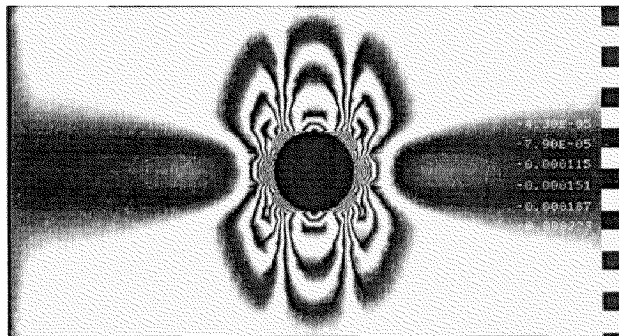
$y$  strain Figure 6.8 shows the isolated distribution of  $\partial v/\partial y$  which was obtained by rotating the specimen and the camera by  $90^\circ$  about the optical axis and by applying equation (6.9) as described in the previous section. The fringe pattern thus obtained agrees well with the result of the finite element analysis of the strain in  $y$  direction, which is shown in figure 6.9.

Image doubling Due to the image shear, the object always appears doubled in the resulting images. This becomes particularly evident at the borders of the object and at discontinuities like the hole in our specimen. Quantitative fringe interpretation and location with respect to the object is therefore impeded by the finite shear distance (see Chapter 5, “Removing the Image Doubling” for analysis and a possible solution of this problem). However, the experimental results are encouraging and show that the measurement of in-plane strain with shearography is feasible.

**Figure 6.8** The phase fringe pattern showing the isolated distribution of  $\partial v/\partial y$ . It represents the strain in the specimen in  $y$  direction.



**Figure 6.9** The calculated distribution of the strain in  $y$  direction.



## 6.5 Concluding Remarks

The visualization of in-plane strain with shearography still imposed the problem of how to suppress the contribution from the out-of-plane displacement derivative  $\partial w/\partial x$  or  $\partial w/\partial y$ . We have briefly described the few solutions to this problem that were proposed in the literature, and we have pointed out their disadvantages. We have described an optical set-up with three light sources which allows to accurately isolate all six displacement derivatives quickly and easily and which does not possess the disadvantages of the methods that were described in the literature so far.

Experimental verification We have demonstrated the isolation procedure on a selected specimen. The results were validated by comparison with calculated strain

distributions. We have shown that it is possible to visualize in-plane strain with shearography and to achieve high quality fringes capable of revealing even localized strain concentrations such as appeared around the hole in our specimen.

The optical set-up we have proposed is simple, and the isolation procedure can easily be automated. Therefore we believe that our method is well suited for the application in an industrial environment and provides a step forward towards the quantitative measurement of in-plane strain with shearography.

Point source  
illumination

It has to be mentioned that the simple procedure presented herein is only accurate, if *plane waves* are used for illumination. For *point sources*, the angles of incidence are only symmetric for one line on the object. An accurate isolation of the displacement derivatives is still possible taking into account the sensitivity vector for each image point separately. This is a part of the *quantitative evaluation* that will be investigated in the following chapter.



## QUANTITATIVE EVALUATION

In the previous chapters, theoretical aspects and various image processing techniques were described, developed, or investigated. These techniques will now be adapted to reach the goal of this work, i.e. the quantitative measurement of strains with shearography. First, we discuss strategies to acquire the images that are necessary for the strain measurement. A method, which records images with two shear directions is compared with a method, which only needs one shear direction and reduces the number of images by a factor of two. In section 7.2, the evaluation procedure is presented, which extracts the components of strain from the acquired images. Section 7.3 then goes into the details of some steps of the evaluation.

### 7.1 Measurement Strategy

---

#### 7.1.1 Two Shear Directions

---

As explained in the previous chapter, approximations to the components of the displacement derivative  $\partial u/\partial x$ ,  $\partial v/\partial x$ ,  $\partial w/\partial x$ ,  $\partial u/\partial y$ ,  $\partial v/\partial y$ , and  $\partial w/\partial y$  can be isolated from the phase images measured with three illumination directions and two shear directions. To obtain the complete set of images needed for the evaluation, the measurement sequence shown in figure 7.1 can be applied.

Measurement  
sequence

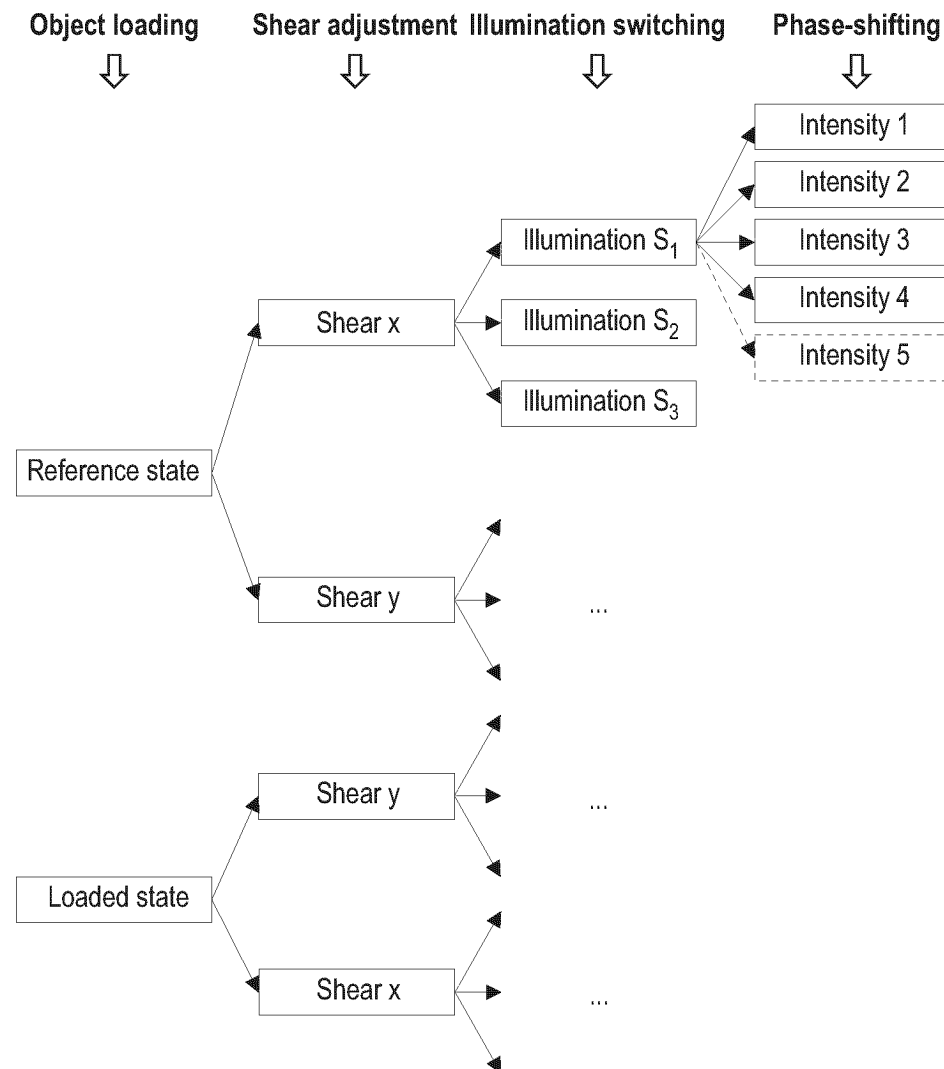
In the reference state, the shearography system is first set up with the shear  $\Delta x$  in  $x$  direction. Illumination source  $S_1$  is switched on and a series of phase-shifted images is recorded by controlling the device for temporal phase shifting in the shearography system. Then  $S_1$  is turned off and illumination source  $S_2$  is turned on for the recording of the next series of phase-shifted images. In the same way, images are recorded with illumination source  $S_3$  switched on. Now we adjust the image shearing device to a shear  $\Delta y$  in  $y$  direction. The same series of phase shifted images are now recorded by turning on and off the illumination sources  $S_1$ ,  $S_2$ , and  $S_3$  sequentially. Next, the object is loaded to induce the deformation to be measured. With shear in the  $y$  direction, another series of images with illumination from  $S_1$ ,  $S_2$ , and  $S_3$  and associated phase

shifts are recorded. Finally, the procedure is repeated after re-adjusting the shear in  $x$  direction.

**Number of images** The whole procedure requires the recording of 48 images if each phase image is calculated from four intensity images for the temporal phase-shifting (see section 3.1); with a five image algorithm, the number of images is increased to 60.

**Addition of incremental images** An improved quality of the measurement result is achieved and decorrelation can be avoided if the addition of incremental images [6] is applied. In this method, the load is introduced in small steps rather than in one single step. Phase images of subsequent load steps are subtracted (in order to obtain phase fringe patterns) and filtered. The filtered phase fringe patterns are then added modulo  $2\pi$ . Applying this method increases the number of images by 24 or 30 for each load step.

**Figure 7.1** Strategy of the measurement using two shear directions. The set of images needed for the quantitative evaluation comprises 48 or 60 images.



**Reduced recording sequence** The number of images that have to be recorded sequentially can be reduced in different ways. Obviously it is not possible to avoid the object

loading, but the three other levels indicated in figure 7.1 offer the potential for a considerable reduction.

**Phase shifting** At the level of phase-shifting, a temporal algorithm with 3+1 images (see section 3.1) would reduce the number of images to 24, with spatial phase shifting (section 3.2), the number of images amounts to 12. Both methods have the drawback of yielding a reduced image quality, which would impede the quantitative evaluation.

**Illumination switching** At the level of illumination switching an interesting solution was proposed in the European research project “Multi-Wavelength Shearography” (MuWaS) [85]. The illumination sources  $S_1$ ,  $S_2$ , and  $S_3$  illuminate the object simultaneously, but at three different wavelengths (810 nm, 830 nm, and 850 nm). In the shearography system, the light is divided after the shearing device and imaged onto three CCD cameras. In front of each camera, a narrow band filter is mounted to single out one of the three laser frequencies. The images of the three cameras can be acquired synchronously by using the red, green and blue channels of a standard colour frame-grabber. With this multi-wavelength method, the total number of images remains the same, as with the method described above, but the synchronous recording reduces the sequential acquisition steps by a factor of three. This improvement has to be paid with a rather complex optical set-up and with a considerable loss of light.

**Shear adjustment** In the same project MuWaS, a method based on polarization effects was proposed to avoid the shear adjustment during the measurement [86]. Circular polarizers are mounted in front of the illuminating lasers to provide an arbitrary polarization of the light reflected from the object. This reflected light enters a Michelson interferometer as shown in figure 2.11. The mirror for adjusting the image shear is replaced by a polarizing beamsplitter and two mirrors, where one mirror is adjusted to effect a shear in  $x$  direction and the other mirror in  $y$  direction. The camera is also replaced by a polarizing beamsplitter and two CCD cameras. In this way, the image with shear in  $x$  direction is captured with one camera and the image with shear in  $y$  direction with the other camera. Again the total number of images is not reduced, whereas the recording sequence is shortened by a factor of two.

In our laboratory, experiments were performed to measure the shearing strain  $\gamma_{xy} = \partial u / \partial y + \partial v / \partial x$  in one measurement by using polarized light illumination and observation with two shearography sensors [87].

The drawbacks of these solutions are the same as for the multi-wavelength set-up: they also complicate the optical set-up and reduce the light efficiency.

## 7.1.2 One Shear Direction

**Displacement fields** An alternative method of reducing the number of images is based on the technique described in Chapter 5, “Removing the Image Doubling”. With this technique, the displacement fields  $u$ ,  $v$ ,  $w$  can be determined from measurements with shear in  $x$  direction. From these displacement fields,

the displacement derivatives in both  $x$  and  $y$  direction can be numerically derived with high accuracy, even if the shear distance is rather large. From the measurements with shear in  $y$  direction the same displacement fields  $u$ ,  $v$ ,  $w$  can be determined. The measurements with shear in  $x$  direction do – in principle – not contain additional information and are therefore obsolete.

Half number of images This measurement strategy consequently needs only one shear direction and half the images of the one depicted in figure 7.1. This simplifies also the control of the system, because the shear does not have to be changed during the measurement.

From the above possibilities we decided to realize the method with *one shear direction*, *sequential illumination* of the object and *temporal phase shifting* with the *four image method*. This means that at each load step 12 images have to be recorded. This recording has to work in a sequential, but automated way.

### 7.1.3 Requirements for the Hardware

---

For a comfortable and automated implementation of the proposed measurement procedure, the shearography system has to incorporate the following features:

- The system has to be able to record and store a considerable number of images within reasonable time.
- The temporal phase shifting has to be controlled by the computer.
- The switching between the illumination sources  $S_1$ ,  $S_2$ , and  $S_3$  should also be computer controlled.
- The adjustment of direction and amount of shear does not have to be reproducible to such an accuracy that the images are correlated after repositioning. Still, a computer controlled adjustment of the shear distance and direction is desirable.

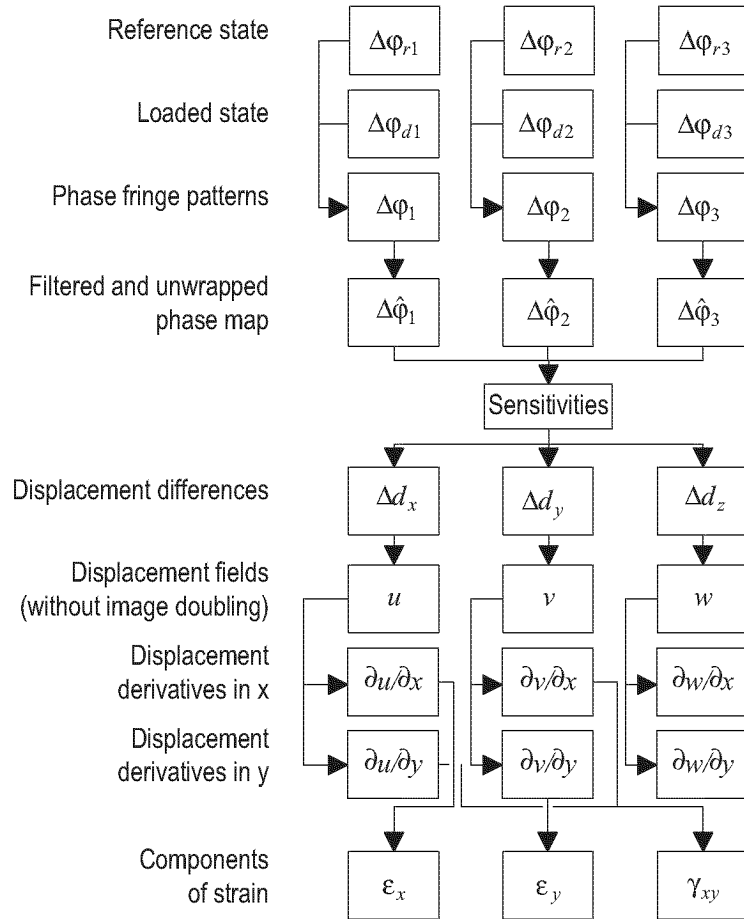
## 7.2 Evaluation Procedure

---

Overview How can we now process the recorded images in order to obtain the information on the mechanical deformation? The evaluation procedure is illustrated in figure 7.2.

6 phase images First we calculate phase images from the recorded intensities using temporal phase shifting, as explained in section 3.1 (this procedure is already implemented in the PISA software). In the following, we only consider these 6 phase images with the notation:  $\Delta\phi_{r,d}$ . The index  $r$  or  $d$  stands for the reference and deformed object state, respectively; 1, 2, and 3 indicate the illumination sources  $S_1$ ,  $S_2$ , and  $S_3$ .

**Figure 7.2** The measured images have to be processed in several steps in order to determine the components of strain.



**3 phase fringe patterns** The subtractions modulo  $2\pi$  of the phase images in reference and loaded state, recorded with the same illumination modules, yield the three phase fringe patterns

$$\begin{aligned}\Delta\phi_1 &= \Delta\phi_{d1} - \Delta\phi_{r1} \\ \Delta\phi_2 &= \Delta\phi_{d2} - \Delta\phi_{r2} \\ \Delta\phi_3 &= \Delta\phi_{d3} - \Delta\phi_{r3}\end{aligned}\tag{7.1}$$

**Filtering and unwrapping** These three patterns correspond to  $B_1$ ,  $B_2$ , and  $B_3$  in section 6.2 (figure 6.3, figure 6.4). For further processing, we filter the phase fringe patterns (see chapter 4) and transform them to phase maps by applying a phase unwrapping algorithm (see section 4.6). This yields the phase maps  $\Delta\hat{\phi}_1$ ,  $\Delta\hat{\phi}_2$ , and  $\Delta\hat{\phi}_3$ .

**Displacement differences** In Chapter 6, “Isolation of the Components” we have determined the displacement differences from the measured phase images by simply adding and subtracting the images. This was possible because we used plane wave illumination. Here, in the case of spherical wave illumination, we have to consider the variation of the sensitivity from pixel to pixel.

According to eq. (2.16) we obtain for every pixel a set of linear equations describing the relation between the measured phase change (filtered and unwrapped) and the deformation of the object:

$$\begin{aligned}\hat{\Delta\phi}_1 &= \mathbf{k}_1 \cdot \Delta\mathbf{d} \\ \hat{\Delta\phi}_2 &= \mathbf{k}_2 \cdot \Delta\mathbf{d} \\ \hat{\Delta\phi}_3 &= \mathbf{k}_3 \cdot \Delta\mathbf{d}\end{aligned}\quad (7.2)$$

$\mathbf{k}_1$ ,  $\mathbf{k}_2$ , and  $\mathbf{k}_3$  are the sensitivity vectors for the three illumination sources and  $\Delta\mathbf{d}$  is the displacement difference vector. The system of equations (7.2) can be expressed as a matrix equation

$$\begin{bmatrix} \hat{\Delta\phi}_1 \\ \hat{\Delta\phi}_2 \\ \hat{\Delta\phi}_3 \end{bmatrix} = \begin{bmatrix} k_{1x} & k_{1y} & k_{1z} \\ k_{2x} & k_{2y} & k_{2z} \\ k_{3x} & k_{3y} & k_{3z} \end{bmatrix} \cdot \begin{bmatrix} \Delta d_x \\ \Delta d_y \\ \Delta d_z \end{bmatrix}.\quad (7.3)$$

On the left side of eq. (7.3) we have the measured phase differences (which are filtered and unwrapped). On the right side, the *sensitivity matrix* is multiplied with the displacement difference vector, which is the mechanical magnitude we are interested in. For each image point we therefore have to determine the sensitivity matrix in order to calculate the displacement differences. The calculation of the sensitivity matrix is described separately in section 7.3.1. Eq. (7.3) can easily be solved for  $\Delta\mathbf{d}$  with MATLAB or a similar program.

Removing the  
image  
doubling

According to figure 7.2 the next evaluation step is the determination of the displacement fields  $u, v, w$  from the displacement differences  $\Delta d_x, \Delta d_y, \Delta d_z$ . This is achieved with the method to remove the image doubling described in chapter 5. With the notation used above, eq. (5.6) can be written as

$$\begin{aligned}\Delta\phi_{res}(\xi, \eta) &= \sum_{j=0}^n \Delta\phi(\xi - j\Delta\xi, \eta) = \sum_{j=0}^n \mathbf{k} \cdot \Delta\mathbf{d}(\xi - j\Delta\xi, \eta) \\ &= \mathbf{k} \cdot \mathbf{d}(x, y) = k_x \cdot u(x, y) + k_y \cdot v(x, y) + k_z \cdot w(x, y)\end{aligned}\quad (7.4)$$

where  $\Delta\xi$  is the shear distance in image coordinates. Since we have already eliminated the sensitivity  $\mathbf{k}$ , we do not perform the operation on the phase difference, but directly on the components of the displacement difference  $\Delta\mathbf{d}$ . By rewriting eq. (7.4) with the unit sensitivity vectors  $\mathbf{k} = [1, 0, 0]$ ,  $\mathbf{k} = [0, 1, 0]$ , and  $\mathbf{k} = [0, 0, 1]$ , we obtain

$$\begin{aligned}
\sum_{j=0}^n \Delta d_x(\xi - j \cdot \Delta\xi, \eta) &= u(x, y) \\
\sum_{j=0}^n \Delta d_y(\xi - j \cdot \Delta\xi, \eta) &= v(x, y) \\
\sum_{j=0}^n \Delta d_z(\xi - j \cdot \Delta\xi, \eta) &= w(x, y)
\end{aligned} \tag{7.5}$$

In section 5.3 we explained that a prerequisite for this method is that a part of the measured area is not deformed. This is the case if the object is clamped or if a reference plane is positioned at the image border. The method to remove the image doubling as described in chapter 5 assumes that the shear distance is an integer number of pixels. In section 7.3.2 we show how we can apply this method with higher accuracy.

Displacement derivatives	We can now numerically derive the displacements $u, v, w$ in $x$ and $y$ direction in order to determine the components of the displacement derivative $\partial u/\partial x, \partial v/\partial x, \partial w/\partial x, \partial u/\partial y, \partial v/\partial y,$ and $\partial w/\partial y$ . The derivative is calculated as the slope of the linear regression through 33 pixels.
Components of strain	Finally we can calculate the components of strain with the following relations:

$$\varepsilon_x = \frac{\partial u}{\partial x}, \varepsilon_y = \frac{\partial v}{\partial y}, \text{ and } \gamma_{xy} = \frac{\partial u}{\partial y} + \frac{\partial v}{\partial x}. \tag{7.6}$$

## 7.3 Details of the Evaluation

---

### 7.3.1 Sensitivity Matrix

---

The sensitivity matrix in eq. (7.3) consists of the components of the three sensitivity vectors  $\mathbf{k}_1, \mathbf{k}_2, \mathbf{k}_3$  in  $x, y,$  and  $z$  direction. Here, we want to show in detail, how the sensitivity vectors can be calculated for spherical wave illumination and imaging onto a small area. We introduce

$$\begin{aligned}
\mathbf{k}_1 &= \mathbf{k}_{s1} - \mathbf{k}_o \\
\mathbf{k}_2 &= \mathbf{k}_{s2} - \mathbf{k}_o, \\
\mathbf{k}_3 &= \mathbf{k}_{s3} - \mathbf{k}_o
\end{aligned} \tag{7.7}$$

where  $\mathbf{k}_o$  is the wave vector in observation direction and  $\mathbf{k}_{s1}, \mathbf{k}_{s2},$  and  $\mathbf{k}_{s3}$  are the wave vectors in the illumination directions (see section 2.1.3).

Knowing the co-ordinates of the points  $S_1, S_2,$  and  $S_3,$  and of the observation point  $O,$  we can calculate the sensitivity vectors for each object point  $P$  with

$$\mathbf{k}_{si} = \frac{2\pi}{\lambda} \cdot \frac{\vec{S_iP}}{|\vec{S_iP}|}, \quad \mathbf{k}_o = \frac{2\pi}{\lambda} \cdot \frac{\vec{PO}}{|\vec{PO}|}. \quad (7.8)$$

Location of Object Points

In equation (7.8) we need the co-ordinates of the point  $P$  for each pixel. In the image co-ordinates (see section 5.1) we define a reference point  $(\xi_0, \eta_0)$  as the point, on which the origin (center of the object) is imaged via the mirror that is not tilted. For any pixel in the image, the corresponding object co-ordinates are then given by

$$P = (P_x, P_y, P_z) = \left( \frac{\xi - \xi_0}{m_x}, \frac{\eta - \eta_0}{m_y}, 0 \right), \quad (7.9)$$

where  $m_x$  and  $m_y$  are the magnifications in  $x$  and  $y$  direction in pixel (in the image) per meter (on the object surface).

Variation between  $P$  and  $P_s$ ?

It was first intended to consider the variation of the illumination and observation angles between the point  $P$  and its sheared counterpart  $P_s$  (see section 2.1.3). Still, Prof. P. Jacquot showed [33] that this is not reasonable. Equation (2.16) can be written in the form

$$\Delta\phi = \mathbf{d}(P_s) \cdot \mathbf{k}(P_s) - \mathbf{d}(P) \cdot \mathbf{k}(P). \quad (7.10)$$

Since  $P$  and  $P_s$  lie close together, we can introduce the two small quantities  $\Delta\mathbf{d}$  and  $\Delta\mathbf{k}$ , where  $\Delta\mathbf{d}$  is the displacement difference as defined in eq. (2.18) and  $\Delta\mathbf{k}$  is sensitivity difference

$$\Delta\mathbf{k} = \mathbf{k}(P_s) - \mathbf{k}(P). \quad (7.11)$$

We obtain the phase difference

$$\begin{aligned} \Delta\phi &= (\mathbf{d}(P) + \Delta\mathbf{d}) \cdot (\mathbf{k}(P) + \Delta\mathbf{k}) - \mathbf{d}(P) \cdot \mathbf{k}(P) \\ &= \Delta\mathbf{d} \cdot \mathbf{k}(P) + \mathbf{d}(P) \cdot \Delta\mathbf{k} + \Delta\mathbf{d} \cdot \Delta\mathbf{k} \end{aligned} \quad (7.12)$$

The first term  $\Delta\mathbf{d} \cdot \mathbf{k}(P)$  is equivalent to eq. (2.20). Considering the variation of the sensitivity between  $P$  and  $P_s$  would mean to account for the last term  $\Delta\mathbf{d} \cdot \Delta\mathbf{k}$ , which is a second order term. The first order term  $\mathbf{d}(P) \cdot \Delta\mathbf{k}$  can not be calculated, since  $\mathbf{d}(P)$  is unknown at this evaluation step.

### 7.3.2 Exact Shear Distance

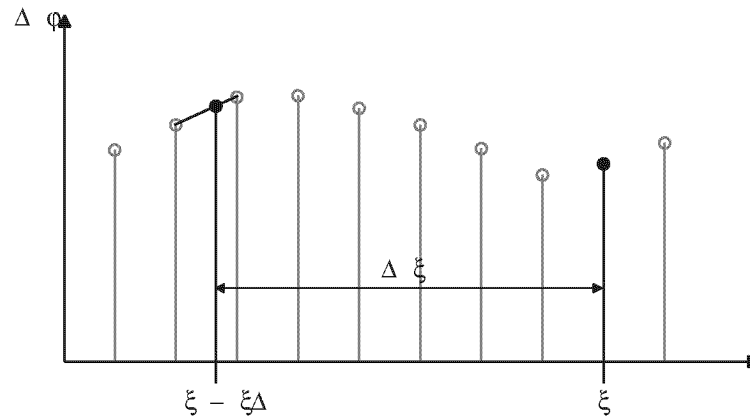
Non-integer shear distance

The method to remove the image doubling presented in chapter 5 assumes that the image shear  $\Delta\xi$  is an integer number of pixels. Since the shear usually amounts to 20 to 80 pixels, rounding it to the closest integer number may cause an error of several percent. Of course it is possible to adjust the shear before the measurement such that it equals an integer number of pixels. A more practical solution is to extend the method of chapter 5 to non-integer shear distances. This can be done by linear interpolation as shown in figure 7.3. Instead of adding the phase values at individual pixels – as illustrated in figure 5.3 – the two neighbouring



pixels are considered and the phase value is determined by linear interpolation between these pixels.

**Figure 7.3** Determination of the phase values for non-integer shear distances  $\Delta\xi$  by linear interpolation.



Variation of the shear distance

As derived in detail by Aebischer and Rechsteiner [88], the shear distance produced by the Michelson interferometer is not constant across the image. The error in the shear distance can be determined in good approximation by

$$\varepsilon \cong \frac{-2 \cdot x_p \cdot \Delta x}{4 \cdot (d_o + d_s)^2 - \Delta x \cdot (\Delta x + 2 \cdot x_p)}, \quad (7.13)$$

where  $\Delta x$  is the shear distance at the object centre,  $x_p$  is the co-ordinate on the object,  $d_o$  is the distance between object and centre of the beam splitter, and  $d_s$  is the distance between centre of the beamsplitter and mirror.

Effect in the experiments

To judge the importance of this effect in practice, eq. (7.13) was evaluated with the values of our measurements in chapter 9. With  $d_o = 560$  mm,  $d_s = 35$  mm,  $\Delta x = 5$  mm, and  $x_p = 68$  mm, we determined the error. This error amounts to 0.048 %. The effect of shear distortion is therefore negligible for our measurements and was not considered in the evaluation.

The whole measurement and evaluation procedure – from the acquisition of the necessary images to the determination of the strain components as illustrated in figure 7.2 – will be performed in Chapter 9, “Quantitative Strain Analysis”. But first in chapter 8 we will describe the hardware and software necessary for the measurements.



## DEVELOPMENT OF ADAPTED EQUIPMENT

This chapter presents and explains in detail the equipment we used for the experiments throughout this work. Section 8.1 describes the laboratory system, which is flexible but difficult to handle, and the device for loading tensile specimens. In section 8.2, the requirements for a practical 3D shearography system are compiled and the commercially available shearography systems are shortly introduced. The comparison of our requirements with what is available motivates our decision to develop our own shearography system. Section 8.3 then describes the developed system consisting of a shearography head, three illumination modules, electronic control and software.

### 8.1 Laboratory System

---

For the verification of the technique described in chapter 6, a shearography system has been developed in our laboratory. The set-up shown in figure 6.2 allows for a symmetric illumination in the  $x$ - $z$  plane. The optical arrangement and the object are placed on a vibration isolated table of  $2.4 \text{ m} \times 1.2 \text{ m}$  size.

#### 8.1.1 Optical Arrangement

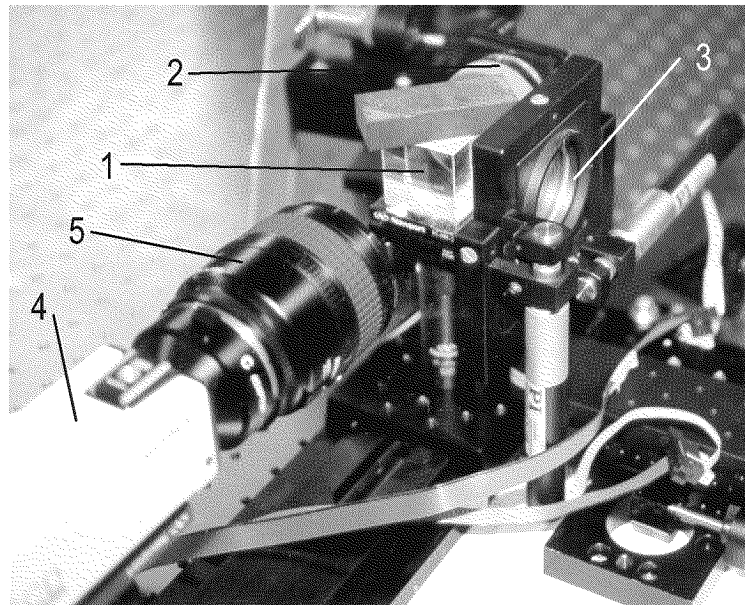
---

**Illumination** A helium-neon gas laser with a power of 35 mW at a wavelength of 632.8 nm (SPECTRA PHYSICS 127-35) is used as light source. The optical elements like beamsplitters, lenses, and mirrors are positioned using mounts and magnetic bases from NEWPORT and PHYSIK INSTRUMENTE. The “Removable mirror” in figure 6.2 is in fact a beamsplitter distributing the light for illuminating the object from the left and right side. By simply blocking one of the two beams, the illumination direction can be selected. The “Ray expansion” consists of two components: (1) A spatial filter (NEWPORT M-900), with a microscope objective and a pinhole aperture in the objectives focal point, produces a clean spherical wave. (2) A lens with diameter 70 mm and focal length 200 mm, positioned with one of its

focal points in the pinhole aperture, transforms the spherical wave to a plane wave.

**Observation** We decided to use a Michelson interferometer as shear element. It consists of a beamsplitter cube and two mirrors. The “Mirror with phase shifting element” is a mirror glued to a piezoceramic cylinder, which is connected to a voltage amplifier. This amplifier (LP PIEZOMECHANIK SQV 1/500) produces a voltage of 0 ... 500 V. The “Shear adjusting mirror” is fixed in a cardanic mirror mount and can be rotated about two axes by DC-MIKE motors (PHYSIK INSTRUMENTE M-220.20). These motors have integrated gear units to produce a linear translation and are connected to a special interface card (PHYSIK INSTRUMENTE C-832) in the PC.

**Figure 8.1** Observation part of the shearography arrangement consisting of (1) beamsplitter cube, (2) mirror with phase shifting element, (3) shear adjusting mirror, (4) CCD camera, and (5) camera lens.



The image of the object observed through the Michelson interferometer is captured by a black and white CCD camera (SONY AVC-D7CE). This camera with  $756 \times 581$  pixels produces an analogue signal according to the CCIR video standard. The camera incorporates a thread for a C-mount lens. However, we used NIKON lenses for photographic cameras with various focal lengths (24 mm, 35 mm, 60 mm, and 105 mm for photo format), which are mounted on the camera using a C-mount adapter.

### 8.1.2 Computer Hardware

For image acquisition and control of the system, a personal computer with an INTEL 80486/66 MHz processor and 32 MB RAM is used. Three interface cards are installed in the PC:

- The “Modular Frame Grabber” board (IMAGING TECHNOLOGY MFG-3M-V) digitizes the analogue video signal from the CCD camera in 8 bit depth. The card offers the possibility to connect a monitor for

displaying images, to intermediately store images, and to perform simple operations on images.

- In the digital to analog (D/A) converter board (DATA TRANSLATION DT 2815) only one of the eight D/A channels is used to produce a voltage of 0 ... 5 V. This signal serves as input for the high voltage amplifier driving the piezoelectric phase shifter.
- The motor controller card (PHYSIK INSTRUMENTE C-832) is used to control the two DC MIKE motors of the shear adjusting mirror.

A keyboard, mouse and two monitors complete the computer hardware. The PC is connected to the network for printing of the images and transfer of files to other computers.

### 8.1.3 Software

**OPTOCAT 5.02** The program OPTOCAT (Version 5.02, BREUCKMANN GMBH) controls the phase shift through the D/A card, the acquisition of images by the frame grabber board, and the processing and display of images. The program is running on the DOS operating system. However, we have installed OPTOCAT on a WINDOWS 3.11 system in order to be able to run other programs without quitting OPTOCAT. A total of about 180 functions are organized in 19 command groups (see figure 8.2). The functions operate on images of (in our case)  $512 \times 512$  pixels size and can be launched by mouse click, function keys, or from the command line. Additionally, a sequence of functions with their parameters can be stored in a batch job, which offers a simple way to automate measurement procedures.

**Figure 8.2** Main screen of the OPTOCAT program. In the upper left part, the command groups are shown, on the right side, special commands with their shortcuts are displayed and in the lower part the function keys. The last line on the screen is the command line. A second monitor is used to display the images.



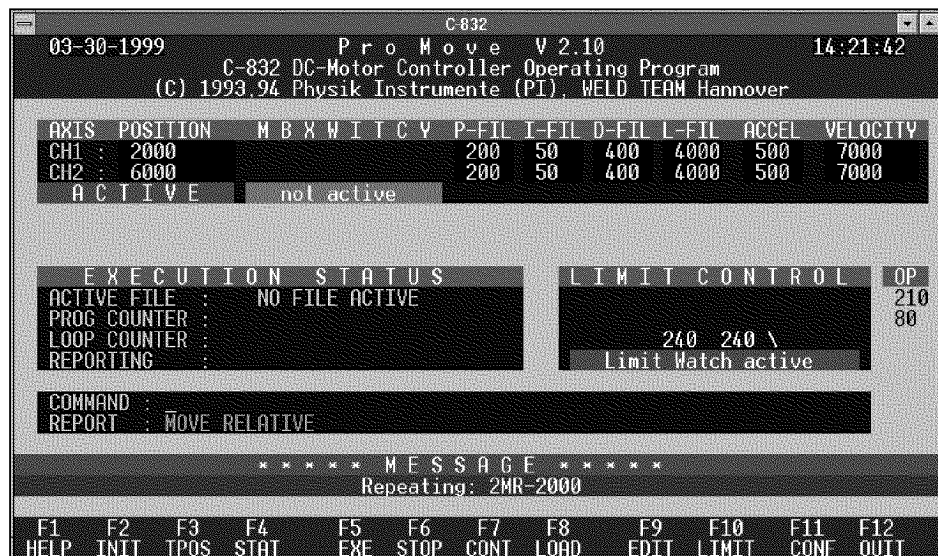
**Important functions** Here, we want to briefly introduce the OPTOCAT functions that are of importance for our measurements:

- FRINGES MOV-DEV, GAUGE-DEV serves for calibrating the phase shift. The voltage at the output of the D/A board causing a phase shift of  $2\pi$  can be determined and set as a constant.
- APE GRAB records phase-shifted intensity images and calculates the phase according to the temporal phase shifting technique (see section 3.1). A 3, 4, or 5 image algorithm can be chosen.
- APE SUB-PHI, ADD-PHI performs a subtraction or addition modulo  $2\pi$  (see section 3.5). With these functions, phase difference images can be calculated and the operations in eq. (6.7) can be performed.
- FRINGES FILT-PI serves for filtering phase fringe patterns. A sine-/cosine average filter as described in section 4.2 is used for this purpose. The first parameter is the filter size, which can be  $3 \times 3$ ,  $5 \times 5$ , or  $7 \times 7$ , the second parameter is the number of repetitions of the filtering. In contrast to our method (section 4.4), the phase is not recalculated between the filter steps.
- UTIL SAVE offers the formats BMP, TIFF, TARGA, OPTIMA, and DT-IRIS for saving the recorded and processed images.

OPTOCAT also offers functions for phase unwrapping and for 3D representation of the results, but these were not used in this work.

**PROMOVE 2.1** PROMOVE is a program that offers an interface to the C-832 motor controller card. It is delivered by PHYSIK INSTRUMENTE along with the card. The software is also based on the DOS operating system. It displays the current position and status of the motors and basically serves for changing this position. To do this in a controlled way, position limits, velocity and acceleration can be set. If a position encoder returns a signal to the card, a PID (proportional-integral-derivative) control can be designed to obtain the optimum positioning behaviour.

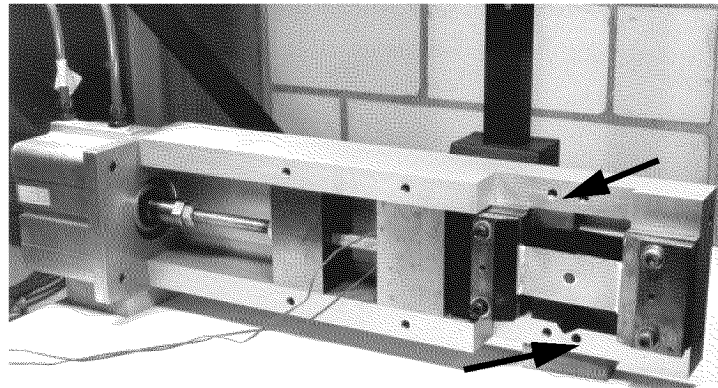
**Figure 8.3** The main screen of the ProMove program displaying the current status of the motors and the parameters for accessing the next position.



## 8.1.4 Object Loading Device

The object loading device used for the experiments shown in chapter 6 is designed to introduce a tensile force on a flat specimen of about 50 mm width, 200 mm length and up to 8 mm thickness. It was developed for the work documented in the theses of T. Flemming [83] and M. Hertwig [89].

**Figure 8.4** The pneumatic object loading device used for the tests. On the right side, the tensile specimen is clamped, on the left, the pneumatic cylinder applies a force, which is measured with strain gauges. The arrows point to the areas where the side walls of the U-shaped structure were removed.



**Pneumatic loading** The force is produced by means of a pneumatic cylinder. The pressure difference between the two sides of the cylinder is controlled by the voltage applied to a electro-pneumatic valve. At the loading device, a pair of strain gauges is glued on a load transferring bar with defined cross section, which serves for measuring the force applied to the sample.

**Superposed bending** The main structure of the loading device is made from an aluminium block with a U-shaped cross section. In order to be able to investigate not only the front side, but also the thin side of the sample with speckle interferometry, the side walls of the U were partly removed. Besides the wanted effect of optical accessibility, this intervention caused a weakening of the device. Applying a force to a stiff specimen now produces a bending of the loading device – and consequently of the specimen –, which is considerably larger than in the original state of the device.

## 8.1.5 Experience Gained with the Laboratory System

**Limited applicability** With this system it was possible to perform the experiments shown in chapter 6 to verify the isolation of the components. The optical set-up is very flexible and the software could be used as it was, without additional programming. Still, the system suffers from several drawbacks:

- The system is mounted on a large optical table and is therefore far from being portable.
- Only two illumination directions were realized. Four components of the displacement derivative can be isolated with this set-up. In order to measure all six components as described in section 6.2, the object has to be rotated.

- Plane wave illumination limits the illuminated area to the lens diameter (in our case 70 mm). In order to illuminate larger objects with plane waves, large optical elements would be necessary.
- $512 \times 512$  pixels are used by OPTOCAT. This is only 60% of the camera resolution.
- The pneumatic loading device produces not only tensile forces on the test sample, but also effects a considerable bending.

## 8.2 Why to Design our own Shearography System

---

In order to overcome the limitations mentioned above, an improved system is necessary. We compared our requirements with the systems available on the market and came to the conclusion that we have to develop our own shearography system.

### 8.2.1 Requirements for the Shearography System

---

Before starting to design the measurement system, we compiled a list of the requirements that have to be fulfilled. During the design process, some requirements were omitted, as they would have led to a considerably more complex design without an adequate benefit. Finally, we formulated the following requirements:

- All six measurements have to be performed without changing the optical set-up by hand or reorienting the object.
- The measurement results have to be phase fringe patterns. It is therefore necessary to apply a phase shifting technique.
- The amount of shear should be variable in order to adapt it to the measurement requirements. The method described in chapter 6 requires that also the direction of shear can be chosen.
- To adapt the system to various measurement conditions, it has to allow for easily exchanging the imaging lens and camera.
- The whole set-up should be portable and it has to work without lengthy adjustments.
- The system should also be suitable for simple out-of-plane applications with only one illumination direction.
- Visible laser light has to be used for reasons of safety, simple handling, and demonstration.
- It has to be possible to illuminate an area of up to  $30 \text{ cm} \times 30 \text{ cm}$ .

### 8.2.2 Shearography Systems on the Market

---

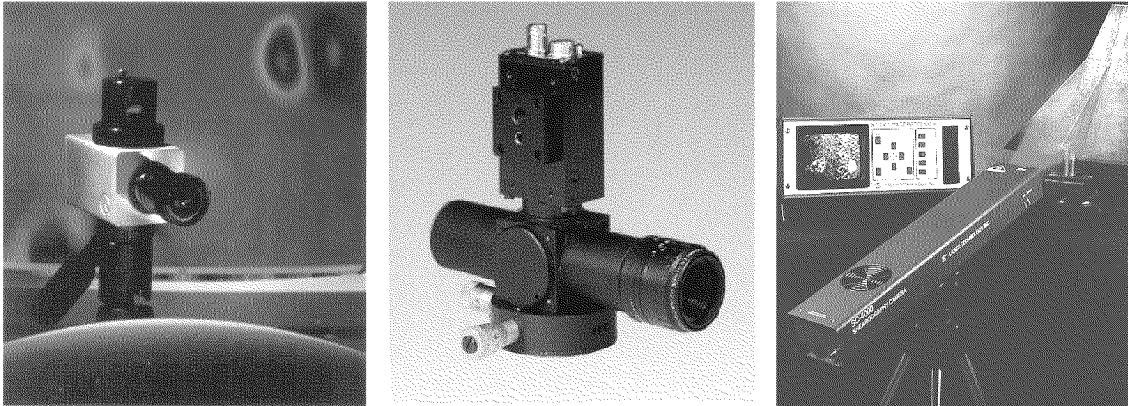
Figure 8.5 shows three commercially available shearography systems.

ETTEMEYER The shearography sensor developed by DR. ETTEMEYER GMBH & CO. (left image) incorporates both illumination and observation part. In the



lower part of the arrangement, a Michelson interferometer and a camera chip are integrated. The phase shift is effected by moving one of the mirrors with a piezo-electric device. The shear can be adjusted by turning two screws on the sensor. From the upper part, the light of an infrared laser diode is distributed onto the object surface. A video zoom-lens completes the arrangement. The highly integrated and compact sensor can be mounted on a standard tripod.

**Figure 8.5** Commercially available shearography systems from DR. ETTEMEYER GMBH & CO. (Neu-Ulm, Germany, left image) [27], STEINBICHLER OPTOTECHNIK GMBH (Neubeuern, Germany, middle image) [90], and LTI (LASER TECHNOLOGY, INC., Norristown (PA), USA, right image) [91].



**STEINBICHLER** The middle image shows the shearography sensor of STEINBICHLER OPTOTECHNIK GMBH. Here, only the observation part is integrated, the illumination can be chosen deliberately. This system is also based on an Michelson interferometer, with one mirror attached to a piezo for the phase shift and one mirror tiltable with two micrometer screws for adjusting the image-shear. The lens and the CCD camera are connected to the beamsplitter block. Obviously, the arrangement is also integrated and compact.

**LTI** One of the shearography systems from LASER TECHNOLOGY, INC. is shown in the right image of figure 8.5. In this device, the illumination and the observation are integrated in one – rather large – housing. LTI also produces systems consisting of a shearography sensor and a vacuum hood. The vacuum hood serves for attaching the device to the object and for applying the load.

**Summary** ETTEMEYER and LTI both integrated the illumination in the system, which restricts the application to the out-of-plane case. For our purposes, the STEINBICHLER system (and also the other systems) could be complemented with a special 3D illumination system. The image shear in the ETTEMEYER and STEINBICHLER system has to be adjusted by hand; for the LTI system, we do not know how the shear is realized. A motor controlled adjustment of the shear and a compact design for a 3D shearography system meeting our requirements can not be purchased on the market. Since product design is one of the main interests of our institute, we decided to develop and realize our own optimized shearography system.

## 8.3 Realization of the Shearography System

---

Based on the requirements defined in section 8.2.1, we made basic considerations and comparisons of different configurations. The optimum concept was then designed in detail and realized.

### 8.3.1 Concept

---

- Illumination directions** For the illumination, we decided to adopt the arrangement proposed in chapter 6. The object is sequentially illuminated from three directions with the illumination vectors  $k_i$ , arranged in a particular symmetry, as shown in figure 6.1. If plane waves are used for illumination, this allows for isolating the components of the displacement derivative by simply adding and subtracting the phase fringe patterns. In our realization, it is not intended to use plane wave illumination for larger objects, as this would necessitate large lenses or parabolic mirrors. On the other hand, with spherical waves the evaluation gets more complicated: the sensitivity vector varies from pixel to pixel, which has to be taken into account for accurate evaluation.
- Shear directions** In order to record all the necessary images with loading of the object only once, the measurement procedure described in section 7.1 has to be applied. This measurement procedure would necessitate that the mirror could be repositioned very accurately, such that correlation between the first and the last three phase images is obtained. If this is not possible, the object has to be loaded twice to perform all measurements.
- Three lasers** The three illumination directions could be realized with one laser source and a system of mirrors and beamsplitters or optical fibers. Alternatively, three independent laser sources could be used. (Note that no coherence between the illumination directions is necessary.) We decided to realize the latter solution as it simplifies the design considerably. Shutters in the illumination path facilitate the sequential illumination. For pure out-of-plane measurements, only one illumination module is necessary. This module should be fixed directly to the measurement head to effect an illumination almost perpendicular to the object surface. The necessary laser power depends on the area to be illuminated, on the light absorption of the surface, and on the optical system. Based on our experience, 50 mW laser power is sufficient to illuminate an area of  $30\text{ cm} \times 30\text{ cm}$  for shearography measurements.
- Michelson set-up** On the observation side, it was decided to implement a Michelson interferometer set-up to accomplish the image shearing and the temporal phase shifting method. The phase shifting is realized by translating one of the mirrors in the interferometer by a piezoelectric device. The other mirror can be rotated about two axes in order to adjust the amount and direction of shear. As this adjustment has to work automatically, the rotations have to be controlled by motors. The necessary rotation angle was calculated to be less than  $\pm 4^\circ$ . According to the measurement procedure described in section 7.1, the adjustment of the shear has to be

reproducible such that correlation between the first series and the last series of measurements is obtained.

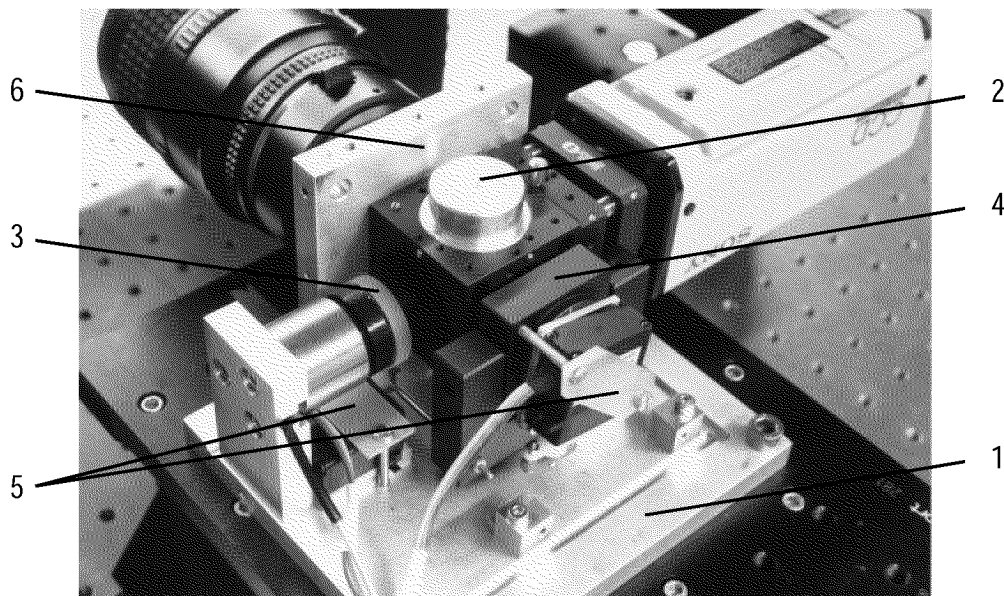
**Interfaces** The interface between the interferometer head and the camera and imaging lens is realized with C-mount threads, which is an accepted standard. In contrast to the set-up in figure 6.2, the lens is located between interferometer and object. As the image plane of the camera is too far away from the lens, an additional lens has to be introduced in order to shift the image plane to the cameras CCD chip. For communication between the computer and the measurement system, a D/A card is used that offers eight analog output channels which can be accurately regulated between 0 V and 5 V.

Having performed these basic considerations, the system was designed in detail.

### 8.3.2 Design of a Compact Shearography Head

**Interferometer set-up** An inside view of the realized shearography head is shown in figure 8.6. The mechanical and optical elements are mounted on base plate 1 with a size of 130 mm × 112 mm, which also serves for fixing the whole system. Holes compatible with the metric standard for optical elements (25 mm spacing) as well as a thread for interface with a photo/video tripod are integrated. Elements 2, 3, and 4 form the Michelson interferometer. The beamsplitter plate is fixed to element 2. Mirror 3 is mounted on a piezoelectric element to effect the phase shift. The mount of mirror 4 allows for rotation about two axes. Part of the elements are from SPINDLER & HOYER and PHYSIK INSTRUMENTE, the rest was designed and fabricated at ETH.

**Figure 8.6** Inside view of the shearography head with 1) base plate, 2) beam splitter holder, 3) mirror for phase-shifting, 4) mirror for shear adjustment, 5) servomotors, and 6) front plate.



- Shear control** A complex task is the control of the shear angle and direction by motors, as the requirements in terms of accuracy, range, and compactness are highly demanding. After considering different alternatives, we decided to use servomotors that are well known from radio-controlled modeling. A servomotor is a combination of a motor and a gear unit. The selected model GRAUPNER C-341 provides a rotation range of about  $\pm 40^\circ$ . The position is internally controlled by a potentiometer connected to the output shaft. As we need a much smaller rotation angle, a crank system is inserted between the servomotor and the mirror.
- Interfaces** The front plate 6 holds three tubes made from carbon fiber reinforced plastic on which the illumination modules are mounted. C-mount connectors allow for the combination with virtually any CCD camera and lens. This shearography arrangement is covered with a housing that offers the possibility to fix one illumination module directly on top of the head for the 1D out-of-plane measurement. The assembly is designed to be compact and stable, but offering the possibility to accurately adjust the optical elements.

### 8.3.3 Design of Illumination Modules

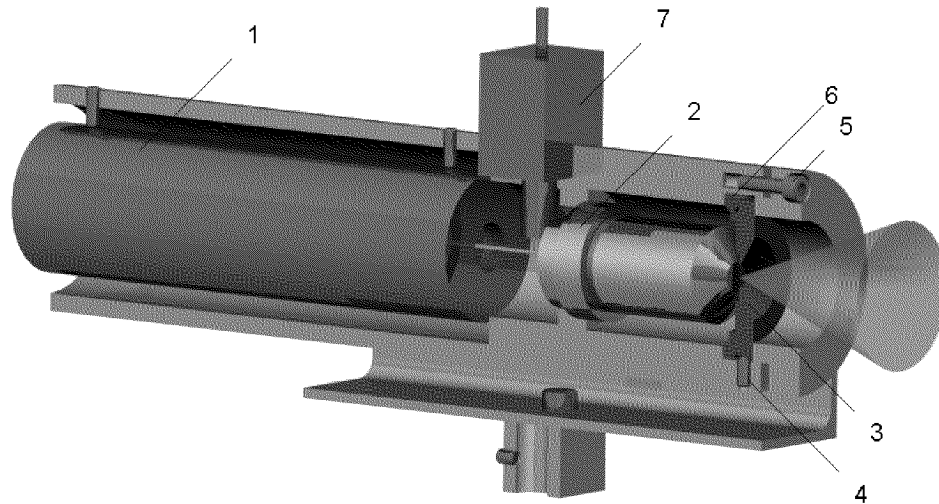
- Laser evaluation** The shape and size of the illumination modules is mainly defined by the laser. Its evaluation had therefore to be completed before designing the rest of the module. The laser has to offer 50 mW power of visible light, it has to be compact, reasonably priced, and its beam quality has to meet the requirements of interferometric measurements. It is worth noting that the required coherence length is much smaller in shearography than in ESPI, because the path difference between the interfering waves is only a few millimeters.

A thorough comparison finally showed that a Nd:YVO<sub>4</sub> diode pumped solid state laser with a diameter of 30 mm and a length of 106 mm is best suited for our application. The wavelength of the emitted light is 532 nm (green) and the maximum power is 50 mW. The coherence length was not specified by the manufacturer, it was measured to be more than 800 mm. The Chinese company CASIX manufactures this laser (DPGL-1050) and GSÄNGER OPTOELEKTRONIK GMBH distributes it in Europe. The laser is driven by the GSÄNGER LDP-1000 laser diode power supply, which allows for varying the light power.

- Illumination set-up** The illumination module in figure 8.7 consists of the laser 1, whose beam is expanded by the microscope objective 2 and filtered with the pinhole aperture 3. Its hole is adjusted to the focal spot of the objective by moving it in radial and axial direction. The three headless screws 4 – positioned in 120°-steps in circumferential direction – set the radial position. The axial adjustment of the pinhole is possible by tightening the screw plugs 5, which compresses the elastic O-ring 6. The illumination beam can be interrupted by the shutter 7 consisting of an electric magnet.
- Housing** All these elements are integrated in a cylindrical housing, which is suspended in a U-shaped profile. The inclination of the cylindrical

module relative to the profile can be easily adjusted (see figure 8.10). The rotation axis lies in the focal plane of the microscope objective, so the source point of the spherical wave front does not move.

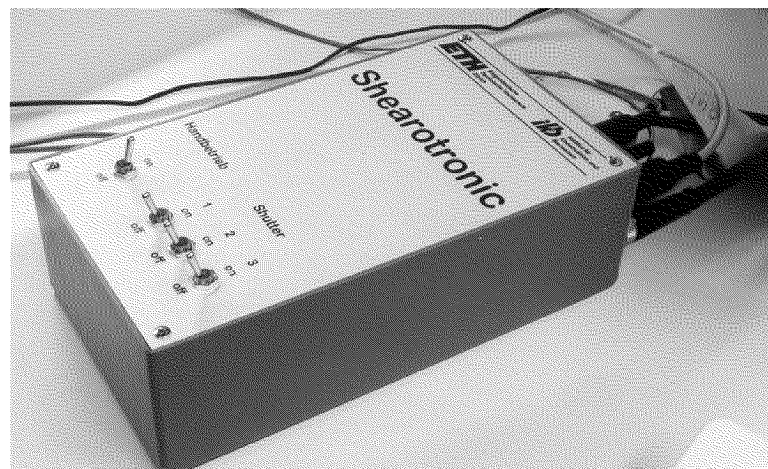
**Figure 8.7** Cut through the CAD model of an illumination module consisting of 1) Nd:YVO<sub>4</sub> laser, 2) microscope objective, 3) pinhole aperture with screws for radial (4) and axial (5) adjustment, 6) elastic O-ring, and 7) electromagnetic shutter [31].



### 8.3.4 Electronic Control

For automatic control of the system, we have developed special driver electronics. A drawing of the circuit is shown in figure 8.9. From the eight channels of the D/A card DT2815 we used seven.

**Figure 8.8** Electronic box for the interface between the PC and the shearography system.



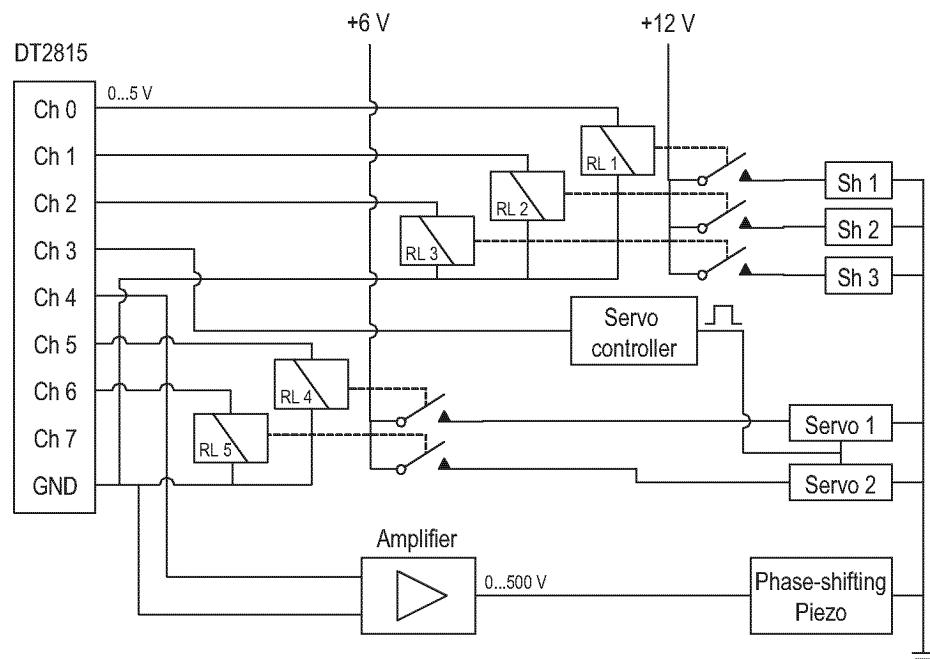
Shutter control Channels 0, 1, and 2 are used to switch the shutters of the illumination modules. As the electromagnetic shutters need a voltage of 12 V, the switching is effected by means of the three relays RL 1, RL 2, RL 3. These relays can be bridged for manually controlling the shutters.

**Servo control** Three channels are necessary to control the two servomotors that serve for adjusting the image-shear. Channels 5 and 6 are switching the power supply of the motors (+6 V) on and off through the relays RL 4 and RL 5. Channel 3 is the input to the servo controller electronics (CONRAD ELECTRONIC 234915-62), which transforms the DC voltage to the pulse-width modulated signal that is necessary to control the servo's rotation angle. This signal is acting on both servos but has only an effect, if the corresponding power supply is switched on.

**Piezo control** Finally, channel 4 is connected to an amplifier for driving the piezo-electric element, which needs a voltage of up to 500 V.

The servo controller, the relays, and the switches to manually control the shutters are integrated in one compact box with all the necessary connectors, which is shown in figure 8.8.

**Figure 8.9** Electronic circuit for the control of the shearography head. Ch 0 to Ch 7 are the output channels of the D/A card, Sh 1 to Sh 3 are the three shutters in the illumination modules and Servo 1 and Servo 2 the servomotors to rotate the shear-adjusting mirror.



### 8.3.5 Measurement Arrangements

**1D and 3D arrangement** Figure 8.10 and figure 8.11 show the arrangements for 1D and 3D measurements, respectively. The shearography head with one illumination module mounted directly on top of it (figure 8.10) is best suited for out-of-plane measurements. The illumination direction is almost perpendicular to the object surface, so the component  $k_z$  of the sensitivity vector  $k$  is dominant in equation (2.17). In order to measure the 3D deformation, the arrangement of figure 8.11 is used. All three illumination modules are mounted at the end of tubes made from carbon fiber reinforced plastic.

**Figure 8.10** Arrangement for out-of-plane measurements. The shearography head is combined with one laser module.



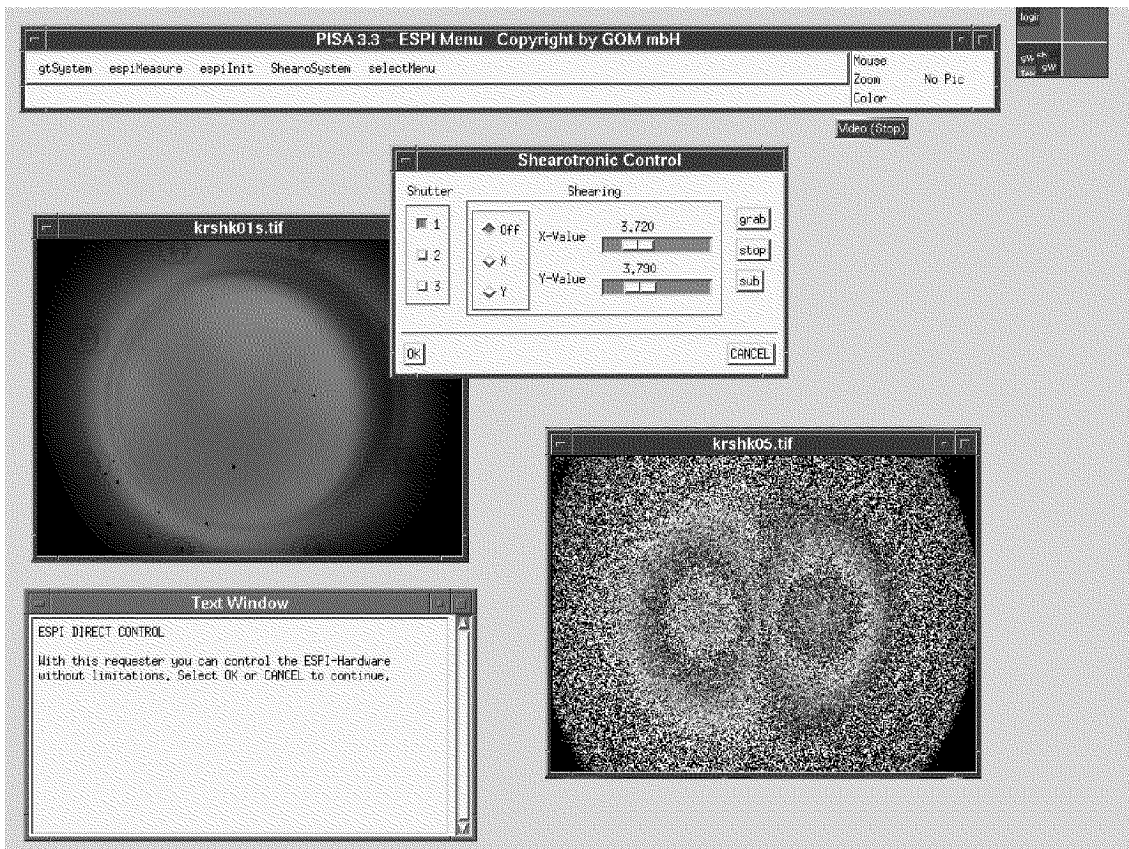
**Figure 8.11** For 3D measurements, the shearography head is combined with all three illumination modules.



### 8.3.6 Hardware and Software

PENTIUM PC In comparison with the laboratory system described in section 8.1, more recent equipment is used. The PC's processor is an INTEL PENTIUM 90 MHz. The RAPTOR PCI 15/1 card from BITFLOW INC. serves as a framegrabber and – like in the laboratory system – the DATA TRANSLATION DT 2815 board as a digital to analogue converter.

**Figure 8.12** Screenshot of the PISA program. The commands are arranged in pull-down menus and the images are represented in individual windows.



PISA 3.3 The software PISA (Version 3.3, GESELLSCHAFT FÜR OPTISCHE MESSTECHNIK MBH), which runs on the operating system LINUX, performs the acquisition and processing of the images. PISA offers basically the same functionality as OPTOCAT 5.02 (see section 8.1.3). We therefore restrict ourselves to pointing out the main differences between the two programs.

- PISA is a mouse- and window-oriented program. Commands are organized in pull-down menus and the images appear in individual windows as one is used to from office and graphics software (see figure 8.12).
- An additional screen for displaying images is not necessary.
- The number and size of images is not as restricted as in OPTOCAT. With our configuration, the image size is  $768 \times 572$  pixels.



- In OPTOCAT, the data is always stored in 8 bit per pixel, which corresponds to 256 grey levels (or colours). In PISA, it is possible to use 16 bit per pixel. This is essential for the phase unwrapping, because representing the unwrapped phase in 8 bit means reducing its resolution. In the example of figure 4.6 the unwrapped phase expands over more than four periods. Since the wrapped phase is represented in 256 grey levels, the unwrapped phase would cover a range of more than 1024 grey levels.
- The PISA software is open for the seamless integration of additional functions. These functions can be programmed in C using the libraries that are delivered with PISA and then linked with the fundamental version. In figure 8.12, the menu “ShearoSystem” appears, which contains the functions that we developed to control the shearography system.

Please note that the above comparison refers to the versions that are available at our laboratory. More recent versions of OPTOCAT offer similar features as the PISA software.

## 8.4 Self Developed Software Routines

---

For the image processing described in chapter 4 to chapter 7, the functions contained in OPTOCAT and PISA are not sufficient. We had to develop the respective software routines ourselves. The only exception is the “Isolation of the Components” in chapter 6: With plane wave illumination, the addition and subtraction of the images modulo  $2\pi$ , which is included in both programmes, is sufficient.

### 8.4.1 PISA vs. MATLAB

---

PISA	As mentioned above, additional functions in C language can be integrated in PISA. Most of the PISA commands are accessible to the programmer in form of library functions. Additional libraries to easily realize user interfaces are also available. After successful compilation and linking, the programmed functions appear integrated in the pull-down menus of PISA.
MATLAB	A different platform for developing image processing software is MATLAB. MATLAB stands for <i>matrix laboratory</i> and integrates numerical analysis, matrix computation, signal processing, and graphics. Since bitmap images can be considered as matrices, MATLAB is a powerful tool for image processing, too.
Advantages and drawbacks	The advantages of software development using MATLAB are that very high level commands – e.g. two-dimensional FFT, reading a BMP image from disk, vector multiplication, and solving systems of linear equations – are already integrated. Additionally, efficient tools for visualisation like shaded 3D representations are available.

MATLAB is an interpreted language, so it is not necessary to recompile and link the program after editing the code. On the other hand, an

interpreted language is slower than compiled code. A further drawback of MATLAB is that the developed software is not “stand-alone”, it only runs on computers where MATLAB is installed.

MATLAB is therefore the ideal platform to develop and test new algorithms. To integrate an optimized algorithm in an environment for recording and processing images, PISA is a good choice.

## 8.4.2 Implementation

---

- |                             |   |
|-----------------------------|---|
| Filtering                   | The software for filtering phase fringe patterns (chapter 4) was developed with MATLAB. In fact we have programmed different filters such as anisotropic Gaussian filters and adaptive filters before we discovered the advantageous behaviour of the multiply repeated anisotropic sine/cosine average filter. This filter was then programmed in C and integrated in PISA.  |
| Image doubling              | The method to remove the image-doubling (chapter 5) was directly programmed in C/PISA. We have developed two functions, one working with 8 bit phase images and one for 16 bit phase images.  |
| Isolation of the components | If the object is illuminated with plane waves, the isolation of the components (see chapter 6) can be achieved by simply adding or subtracting the phase fringe patterns modulo $2\pi$ . This can be effected with the built-in functions of OPTOCAT and PISA. For the experiments documented in chapter 9, spherical wave illumination was used. The sensitivity vector then varies from pixel to pixel, which has to be taken into account for the isolation. This evaluation procedure was programmed in MATLAB. |
| Quantitative evaluation     | The automated <i>recording</i> of the measurement sequence described in section 7.1 was programmed in PISA, whereas the <i>evaluation</i> of the images (section 7.2) was accomplished with MATLAB.   |

In the next chapter, the developed equipment and image processing software will be verified and applied to quantitative strain analysis.

# QUANTITATIVE STRAIN ANALYSIS

In this chapter, the developed measurement equipment, the image processing, and evaluation method are validated with measurements. In a first part of the chapter, the measurements with the laboratory system are briefly reviewed and the ability of the compact shearography system to provide quantitative results is tested on a simple out-of-plane example. In the second part, the quantitative strain analysis is performed with the shearography system. The test sample and the measurement conditions are described. Then, the strain distributions are calculated by finite element analysis for comparison with the measurement. The measured images are processed and quantitatively evaluated, which results in the strain distributions. Finally, the calculated and measured results are compared and discussed.

## 9.1 Preliminary Experiments

---

### 9.1.1 Experiments with the Laboratory System

---

The laboratory system described in section 8.1 was used to develop and demonstrate the isolation of components (chapter 6). The results of these measurements are documented in section 6.4. Figure 6.5 and figure 6.8 show the approximations to the components of strain  $\epsilon_x$  and  $\epsilon_y$ , respectively. The results are qualitatively good, but are not evaluated quantitatively. The quantitative evaluation will be performed on images measured with the compact shearography system later in this chapter (see section 9.2.3).

### 9.1.2 First Verification of the Shearography System

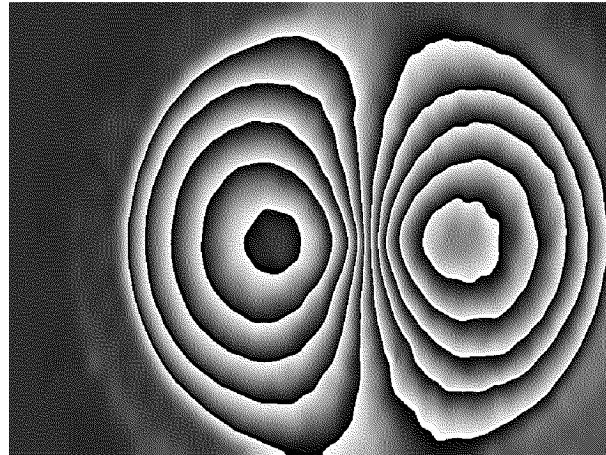
---

1D  
measurement

This first test should validate the ability of the compact shearography system (described in section 8.3) to provide quantitative results. As a test example, the well-known clamped circular plate was chosen. The plate is made from steel and has a 140 mm diameter and 1.5 mm thickness. It is

clamped all around the edge and loaded at the center of its back side by a micrometer screw. The 1D arrangement as shown in figure 8.10 was used for this measurement. The shear distance  $\Delta x$  on the object surface was chosen to be 5 mm. The shearographic measurement was performed using the addition of incremental images: The load – a displacement of  $13 \mu\text{m}$  – was applied in three steps, and the phase fringe patterns were filtered individually and added modulo  $2\pi$  as described in [6]. The fringe pattern in figure 9.1 shows the expected result. A measurement with shear in  $\Delta y$  direction accordingly led to a fringe pattern rotated by  $90^\circ$ .

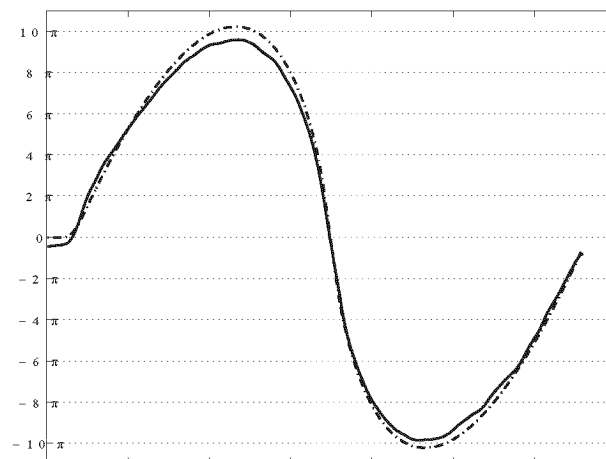
**Figure 9.1** Measurement of the out-of-plane deformation of a clamped circular plate loaded at its center.



Comparison  
with  
calculation

For comparison with a simulation, the fringe pattern of figure 9.1 was unwrapped and the phase was evaluated along a horizontal line through the center of the plate (solid line in figure 9.2). Based on plate theory (see eq. (5.8)), we calculated the out-of-plane displacement of the loaded plate and the corresponding shearography result (dash-dotted line in figure 9.2). In this simulation the shear distance, the laser wavelength, and the variation of the sensitivity vector were taken into account.

**Figure 9.2** Horizontal cut through the center of the plate (unwrapped phase). Measured result (solid line) and simulated result (dash-dotted line).



Comparing the measured with the simulated result, a good agreement is obtained. The measured deformation is slightly smaller, which could be

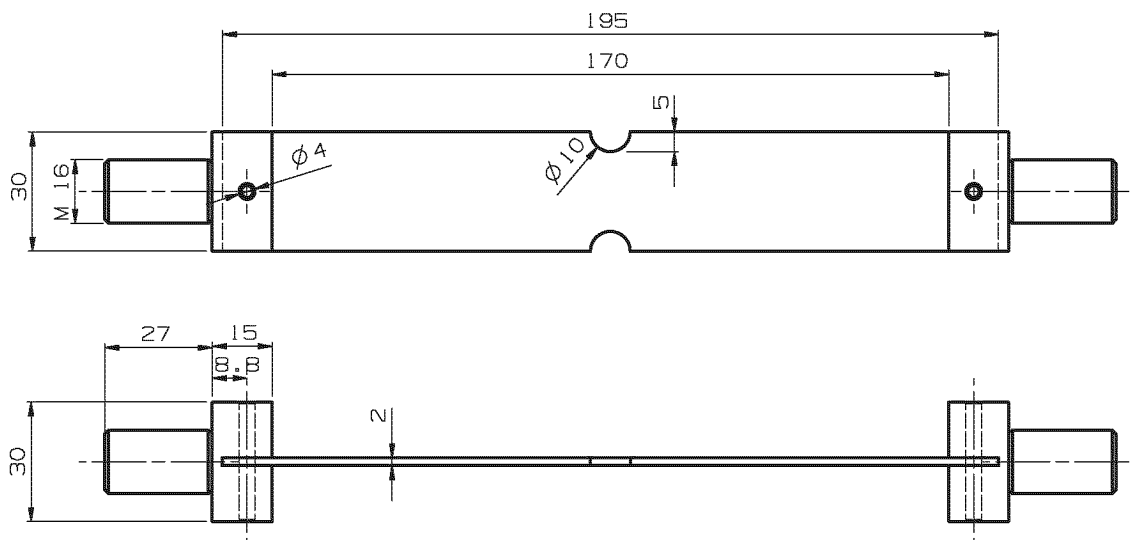
caused by the elasticity of the loading device itself. The maximum difference between the two curves is  $0.775 \pi$ , which is 7.6 % of the peak value.

## 9.2 Strain Measurement with the Shearography System

### 9.2.1 Description of the Measurement

**Test sample** As a test sample, a notched tensile specimen was selected. Geometry and material were chosen such that the sample exposes a clearly defined strain distribution. We chose steel as material, which shows an isotropic, linear elastic behaviour for the considered strain levels. The sample with 30 mm width and 2 mm thickness was made from tool steel 90MnCrV8.

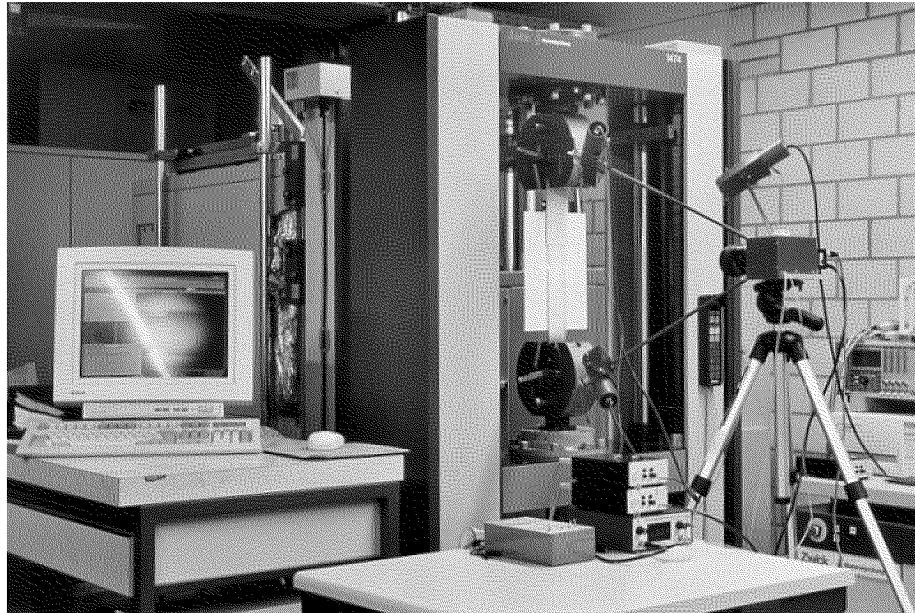
**Figure 9.3** Drawing of the notched tensile specimen that served as a test sample (with the interface parts).



Special attention was given to the interface between the testing machine and the test sample. In fact, a first test with a sample clamped directly in the testing machine (see figure 9.4) showed that – in addition to the tensile force – bending and torsion moments are induced in the specimen, resulting in a completely asymmetric strain distribution. Therefore, the design shown in figure 9.3 was chosen. Two interface parts (made from St 50-2) with M 16 threads hold the sample with bolts. The threads fit with specimen holders, which have two joints. These assure that no bending moments are transferred from the specimen grips to the specimen.

**Shearography set-up** In order to perform the measurement at the testing machine, the shearography head with the three illumination modules was mounted on a tripod, as shown in figure 9.4. Of course, also the PC and the electronic equipment had to be brought to the testing machine.

**Figure 9.4** The shearography system is mounted on a tripod and set up in front of the testing machine.



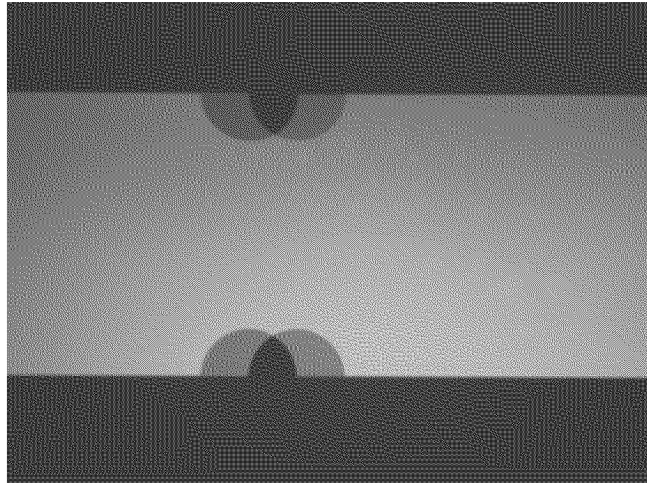
In order to optimize the quality of the fringe patterns, we changed the set-up in the following way:

- The pinhole apertures in the illumination modules were removed, which increased the light intensity on the object and enlarged the illuminated area. On the other hand, beam imperfections are no longer filtered out, which results in local intensity variations.
- It seemed that the lens system (camera lens and additional lens to shift the image plane) delivered poor quality images. We therefore removed the additional lens, mounted the camera lens with the C-mount adapter directly on the camera, and placed the camera next to the interferometer (like in figure 2.11). This arrangement is difficult to mount on a tripod, so a shelf was used as a basis.

These two measures lead to a considerably improved fringe quality.

**Image size** For the measurement shown below, the distance between object and shearography head (front edge) was 510 mm. A 60 mm NIKON lens was used and the camera was rotated by 90°, such that the larger number of pixels of the CCD is oriented in direction of the length of the object. With this set-up, the image corresponds to 68 mm × 51 mm of the object. The shear distance was adjusted to 5 mm in direction of the length of the test object. An image with white light illumination is shown in figure 9.5.

**Figure 9.5** Image of the test sample in the testing machine with white light illumination.



**Object loading** For the measurements in chapter 6, we used a pneumatic object loading device (see section 8.1.4). This has the advantage that it can be placed on the same vibration isolated table as the measurement head. The main drawback of the device is that it produces an unwanted bending of the object.

For the measurements with the compact shearography head, we decided to use the static testing machine ZWICK 1474. This machine is commonly used to perform standard tests to determine material properties (elastic modulus, tensile strength, etc.). Our motivation to use the testing machine for object loading was twofold: The loading of the object is expected to be well controllable, such that the measured deformation can be compared with calculations. Furthermore, applying the shearography system outside the optical laboratory demonstrates the flexibility and robustness of the developed system.

**Loads** The force that the testing machine effects on the object is controlled by a PC software and measured with a load cell. Before starting the measurement, a tensile force of 500 N was applied to the sample, in order to minimize sliding between the sample and the specimen grips and in the specimen grips itself. The load was then increased up to 2480 N. At four intermediate levels the measurement was stopped and images were recorded in order to allow for an addition of incremental images, which considerably reduces decorrelation.

## 9.2.2 Calculated Results

---

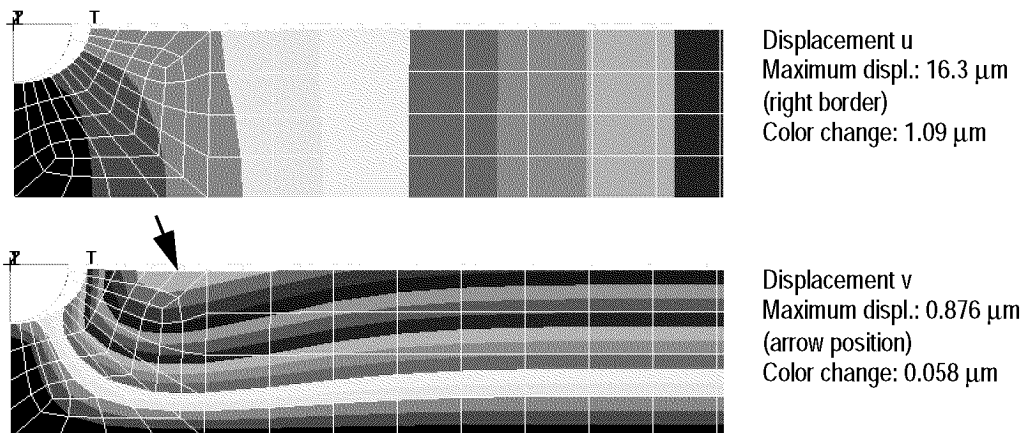
The notches in the test sample cause local stress concentrations. According to [92] the geometry shown in figure 9.3 yields a stress concentration factor of 3, which means that the stress at the notch ground will be three times higher than in the sample without notch.

The mechanical behaviour of the test sample under the applied load was calculated with the finite element software PATRAN. Since the problem is symmetric with respect to two axes, it is sufficient to model  $\frac{1}{4}$  of the

sample. We took into account the symmetry by blocking the corresponding degrees of freedom (translations, rotations). The tensile load is modeled as a negative edge pressure of  $33.0 \text{ N/mm}^2$ .

**Displacement** The finite element analysis yields the displacement fields  $u$  and  $v$  (figure 9.6) and the strain distributions  $\epsilon_x$ ,  $\epsilon_y$ , and  $\gamma_{xy}$  (figure 9.7). The displacement  $u$  between the center of the object and the clamping amounts to  $16.3 \mu\text{m}$ . The displacements  $v$  normal to the loading direction are much smaller than in loading direction: the maximum displacement is  $0.88 \mu\text{m}$  and appears at the location of the arrow in figure 9.6. The displacements are represented as different colours (or grey levels). From one colour to the next,  $u$  changes by  $1.09 \mu\text{m}$  and  $v$  by  $0.058 \mu\text{m}$ . Since the model was two-dimensional, the out-of-plane displacement  $w$  was not calculated. Only small values are expected near the notch ground caused by transversal contraction.

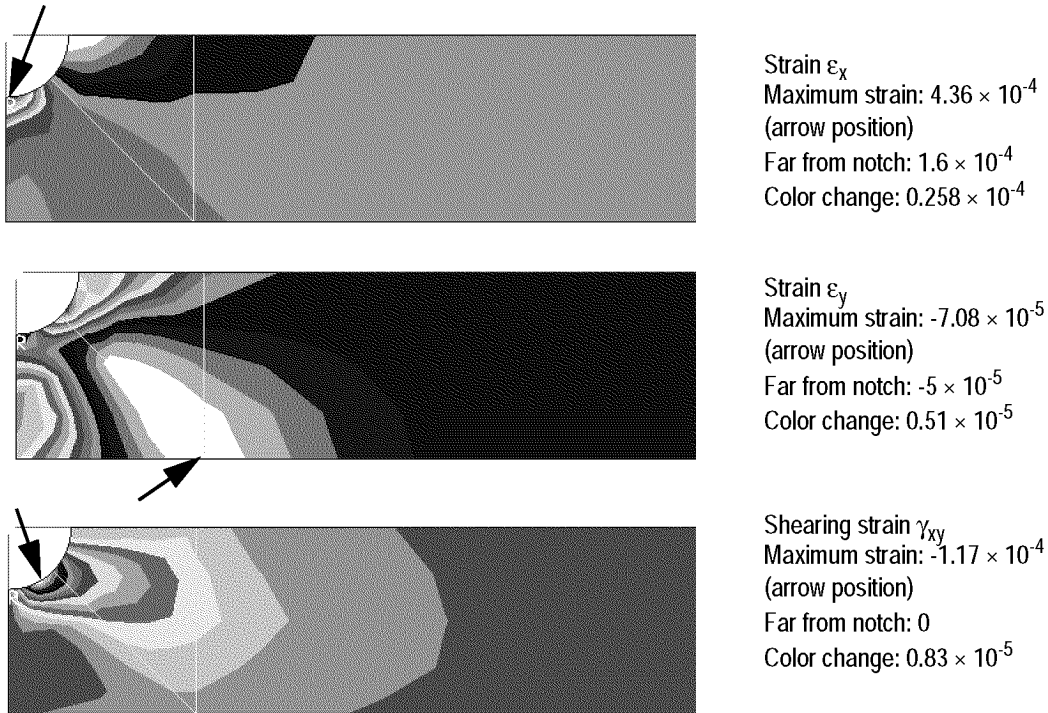
**Figure 9.6** Displacement fields  $u$  and  $v$  calculated with finite elements. The maximum  $u$  displacement appears at the right border, the maximum of  $v$  at the location of the arrow.



**Strains** In a sample without notch, the strain  $\epsilon_x$  would be  $1.63 \times 10^{-4}$ . The largest part of the notched sample also exposes a similar strain value. At the notch ground we expect the maximum strain, which in the FE analysis amounts to  $4.36 \times 10^{-4}$ . The strain  $\epsilon_y$  and the shearing strain  $\gamma_{xy}$  also show the effect of the notch. The maximum strain values are  $-7.08 \times 10^{-5}$  for  $\epsilon_y$  and  $-1.17 \times 10^{-4}$  for  $\gamma_{xy}$ . Far from the notch,  $\gamma_{xy}$  is zero.  $\epsilon_y$  amounts to approximately  $-5 \times 10^{-5}$ , in agreement with *Poisson's ratio* (eq.(2.27)). A change of the grey level in the strain maps corresponds to a strain difference of  $0.285 \times 10^{-4}$  ( $\epsilon_x$ ),  $0.51 \times 10^{-5}$  ( $\epsilon_y$ ), or  $0.83 \times 10^{-5}$  ( $\gamma_{xy}$ ).



**Figure 9.7** Strain distributions  $\epsilon_x$ ,  $\epsilon_y$ , and  $\gamma_{xy}$ , calculated with finite elements. The arrows point to the locations of maximum absolute strain.



### 9.2.3 Results of the Quantitative Evaluation

In order to determine the strain distributions from the shearography measurements, the evaluation method described in chapter 7 was followed. The graphical representation of this procedure (figure 7.2) is repeated here in figure 9.8, since we will often refer to this illustration.

- 18 phase images We mentioned above that the load was increased from 500 N to 2480 N in five steps. Therefore we recorded phase images at six load levels (not only two as in figure 9.8) and with three illumination modules, which resulted in 18 phase images that we stored for further processing.
- Region of interest In figure 9.5 we observe that not the whole image belongs to the test object. In order to minimize the processing time, the rows and columns outside the region of interest were removed. This reduced the size of each image from  $768 \times 572$  pixels to  $669 \times 341$  pixels.
- 3 filtered phase fringe patterns From the 18 phase images, we want to produce the three filtered and unwrapped phase maps  $\Delta\hat{\varphi}_1$ ,  $\Delta\hat{\varphi}_2$ ,  $\Delta\hat{\varphi}_3$ . This is done for each illumination direction individually. From the six images recorded with illumination module 1, we calculated five *phase fringe patterns*, corresponding to the differences between subsequent load levels. One example is shown in figure 9.9.

**Figure 9.8** The evaluation process for the determination of the strain components as explained in chapter 7.

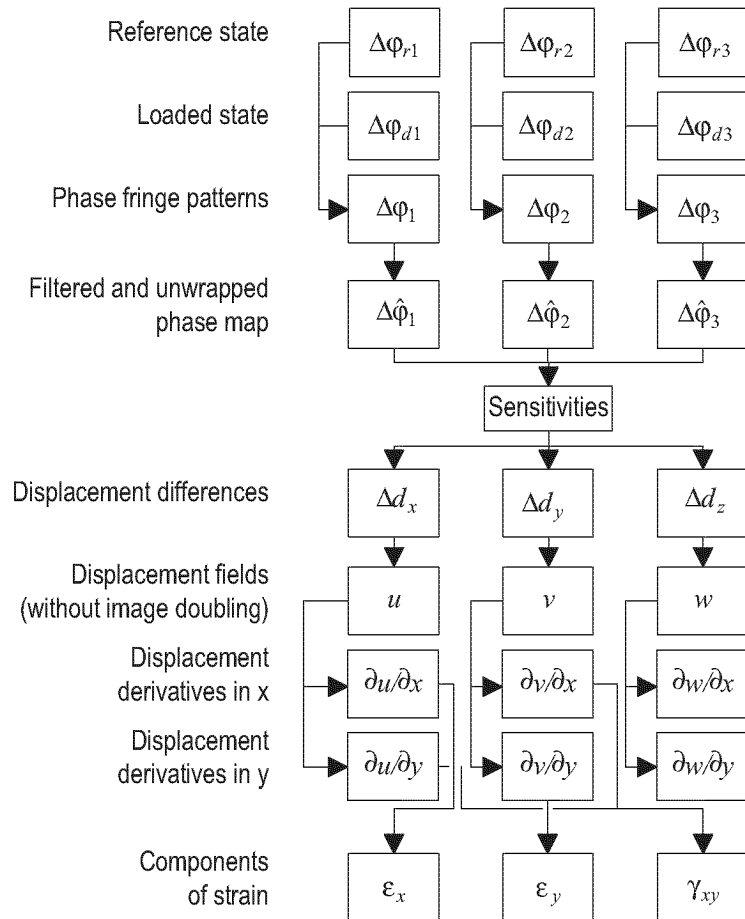
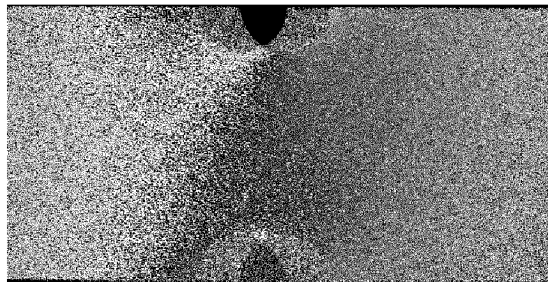


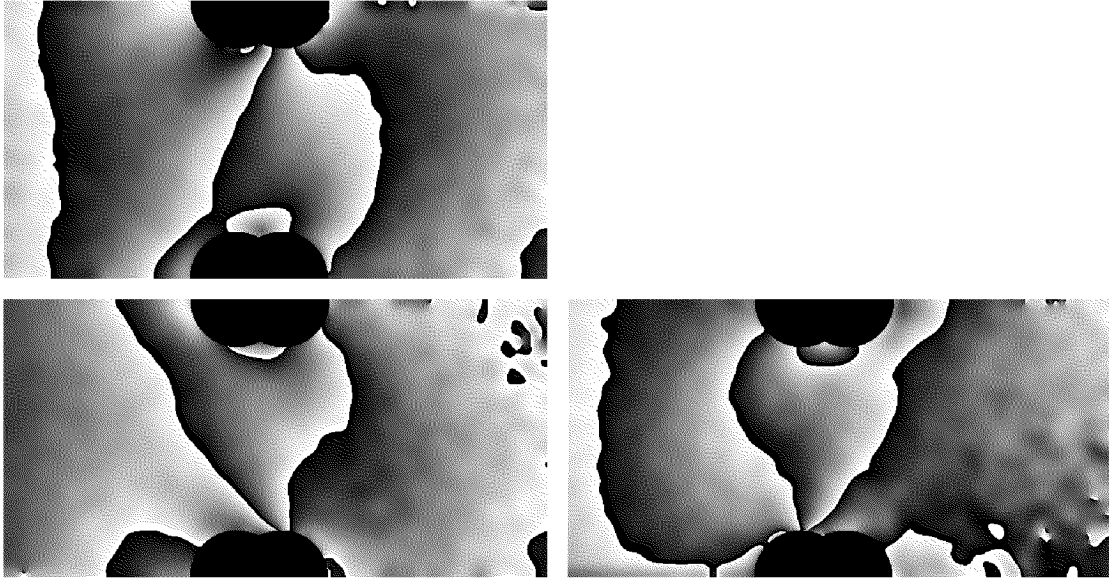
**Figure 9.9** Phase fringe pattern showing the phase difference between two subsequent load levels.



Each of these phase fringe patterns was filtered individually according to the method introduced in chapter 4, with 20 repetitions of a  $7 \times 7$  filter. The filtered phase fringe patterns were then added modulo  $2\pi$  and a mask was applied to hide the regions where the notches appear, resulting in the image in figure 9.10 a). This procedure was repeated for the images recorded with illumination module 2 and 3, which yielded the results in figure 9.10 b) and c). The modules are arranged as illustrated in figure 6.1. If we consider the gaps between the images in figure 9.10 as mirror lines, we observe a particular symmetry between the fringe patterns. This indicates that the deformation of the object is symmetric about two axes

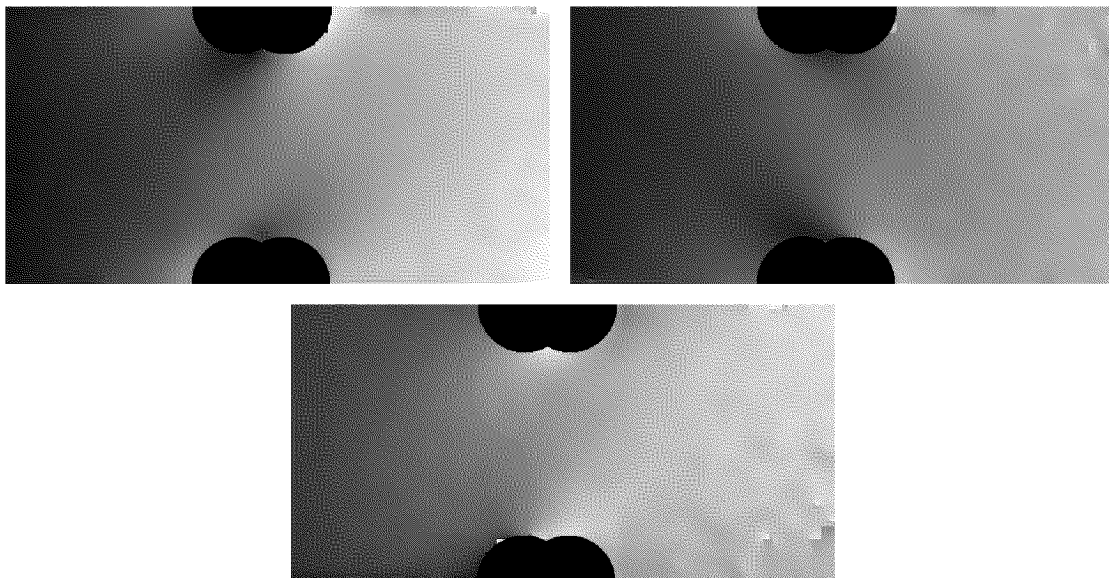
and that the variation of the fringe shape a), b) and c) reflects the variation of the illumination directions.

**Figure 9.10** a), b), c) Filtered and added phase fringe patterns from illumination modules 1, 2, and 3, respectively.



**Unwrapping** For further processing, the absolute phase values are necessary. We therefore unwrapped the phase fringe patterns measured with the three illumination modules (figure 9.10) and scaled them properly yielding the *filtered and unwrapped phase maps*  $\Delta\hat{\phi}_1$ ,  $\Delta\hat{\phi}_2$ ,  $\Delta\hat{\phi}_3$ . The values in these phase maps (shown in figure 9.11) are therefore not restricted to the range of 256 grey levels, but are the real-numbered phases.

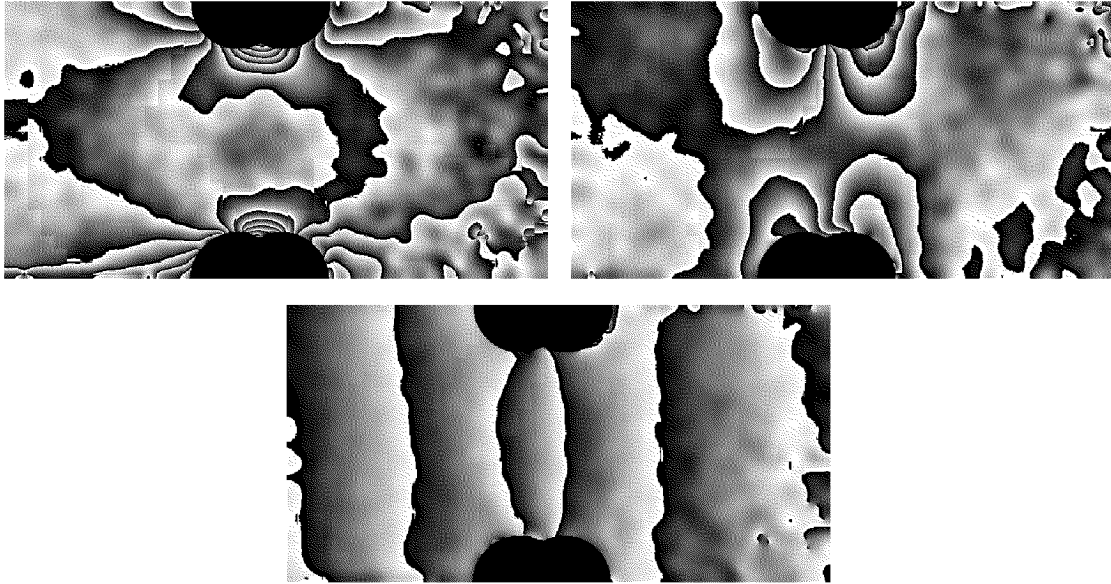
**Figure 9.11** The phase images for illumination modules 1, 2, and 3 are obtained by unwrapping the phase fringe patterns in figure 9.10.



**Displacement differences** Next, the *displacement differences*  $\Delta d_x$ ,  $\Delta d_y$ , and  $\Delta d_z$  in directions of the co-ordinate axes were calculated according to eq. (7.3). In order to obtain this result, the illumination and observation direction and the resulting

sensitivity were calculated for each pixel in order to take into account the spherical wave illumination. In figure 9.12 the resulting displacement differences are shown. For the representation as a fringe pattern, the results are shown wrapped modulo  $0.2\ \mu\text{m}$ , i.e. the displacement differences vary by  $0.2\ \mu\text{m}$  between two neighbouring fringes.

**Figure 9.12** From the three unwrapped phase images (figure 9.11) the displacement differences  $\Delta d_x$ ,  $\Delta d_y$ , and  $\Delta d_z$  are calculated.



Removing the image doubling

According to the procedure shown in figure 9.8, the next step is to calculate the *displacement fields* by removing the image doubling. The method described in chapter 5 was applied with the extension described in section 7.3.2: Since the shear distance of  $\Delta x = 5\ \text{mm}$  corresponds to  $\Delta \xi = 56.47$  pixels in the image, we used interpolation to calculate intermediate values.

Boundary conditions

In order to apply the method to remove the image doubling, one border of the image may not be deformed (see figure 5.4). An alternative is to use our knowledge about the deformation of the sample as a boundary condition. At the image border, i.e. far away from the notch, we may assume that  $\Delta d_y$ , and  $\Delta d_z$  are equal to zero.  $\Delta d_x$  is a constant given by

$$\Delta d_x = \varepsilon_x \cdot \Delta x = \frac{\Delta F}{A \cdot E} \cdot \Delta x, \quad (9.1)$$

where  $\Delta F = 1980\ \text{N}$  is applied load,  $A = 60\ \text{mm}^2$  is the cross-section of the sample,  $E = 210000\ \text{N/mm}^2$  is the elastic modulus, and  $\Delta x = 5\ \text{mm}$  is the shear distance. With these values,  $\Delta d_x$  amounts to  $0.7857\ \mu\text{m}$ .

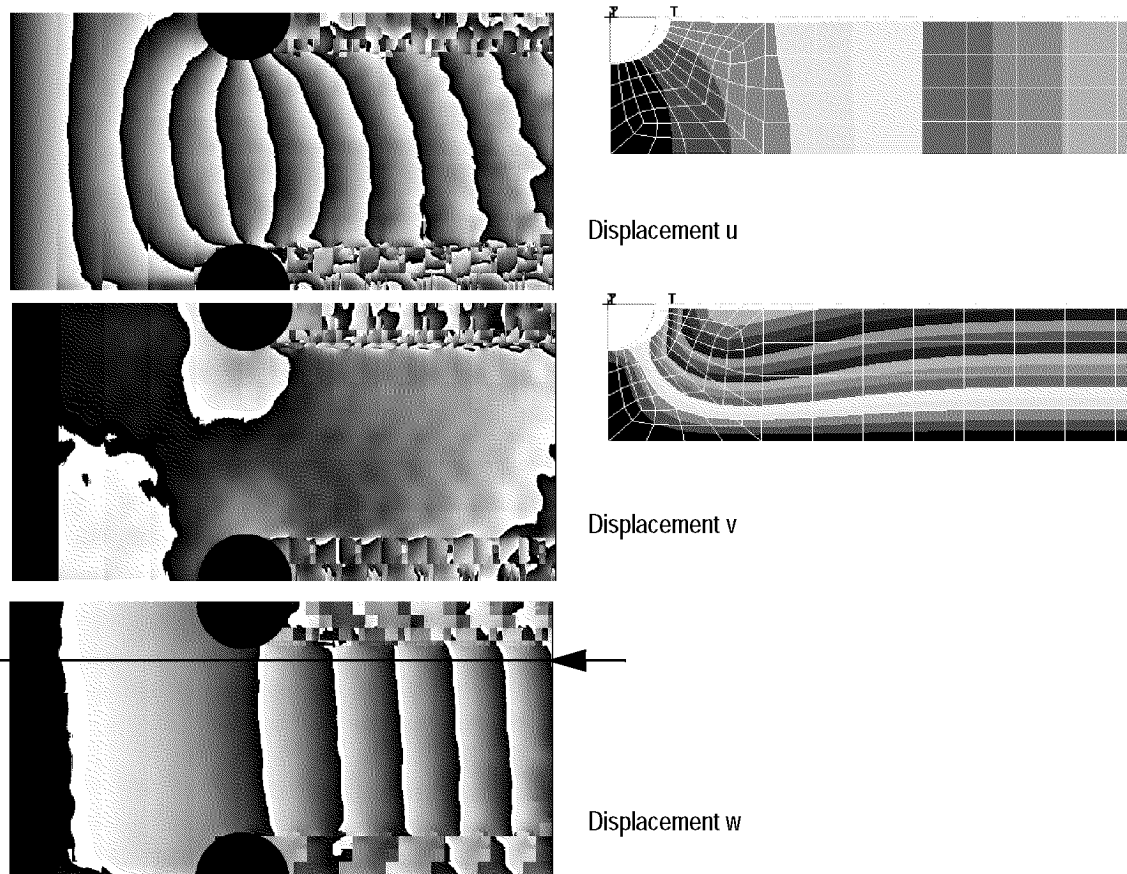
Displacement fields

Applying the method to the displacement differences (figure 9.12) yields the result shown in figure 9.13. Between two neighbouring fringes, the displacement varies by  $1\ \mu\text{m}$ . For a qualitative comparison, the calculated displacement fields  $u$  and  $v$  of figure 9.6 are shown here again next to the measurement results. The displacement  $u$  shows a good agreement; the displacement increases in  $x$  direction. But for  $v$  and  $w$  the results show a big difference. The out-of-plane displacement  $w$  should show the

transversal contraction near the notch ground and  $v$  should vary in  $y$  direction.

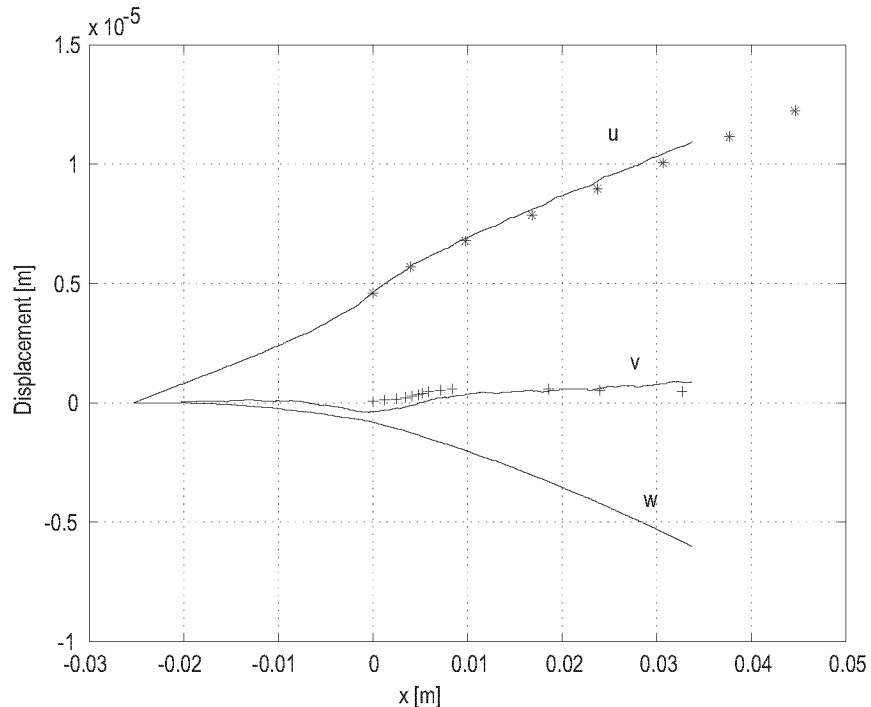
On the right side of the notches, only noise appears in the displacement fields. This is due to the procedure to remove the image doubling. To calculate the values right from the notch, values inside the area of the notch are contained in the summation. Since no interference occurs in this area, the results for the pixels right from the notches are invalid.

**Figure 9.13** The displacement fields  $u$ ,  $v$ , and  $w$  calculated with the method to remove the image doubling. A displacement of  $1\ \mu\text{m}$  corresponds to one fringe.



For a quantitative assessment, we evaluated the displacement fields along a horizontal line near the notch (see arrow in figure 9.13 c). The results are shown in figure 9.14. Along with the measured displacements (solid lines), the calculated displacements for  $u$  and  $v$  are drawn as stars and plus signs. The displacement  $u$  from the notch to the right border of the image ( $35.5\ \text{mm}$ ) amounts to  $6.7\ \mu\text{m}$ . This corresponds to a displacement of  $18.9\ \mu\text{m}$  over the half specimen length, whereas the calculated result (section 9.2.2) was  $16.3\ \mu\text{m}$ . As indicated by the calculation, the measured  $v$  displacements are much smaller than the  $u$  displacements. The out-of-plane displacement  $w$  shows that a bending of the test sample occurred.

**Figure 9.14** Displacements  $u$ ,  $v$ , and  $w$  evaluated along a horizontal line (see arrows in figure 9.13 c). For  $u$  and  $v$ , the results of the FE analysis are shown with \* and + signs, respectively.

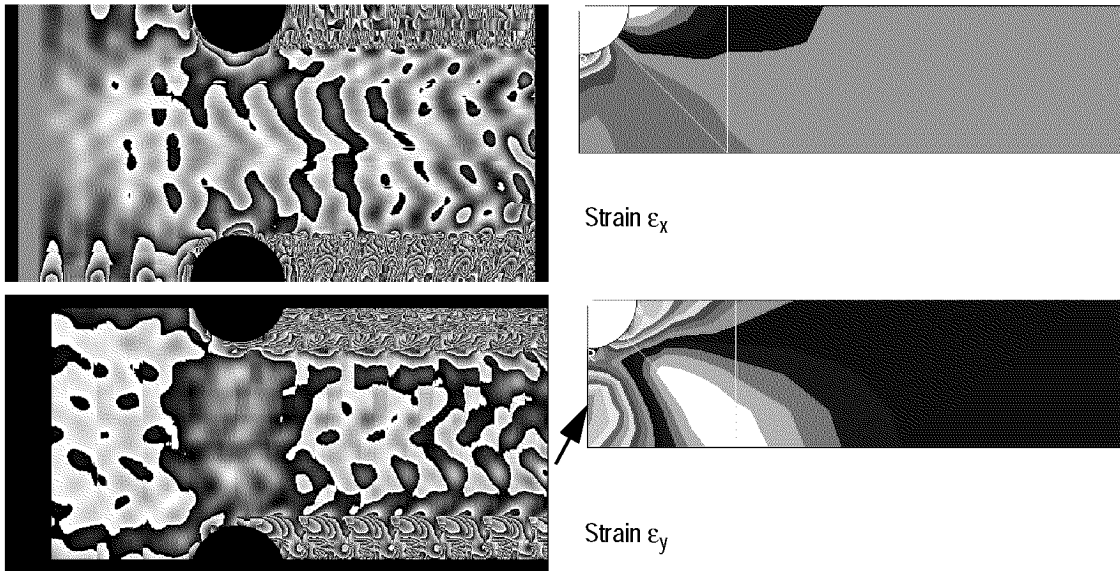


**Strains** According to figure 9.8 the next evaluation step is the determination of the *displacement derivatives*. Deriving  $u$  in  $x$  direction directly yields the strain (unit elongation)  $\epsilon_x$ , whereas  $v$  derived in  $y$  yields the strain  $\epsilon_y$ . In figure 9.15 these strain distributions are shown along with the calculated strains. From one fringe to the next, the strain in the measured images changes by  $1 \times 10^{-4}$  (or 0.01 %).

For the strain  $\epsilon_x$ , concentrations near the notches are clearly visible. Unfortunately, also two types of artefacts become obvious: Repeated ‘waves’ cover the images and the areas right of the notches, which contain only noise.

In the measured result for the strain  $\epsilon_y$ , elevated values appear in the region between the two notches. This elevation is also present in the calculated strain distribution. The rest of the fringe pattern does not agree well with the calculated strains.

**Figure 9.15** The strain distributions  $\epsilon_x$  and  $\epsilon_y$  derived from the displacement fields  $u$  and  $v$ . 0.01 % correspond to one fringe. The calculated strain distributions  $\epsilon_x$  and  $\epsilon_y$  are shown on the right side for comparison.



The quantitative comparison of the measured with the calculated strains is again done by evaluating a horizontal line. The strain  $\epsilon_x$  along a horizontal line tangent to the notch is shown in figure 9.16. From figure 9.7 the strains along the same line were determined. The measured (solid line) and the calculated values (\* signs) match very well in the left half of the specimen. The numerical values of the peak value near the notch ground and the average value far from the notch do also agree well. These values are compiled in table 9.1.

**Figure 9.16** Strain  $\epsilon_x$  along a horizontal line tangent to the notch. The result from the FE calculation is marked with \* signs.

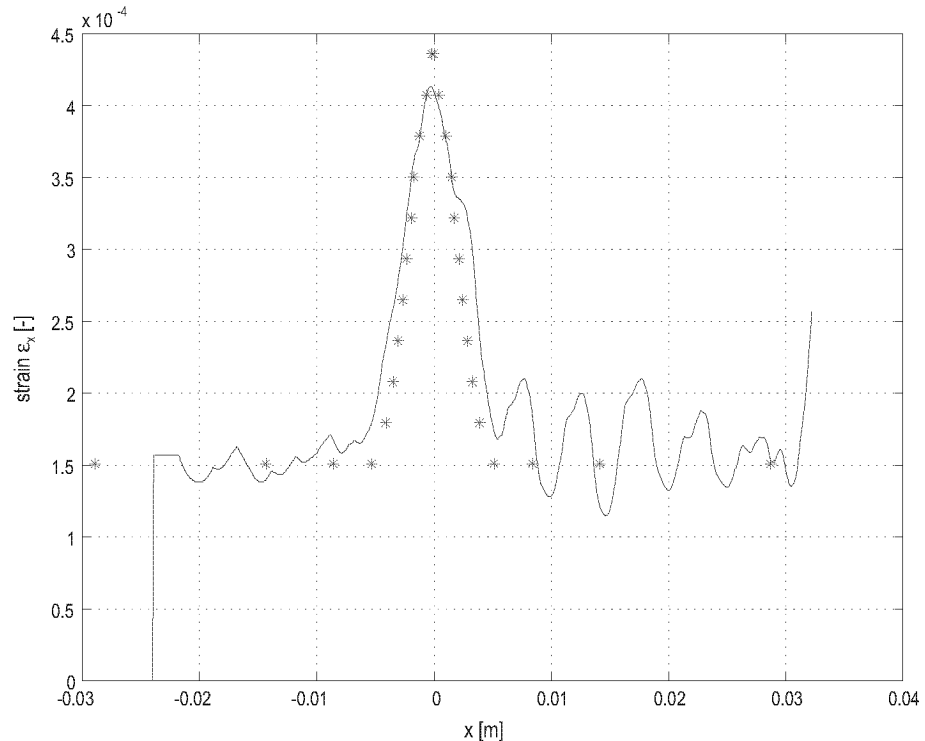
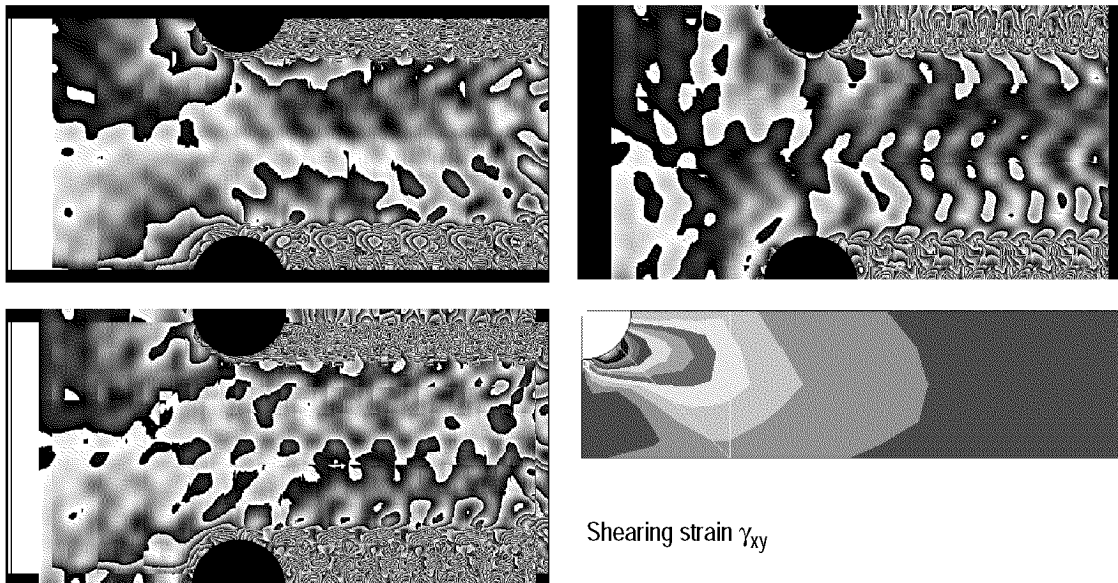


**Table 9.1** Strain values  $\epsilon_x$  near the notch ground and far from the notch.

	$\epsilon_x$ calculated	$\epsilon_x$ measured
Peak value	$4.36 \times 10^{-4}$	$4.1 \times 10^{-4}$
Far from notch	$1.6 \times 10^{-4}$	$(1.5 \pm 0.5) \times 10^{-4}$

Shearing strain Figure 9.17 shows the two displacement derivative maps  $\partial u/\partial y$  and  $\partial v/\partial x$ . The addition of these two maps yields the shearing strain  $\gamma_{xy}$ . Again, a wavy pattern appears. The measured result does not resemble the calculated shearing strains shown in figure 9.17 d).

**Figure 9.17** From the displacement derivatives  $\partial u/\partial y$  (a) and  $\partial v/\partial x$  (b) the shearing strain  $\gamma_{xy}$  (c) is calculated. d) The shearing strains calculated with FEM.



## 9.2.4 Discussion

**Results** The concept for quantitative strain analysis proposed in chapter 7 was successfully realized and carried out with a first measurement. The experiment was simulated with a finite element calculation for the qualitative and quantitative comparison with the measurement results. As a result of the evaluation of the measurements, we obtained the strain fields  $\epsilon_x$ ,  $\epsilon_y$ , and  $\gamma_{xy}$ .

**$u, v, w$**  The displacement fields  $u, v, w$  were calculated as intermediate results. Their comparison with the simulated results showed a good agreement for the in-plane displacements  $u$  and  $v$ , whereas the out-of-plane component  $w$  revealed a bending of the specimen.

**$\epsilon_x$**  The largest strain component  $\epsilon_x$  shows an acceptable result. The strain concentration near the notches was determined from the measurement with an accuracy of 6%. Also the averaged strain far from the notch is close to the expected value. On the other hand, the strain distribution is not smooth, but varies considerably – a ‘wavy’ structure appears.

**$\epsilon_y, \gamma_{xy}$**  The results for the strain  $\epsilon_y$  and the shearing strain  $\gamma_{xy}$  are not satisfactory. While the measurement result for  $\epsilon_y$  shows a qualitative resemblance with



the calculated result, the distribution of  $\gamma_{xy}$  is completely different from the calculation. The above mentioned wave structure is dominant.

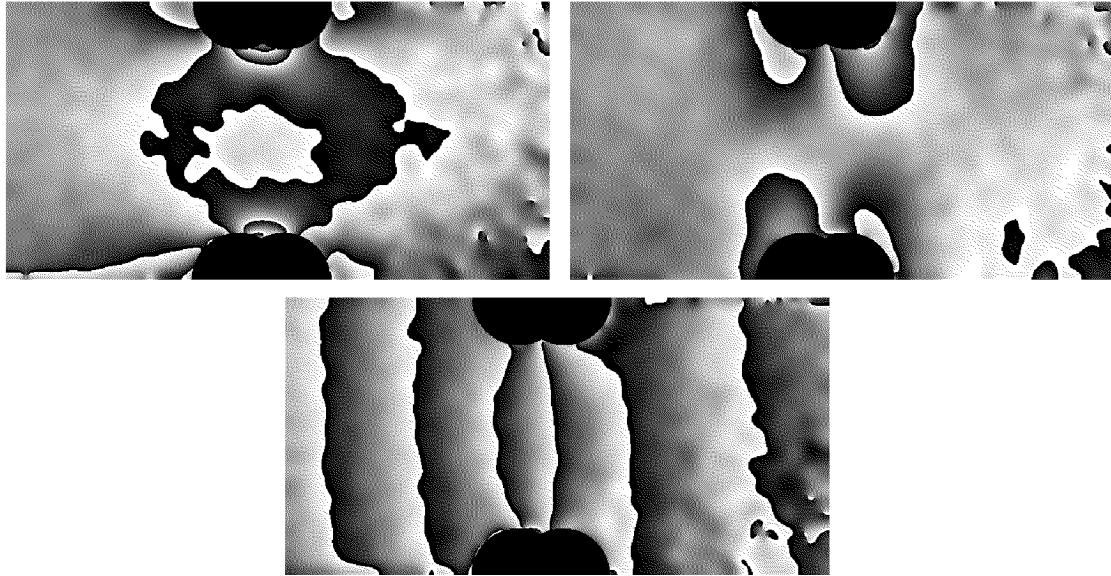
Correct evaluation	The individual processing steps used in the evaluation have been successfully validated in the previous chapters. In the evaluation sequence, the results of the displacement differences (figure 9.12) and of the displacement fields (figure 9.13) are of acceptable quality. The unsatisfactory quality of the final results is the consequence of small errors in the measurement and evaluation steps, which are emphasized in the course of the evaluation process.
Error sources	The principal sources of errors are the phase unwrapping and the displacement field calculation (removing of the image doubling). For the phase unwrapping, PISA's "Puzzle" algorithm – one of the most advanced algorithms (see section 4.6) – was used. While the quality of the unwrapped phase maps in figure 9.11 seems to be excellent, discontinuities at the borders of unwrapped blocks become apparent in the displacement differences (figure 9.12) and later in the evaluation. The method to remove the image doubling, which works in principle, also introduces considerable errors. These errors (spatial discontinuities) are repeated and emphasized from the left to the right of the image (see section 5.4). While these discontinuities remain at an acceptable level in the displacement fields (figure 9.13), the derivative operation emphasizes them, producing the 'wavy' structure in the derived fringe patterns. The spatial frequency of these waves agrees with the shear distance, which indicates that these errors are caused by the removal of the image doubling. A second weakness is that the area on the right side of the notches can not be evaluated. A further source of errors is not located in the evaluation procedure: The measured bending of the test sample was caused by an asymmetry of the test sample or of the load introduction.
Possible improvements	The mentioned sources of errors already indicate how the strain analysis method can be improved. An enhanced phase unwrapping method or the use of dynamic phase shifting, which makes the unwrapping obsolete, is one necessary step. The second is the improvement of the method to remove the image doubling. The alternative methods mentioned in section 5.6 may show the way to a better realisation of the idea.

## 9.2.5 Comparison with Other Published Work

---

Approximate displacement derivatives	According to chapter 6, approximations to the displacement derivatives $\partial u/\partial x$ , $\partial v/\partial x$ , and $\partial w/\partial x$ can be visualized by simply adding and subtracting the phase fringe patterns from the three illumination directions (eqs. (6.7)). With shear in $y$ direction, the approximations to $\partial u/\partial y$ , $\partial v/\partial y$ , and $\partial w/\partial y$ can be obtained. These approximations do not take into account the shear distance and the variation of the illumination direction due to the spherical wave illumination. In figure 9.18 the results of these operations – directly extracted from the fringe patterns in figure 9.10 – are shown. These fringe patterns may qualitatively illustrate the strain distributions but do not deliver quantitative results.
--------------------------------------	---

**Figure 9.18** Approximations to the displacement derivatives  $\partial u/\partial x$ ,  $\partial v/\partial x$ , and  $\partial w/\partial x$ . The shear distance and the variation of the illumination direction are not considered.



Work of  
Schuth and  
Yang

This evaluation is identical to the one used by Schuth [41] and Yang [93] in their theses for strain analysis. The reason why they obtained relatively good results with this method is that they used ARALDIT as material for the test samples. This material is often used for photo-elastic models, but rarely as structural material. Such materials have an elastic modulus in the range of 1000 to 3000 N/mm<sup>2</sup>, compared with 210'000 N/mm<sup>2</sup> for steel. The deformations are therefore much larger than with an engineering material, which allows for reducing the shear distance and the applied force. A smaller force considerably simplifies the device to load the object, and with a small shear distance, the displacement difference approximates the displacement derivative well.

In this chapter we have performed the quantitative strain analysis, which was the goal of the present work. Still, the methods and equipment developed in this work may also be of interest for other applications. This is the topic of the next chapter “Further Applications of the Developed Techniques”.

CHAPTER  
10

## FURTHER APPLICATIONS OF THE DEVELOPED TECHNIQUES

As indicated in the lower part of figure 1.4 (page 7), the developed methods not only serve for the quantitative strain analysis with shearography, but may also be useful in other applications, e.g. in conventional shearography and in ESPI. In this chapter we show further applications of the new filter method, the removal of the image doubling, the quantitative evaluation, and the equipment developed in this work.

### 10.1 Filtering of Phase Fringe Patterns

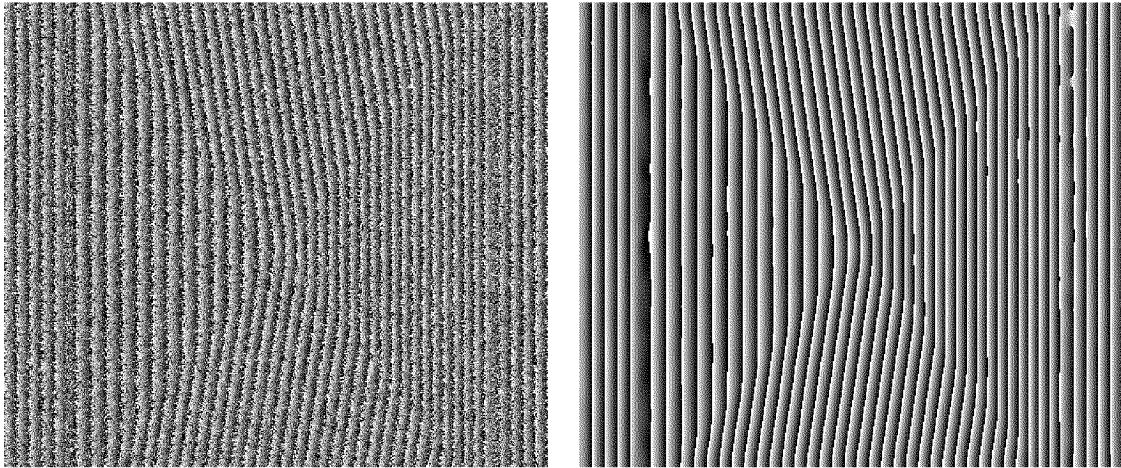
---

The multiply repeated anisotropic sine/cosine filter presented in chapter 4 effectively removes the noise from phase fringe patterns. For the strain measurement with shearography this is vital, since a series of image processing steps is necessary to extract the wanted quantitative results. Of course, the relevance of this filter is not limited to this application. It can be of favour wherever noise has to be removed from phase fringe patterns.

**Shearography  
NDT** The demonstration example in chapter 4 is the qualitative detection of a delamination with shearography. The result in figure 4.5 shows the defect much clearer than the original result in figure 4.2 – at least for the inexperienced observer.

**ESPI shape  
measurement** A further example is shown in figure 10.1. The shape of a pyramid is measured with the ESPI set-up proposed by Wang et al. [94]. As the fringes are predominantly oriented in vertical direction, the anisotropic filtering with a larger filter strength in vertical direction leads to a very good result. It does not affect the fine details of the fringe pattern, allowing for an accurate determination of the objects' z co-ordinate from the fringe pattern.

**Figure 10.1** Example of an ESPI shape measurement: a) The measured phase fringe pattern; b) the fringe pattern a) after 20 repetitions of filtering with a  $7 \times 3$  filter. (Courtesy of Nicolas Goudemand, ETH Zürich).



Other potential fields of application are holographic interferometry and Moiré techniques.

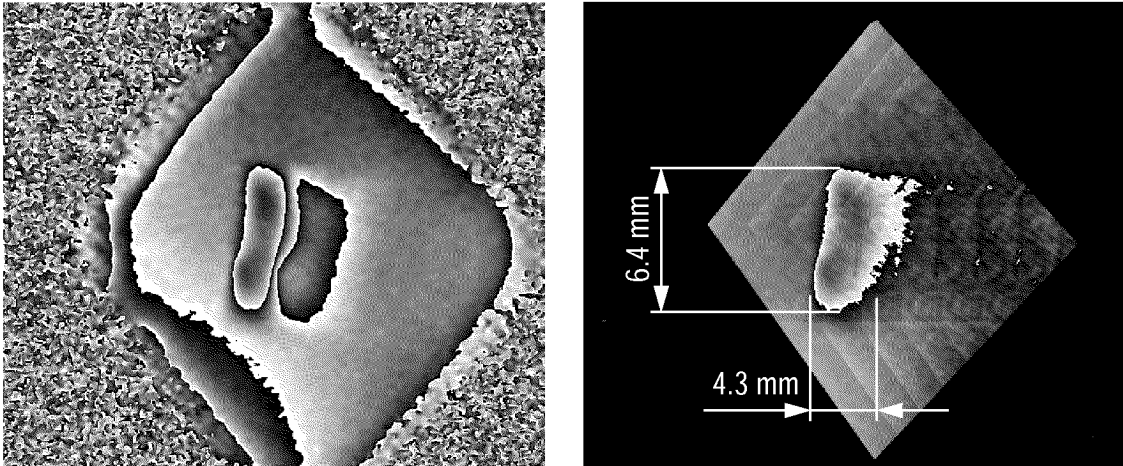
## 10.2 Removing the Image Doubling

The effect of image doubling is specific to shearography. Its removal is important for the quantitative evaluation of in-plane measurements, as demonstrated in chapter 9.

**Out-of-plane shearography** But the method is also suitable for out-of-plane applications, as it facilitates the interpretation and quantitative evaluation. The example of the clamped circular plate with comparison of the measured and calculated results in section 5.4 shows this clearly.

**Qualitative NDT** Even if one is only interested in the location and size of a defect, and not in the quantity of deformation, the method is advantageous. Figure 10.2 shows such an example: It is a preliminary test to find defects in a “glob top” encapsulation for chip-on-board applications. Epoxy was dispensed on an electronic circuit board on which a folded Teflon tape was laid. This tape simulated a flaw in the glob top. The specimen was loaded by heating with an infrared lamp and measured with shearography.  $27 \text{ mm} \times 20 \text{ mm}$  of the object were imaged and the shear distance  $\Delta x$  was 2 mm (corresponding to 38 pixels in the image). Three incremental phase fringe patterns were recorded, filtered and added modulo  $2\pi$  to obtain figure 10.2 a). As only the part of the specimen covered with epoxy was illuminated, the area outside this quadratic region contains only noise. Figure 10.2 b) shows the out-of-plane displacement field calculated from figure 10.2 a). Comparing the two images, the outline of the simulated flaw seems to be wider in a) than in b). This is the effect of the image-shear which stretches the deformed region in the shear direction. After removing the image shear, the correct size and location of the flaw can be quantified.

**Figure 10.2** a) Shearographic measurement of a simulated flaw in a patch of epoxy.  
 b) The displacement field calculated from the left image. Since the image shear is removed, the correct size of the flaw can be determined [69].



Plasma science The publication on the removal of the image doubling [68] was also cited in a rather unexpected context: In an article in the “IEEE Transactions on Plasma Science” [95] the authors measure the electron density and current of a plasma with shearing interferometry and propose the method to remove the image doubling as a ‘more sophisticated numerical procedure’ for the evaluation of the results.

### 10.3 Quantitative Evaluation

The quantitative evaluation in chapter 7 aims at extracting the relevant physical data from the measurements. For 3D strain measurement, this procedure is rather complex.

Out-of-plane shearography For the quantitative evaluation of pure out-of-plane measurements, the process is simpler. With illumination approximately perpendicular to the object surface, the in-plane components can be neglected and the measured phase difference (eq. (2.16)) simplifies to

$$\Delta\varphi = k_z \cdot \Delta d_z, \text{ where } k_z = \frac{2\pi}{\lambda} \cdot (1 + \cos\theta_s). \quad (10.1)$$

The cosine varies slowly close to  $\theta_s = 0$ , the influence of the variation of the illumination angle (with spherical wave illumination) on the measurement sensitivity is therefore negligibly small.

The quantitative evaluation for out-of-plane shearography consists in removing the image doubling and scaling the result with a constant sensitivity, as demonstrated in section 5.4.

ESPI For the quantitative evaluation of in-plane ESPI measurements, the developed procedure is also partially applicable. If the object is illuminated with spherical waves (see figure 2.9), a considerable error is caused by assuming constant sensitivity for the whole object. For the quantitative evaluation – e.g. of figure 1.3 – the variation of the sensitivity vector  $\mathbf{k}$  should be taken into account.

## 10.4 Specific Equipment

---

The shearography system was designed with the possibility to realise two set-ups. The shearography head combined with three illumination modules is used for the measurement of in-plane strain, the set-up with one illumination module for out-of-plane measurements. This 1D set-up – shown in figure 8.10 – is very compact and easy to handle.

**Quantitative out-of-plane** An example of the application of the shearography system to the quantitative analysis of out-of-plane deformation is documented in section 9.1.2, where a clamped circular plate is investigated.

**Qualitative NDT** Of course, our shearography system can also be applied to qualitative non-destructive testing. The system is very compact; it can be brought to the component that is to be tested. For such on-site tests, safety is an important issue. Since we selected a laser that emits visible light, the risk of exposing the eyes to the laser beam is much smaller than with invisible (e.g. infrared) lasers.

**Adjusting the sensitivity** The measurement sensitivity is directly related to the shear distance and the shear distance can be remotely controlled from the computer. It is therefore possible to reduce or increase the measurement sensitivity from the PC. This is a clear advantage of our system, because the shearography head is often difficult to access during a measurement.

The above remarks show that the developed equipment as well as the image processing is suitable not only for shearographic strain measurement, but may find application in various other fields of optical measurement and testing.

CHAPTER  
11

## CONCLUSIONS

In this final chapter, the main achievements that were realized in this work are summarized. Then the advantages and drawbacks of the developed method in comparison with ESPI are discussed. Finally, the points that appeared as being critical are identified and suggestions are made, how the method could be further improved.

### 11.1 Summary of the Main Achievements

---

The goal of this work was to develop a method for quantitative strain analysis based on image-shearing speckle pattern interferometry (shearography). We identified three basic problems of shearography that impeded this development:

- Since two speckle patterns sheared against each other interfere in the image plane, the measured phase fringe patterns contain a high level of noise.
- The shearing of the images causes a doubled image in the result of the measurement. The amount of shear directly influences the measurement sensitivity. It is thus not desirable to minimize the shear distance: the sensitivity would also be minimized.
- Generally, a mixture of all directions of the object deformation is contained in the measured result. Only the out-of-plane components can be isolated with an adapted optical set-up. Isolating the in-plane components with the optical set-up – which is possible in ESPI – is not possible with shearography.

#### 11.1.1 Solution of the Principal Problems

---

These problems have been addressed and solutions have been proposed in Chapter 4, “Filtering of Phase Fringe Patterns and Phase Unwrapping”, Chapter 5, “Removing the Image Doubling”, and Chapter 6, “Isolation of the Components”.

New filter method We have developed the multiply repeated anisotropic sine/cosine filter, which removes the noise effectively without affecting the fine details of

the fringe patterns. This filter clearly outperforms the best filters for phase fringe patterns that are available in literature or in commercial programs.

Removing the image doubling

We have analysed the problem of image doubling theoretically and found a simple solution to solve this problem. By addition of particular phase values, the displacement field is determined from the shearography result – cancelling the influence of the shear distance. The method is demonstrated with a simulated example as well as with measured examples.

Isolation of components

We have shown that from three measurements with three independent sensitivity directions, the components of deformation can be isolated. A special arrangement of the (plane wave) illumination sources allows for the isolation of the components by simple addition and subtraction of the measured phase fringe patterns.

### 11.1.2 Concept for Quantitative Strain Analysis

---

Detailed evaluation procedure

In Chapter 7, “Quantitative Evaluation”, we propose a detailed concept for the measurement of the strain components  $\epsilon_x$ ,  $\epsilon_y$  and  $\gamma_{xy}$ . Starting from the measured phase images, extensive image processing is necessary to obtain quantitative results. The newly developed methods for filtering, for the removal of the image doubling, and the isolation of components are all integrated in this evaluation procedure. For the proposed procedure, only measurements with one shear direction are necessary.

### 11.1.3 Development of Specific Equipment

---

We have developed special equipment for the strain measurement with shearography (Chapter 8, “Development of Adapted Equipment”). A compact shearography head was designed and realized, which is based on a Michelson interferometer set-up. Three independent illumination modules were realized with lasers emitting visible light.

Computer-controlled measurement

The phase shift, the adjustment of the distance and direction of shear, and the switching of the illumination sources are controlled by the computer. For this purpose we developed electronics and software functions, which allowed us to automate the measurement procedure. The whole system is portable and can be mounted on a tripod. Special vibration isolation is not necessary.

### 11.1.4 Experimental Demonstration

---

In Chapter 9, “Quantitative Strain Analysis” we brought all the developed equipment and the image processing routines together for a first experimental demonstration of the quantitative strain analysis.

Feasibility demonstrated

These first results indicate that the strain analysis method and the equipment may be able to provide quantitative results. The displacement fields and the principal strain  $\epsilon_x$  were evaluated and showed a good agreement with the simulated results. The evaluation of the strains  $\epsilon_y$  and



$\gamma_{xy}$ , on the other hand, did not lead to meaningful results. We revealed weak points in the evaluation procedure, which have to be addressed in order to obtain reliable accurate results.

## 11.2 Comparison with ESPI

---

In order to determine the strain components with ESPI, a procedure similar to that shown in figure 7.2 has to be followed. The main difference to the shearography procedure is that the transformation of the displacement differences to the displacement fields – i.e. the removal of the image doubling – is not necessary. All the other processing steps are needed except for the case of plane wave illumination, where a set-up can be realized such that the filtered and unwrapped phase map  $\Delta\hat{\phi}_1$  is directly related to  $u$ ,  $\Delta\hat{\phi}_2$  to  $v$ , and  $\Delta\hat{\phi}_3$  to  $w$ .

**Advantages of ESPI** In section 9.2.4 we identified the removal of the image doubling as one of the principal sources of error in the strain analysis with shearography. Since this evaluation step is not necessary for ESPI measurements, it is easier to obtain accurate quantitative results with ESPI. Furthermore, ESPI measurements are usually less noisy than shearography measurements (see e.g. figure 5.11), which reduces the need for sophisticated filter methods.

**Advantages of shearography** The two main advantages of ‘classical’ shearography over ESPI are also valid for the strain measurement: The susceptibility to vibrations is considerably smaller and the measurement sensitivity can be easily altered by adjusting the shear distance. In the experimental demonstration, vibrations generated by the testing machine did not disturb the measurements; mounting the measuring head directly on the testing machine – as preferred for ESPI measurements [10] – is not necessary.

At the current state of development, quantitative strain analysis is still easier and more accurate with ESPI. But if vibrations and the sensitivity range are an important issue, shearography is the method of choice. We are sure that this work has extended the application range of shearography towards fields, which before have been reserved to ESPI. The further development of the strain analysis with shearography may lead to the situation that the same quality and accuracy of results as with ESPI can be obtained, but with all the advantages of the shearography technique. The actual subjects for improving the strain analysis with shearography are the topic of the next section.

## 11.3 Further Work

---

Several ideas for improvements were generated during this work, which could not be realized within the scope of this thesis. Furthermore, the experiments in chapter 9 have revealed the weak points in the practical application of the evaluation procedure as well as of the equipment.

Phase determination	For the determination of the phase from the measured intensity images, the dynamic phase shifting (described in section 3.3) may offer new possibilities. This method yields the absolute phase change and not only the phase modulo $2\pi$ , which makes phase unwrapping obsolete.
Filtering	Although the results of the filter method proposed in chapter 4 are generally considered as being excellent, the quantitative proof of the filter's superiority is missing. Also the mechanism leading to the good result is not fully understood. A problem exists at discontinuities (e.g. the notches in the tensile sample), where valid data is mixed together with invalid data from the area of the notch. A further progress would be the automatic selection of the optimum filter parameters (strength in horizontal and vertical direction and number of repetitions) and a faster processing.
Removing the image doubling	The method developed in chapter 5, which turned out to be one of the main sources of errors, should be compared with the two alternative methods mentioned in section 5.6. This would suggest, which method is the best for a given type of measurement, or may produce ideas for a new, improved method.
Quantitative evaluation	We decided to perform measurements with only one shear direction. Measuring with two shear directions would produce redundant information, which might be used to improve the accuracy of the results. The evaluation procedure, which was realized in MATLAB has to be integrated in a commercial software for regular use.
Equipment	<p>The shearography system described in chapter 8 was the first integrated optical measurement system developed at our institute. Although it comprises some innovative features, the development was successful: The performance of this first prototype is very good. Still, some details of the system could be improved:</p> <ul style="list-style-type: none"> <li>• The stiffness of the mounting system for the illumination modules should be improved. Additional cross connections are recommended.</li> <li>• The adjustment of the pinhole apertures in the illumination modules is difficult. The screws should be replaced by screws with a finer pitch.</li> <li>• The control of the servos for adjusting the shear distance is accurate enough for normal applications. If it would be possible to adjust the mirror with such an accuracy that correlation can be obtained after readjustment, it would be possible to perform measurements with two shear directions with loading the object only once. This is not possible so far.</li> <li>• The additional lens that shifts the image plane reduces the field of view and degrades the image quality. The lens system works in principle (figure 9.1 was measured in this way), but for the strain analysis we modified the system (section 9.2.1) to obtain better results. A larger lens with high quality would surely improve the image quality.</li> </ul>
Application range	The developed strain analysis method was tested with only one complete measurement and evaluation series. More experiments and theoretical

considerations are necessary in order to assess the application range, e.g. in which range strain values can be measured by varying the shear distance or the optical set-up.

## 11.4 Concluding Remark

---

In my personal opinion, quantitative strain analysis with shearography has the potential to become a valuable measurement method. I hope that this work contains valuable concepts as well as solutions to some of the problems of the technique. The first measurements yielded promising results but also showed that more work and good ideas are necessary in order to turn quantitative strain analysis with shearography into a reliable and accurate measurement method.



# CHAPTER 12

## REFERENCES

- Chapter 1
- 1 R. T. Reese, W. A. Kawahara (eds.), *Handbook on structural testing*, copublished by Society for Experimental Mechanics, Lilburn, GA: The Fairmont Press, 1993.
  - 2 A. L. Window (ed.), *Strain gauge technology*, 2<sup>nd</sup> ed., London (etc.): Elsevier Applied Science, 1992.
  - 3 J. W. Dally, W. F. Riley, *Experimental stress analysis*, 3<sup>rd</sup> ed., New York (etc.): McGraw-Hill, 1991.
  - 4 R. Jones, C. Wykes, *Holographic and speckle interferometry*, 2<sup>nd</sup> ed., Cambridge University Press, 1989.
  - 5 R. Dändliker, P. Jacquot, *Holographic interferometry and speckle methods*, Chapter 23 in: E. Wagner, R. Daendliker, K. Spenner (eds.), *Optical sensors*, Weinheim (etc.), VCH Verlagsgesellschaft, 1992, pp. 589-628.
  - 6 T. Floureaux, *Improvement of Electronic Speckle Fringes by Addition of Incremental Images*, *Optics & Laser Technology*, 25(4) (1993), pp. 255-258.
  - 7 M. Hertwig, T. Flemming, R. Usinger, *Speckle Interferometry for Detection of Sub-Surface Damage in Fibre-Reinforced Composites*, *Measurement Science and Technology*, 5 (1994), pp. 100-104.
  - 8 M. Hertwig, T. Flemming, T. Floureaux, H. A. Aebischer, *Speckle Interferometric Damage Investigation of Fibre-Reinforced Composites*, *Optics and Lasers in Engineering*, special issue "Optical Phase Shifting Methods Applied to Interferometric Measurement of Solid Deformation", 23 (1995), pp. 485-504.
  - 9 A. Ettemeyer, *Noncontact and Whole Field Strain Analysis with a Laser-Optical Strain Sensor*, *Materials evaluation*, Vol. 53, No. 12 (Dec. 1995), pp. 1336-37.
  - 10 A. Ettemeyer, Z. Wang, T. Walz, *Applications of 3D speckle interferometry to material and component testing*, SPIE Vol. 3098, *Optical Inspection and Micromasurements II*, Christophe Gorecki, Ed. (1997), pp. 188-194.
  - 11 J. A. Leendertz, J. N. Butters, *An image-shearing speckle-pattern interferometer for measuring bending moments*, *Journal of Physics E: Scientific Instruments* Vol. 6 (1973), pp. 1107-1110.

- 12 Y. Y. Hung, C. E. Taylor, *Speckle-Shearing Interferometric Camera – A Tool for Measurement of Derivatives of Surface Displacement*, Proceedings of Photo-optical Instrumentation Engineers (SPIE), Vol. 41 (1973), pp. 169-175.
- 13 Y. Y. Hung, *Speckle-Shearing Interferometric Camera – A Tool for Measurement of Derivatives of Surface-Displacement*, T. & A. M. Report No. 374, University of Illinois, 1973.
- 14 Y. Y. Hung, *Shearography: A new optical method for strain measurement and nondestructive testing*, Optical Engineering, Vol. 21, No. 3 (May/June 1982), pp. 391-395.
- 15 S. Nakadate, T. Yatagai, H. Saito, *Digital speckle-pattern shearing interferometry*, Applied Optics, Vol. 19 (1980), No. 24, pp. 4241-4246.
- 16 H. Kadono, S. Toyooka, Y. Iwasaki, *Speckle-shearing interferometry using a liquid-crystal cell as a phase modulator*, Journal of the Optical Society of America A, Vol. 8, No. 12 (December 1991), pp. 2001-2008.
- 17 N. Krishna Mohan, P. J. Masalkar, R. S. Sirohi, *Separation of the influence of in-plane displacement in multiaperture speckle shear interferometry*, Optical Engineering, Vol. 33, No. 6 (June 1994), pp. 1973-1982.
- 18 R. F. Anastasi, S. M. Serabian, R. J. Shuford, D. K. Das-Gupta, *Nondestructive Detection of simulated delaminations in composite laminates by Laser-Speckle Shearography*, Experimental Techniques, Vol. 11, No. 6 (June 1987), pp. 28-31.
- 19 D. W. Templeton, Y. Y. Hung, *Computerization of Data Deduction in Shearography*, SPIE Vol. 814 Photomechanics and Speckle Metrology (1987), pp. 116-123.
- 20 H. A. Aebischer, S. Waldner, *Strain Distributions Made Visible with Image-Shearing Speckle Pattern Interferometry*, Optics and Lasers in Engineering, Vol. 26, Nos. 4-5, Special issue on Speckle and Speckle Shearing Interferometry - II (March 1997), pp. 407-420.
- 21 W. Steinchen, L. X. Yang, M. Schuth, G. Kupfer, *Digitale Shearographie in der Praxis*, F & M Feinwerktechnik Mikrotechnik Messtechnik, Vol. 103, No. 6 (Juni 1995), pp. 342-346.
- 22 S. Naasner, K.-P. Gründer, G. Wernicke, *Untersuchungen zur Genauigkeit des sherographischen Prüfverhaltens*, In: Laser in Research and Engineering, Proc. of the 12th International Congress LASER 95, W. Waidelich et al. (eds.), Springer-Verlag Berlin (etc.), 1996, pp. 494-498.
- 23 Y. Y. Hung, *Automated Shearography for Nondestructive Evaluation and Strain Measurement*, Proc. SPIE Vol. 2455: Nondestructive Evaluation of Aging Aircraft, Airports, Aerospace Hardware, and Materials, ed. T. M. Cordell, R. D. Rempt, Oakland (1995), pp. 238-249.
- 24 W. Steinchen, L. X. Yang, G. Kupfer, *Vibration analysis by digital shearography*, Proc. SPIE Vol. 2868 Second International Conference on Vibration Measurements by Laser Techniques: Advances and Applications (1996), Ed. E. P. Tomasini, pp. 426-437.
- 25 G. Pedrini, Y.-L. Zou, H. J. Tiziani, *Quantitative evaluation of digital shearing interferogram using the spatial carrier method*, Pure and Applied Optics, Vol. 5 (1996), No. 3, pp. 313-321.
- 26 J. W. Newman, *Real Time Shearography as a Means for Tire Manufacturing Process Control*, Meeting of the Rubber Division of the American chemical Society, Vol. 152 (1997), Paper No. 118.

- 27 T. Walz, A. Ettemeyer, *Automatic Shearography System for Helicopter Rotor Blades*, Proc. SPIE Vol. 3397 Nondestructive evaluation of aging aircraft, airports, and aerospace hardware II (1998), Eds. G. A. Geithman, G. E. Georgeson, pp. 187-192.
- 28 T. Walz, *Shearography for nondestructive inspection*, Workshop on New Developments in Shearography, 20 Jan. 1999, EMPA Dübendorf.
- Chapter 2 29 K. J. Gasvik, *Optical metrology*, 2<sup>nd</sup> ed., Chichester (etc.): Wiley, 1995.
- 30 M. Born, E. Wolf, *Principles of optics*, 6<sup>th</sup> ed., Oxford (etc.): Pergamon Press, 1993.
- 31 S. Brem, *Entwicklung eines Shearographie-Kopfes*, Internal Report, Institut für Konstruktion und Bauweisen, 1998.
- 32 J. W. Goodman, *Statistical Properties of Laser Speckle Patterns*, in: [35].
- 33 P. Jacquot, private communication.
- 34 A. E. Ennos, *Speckle Interferometry*, in: [35].
- 35 J. C. Dainty, *Laser speckle and related phenomena*, Springer, Berlin a.o., 2<sup>nd</sup> edition 1984, (Topics in applied physics, vol.9).
- 36 M. Lehmann, *Statistical theory of two-wave speckle interferometry and its application to the optimization of deformation measurements*, These, Sciences techniques, EPF Lausanne, No 1797, 1998, Departement de genie civil, Lausanne, 1998.
- 37 C. Joenathan, *Speckle Photography, Shearography, and ESPI*, Chapter 6 in [38].
- 38 P. K. Rastogi (ed.), *Optical measurement techniques and applications*, Artech House, Boston (etc.), 1997.
- 39 Y. Y. Hung, C. Y. Liang, *Image-Shearing Camera for direct Measurement of Surface Strains*, Applied Optics, Vol. 18 (1979), No. 7, pp. 1046-1051.
- 40 Y. Y. Hung, R. E. Rowlands, I. M. Daniel, *Speckle-Shearing Interferometric Technique: a Full-Field Strain Gauge*, Applied Optics, Vol. 14, No. 3, (March 1975), pp. 618-622.
- 41 M. Schuth, *Aufbau und Anwendung der Shearografie als praxisgerechtes, optisches Prüf- und Messverfahren zur Dehnungsanalyse, Qualitätssicherung und Bauteiloptimierung*, Fortschritt-Berichte VDI, Reihe 8, Mess-, Steuerungs- und Regelungstechnik, Nr. 539, Düsseldorf, VDI Verlag, 1996, Diss., Univ. Gesamthochschule Kassel.
- 42 H. Aebischer, internal report.
- 43 S. Waldner, H. Aebischer, *Report on Task 230: "Measurement Analysis and Validity"*, Pulsed Digital Holography and Shearography, Brite EuRAM Project BRPR-CT96-0152.
- 44 H. A. Aebischer, P. Rechsteiner, *Theoretical Prediction of the Effect of Shear Distortion in the Michelson Interferometer*, Pure and Applied Optics, Vol. 6 (1997), pp. 303-308.
- 45 S. P. Timoshenko, J. N. Goodier, *Theory of elasticity*, 3<sup>rd</sup> ed., Auckland (etc.), McGraw-Hill Book, 1970.
- Chapter 3 46 K. Creath, *Temporal Phase Measurement Methods*, Chapter 4 in: [47]
- 47 D. W. Robinson, G. T. Reid (eds.), *Interferogram Analysis, Digital Fringe Pattern Measurement Techniques*, Bristol (etc.), Institute of Physics Publishing, 1993.

- 48 C. Joenathan, *Phase-measuring interferometry: new methods and error analysis*, Applied Optics, Vol. 33 (1994), No. 19, pp. 4147-4155.
- 49 Th. Kreis, J. Geldmacher, W. Jüptner, *Phasenschiebe-Verfahren in der interferometrischen Messtechnik: ein Vergleich*, Laser in der Technik: Vorträge des 11. Internationalen Kongresses Laser 93, Springer, Berlin (1994), pp. 119-126.
- 50 M. Takeda, I. Hideki, A. Kobayashi, *Fourier-transform method of fringe-pattern analysis for computer-based topography and interferometry*, Journal of the Optical Society of America A, Vol. 72 (1982), pp. 156-160.
- 51 A. Sibilia: *Shearographie für dynamische Messungen*, Diplomarbeit am Institut für Konstruktion und Bauweisen, ETH Zürich (1997).
- 52 M. Vaz, S. Gomes et al., *Report on Task 226: "Basic Image Processing"*, Pulsed Digital Holography and Shearography, Brite EuRAM Project BRPR-CT96-0152.
- 53 M. Kujawinska, *Spatial Phase Measurement Methods*, Chapter 5 in: [47].
- 54 A. L. Weijers, H. van Brug, H. J. Frankena, *Real-time phase-stepped shearing speckle interferometer for non destructive testing*, Fringe '97: proceedings of the 3rd International Workshop on Automatic Processing of Fringe Patterns, Bremen, Germany, September 15-17, 1997, ed. by Werner Jueptner, Wolfgang Osten, Berlin : Akadaemie-Verlag, cop. 1997.
- 55 X. Colonna De Lega, *Processing of non-stationary interference patterns, adapted phase-shifting algorithms and wavelet analysis, application to dynamic deformation measurements by holographic and speckle interferometry*, These, Sciences techniques, EPF Lausanne, No 1666, 1997, Departement de genie civil.
- 56 X. Colonna de Lega, P. Jacquot, *Deformation measurement with object-induced dynamic phase shifting*, Applied Optics, Vol. 35, No. 25, 1 Sept. 1996, pp. 5115-21.
- 57 X. Colonna de Lega, *Contiuous deformation measurement using dynamic phase-shifting and wavelet transforms*, Applied Optics and Optoelectronics 1996, Proceedings of the Applied Optics Divisional Conference of the Institute of Physics, held at Reading, 16-19 September 1996, ed. by K. T. V. Grattan, Bristol (etc.), Institute of Physics Publ., pp. 261-267.
- 58 J. M. Huntley, H. Saldner, *Temporal phase-unwrapping algorithm for automated interferogram analysis*, Applied Optics, Vol. 32 (1993), No. 17, pp. 3047-3052.
- 59 C. Joenathan, B. Franze, P. Haible, H. J. Tiziani, *Speckle interferometry with temporal phase evaluation for measuring large-object deformation*, Applied Optics, Vol. 37, No. 13, 1 May 1998, pp. 2608-14.
- 60 C. Joenathan, B. Franze, P. Haible, H. J. Tiziani, *Large in-plane Displacement Measurement in Dual-beam Speckle Interferometry using Temporal Phase Measurement*, Journal of Modern Optics, Vol. 45, No. 9, Sep. 1998, pp. 1975-84.
- 61 C. Joenathan, B. Franze, P. Haible, H. J. Tiziani, *Novel temporal Fourier transform speckle pattern shearing interferometer*, Optical Engineering. Vol. 37, No. 6, June 1998, pp. 1790-5.
- Chapter 4 62 H. A. Aebischer, S. Waldner, *A simple and effective method for filtering speckle-interferometric phase fringe patterns*, Optics Communications, Vol. 162, No. 4-6, April 1999, pp. 205-210.



- 63 G. H. Kaufmann, A. Davila, D. Kerr, *Speckle noise reduction in TV Holography*, in: D Malacara-Hernandez/S E Acosta/R Rodriguez-Vera/Z Malacara/A A Morales (eds.), Second Iberoamerican Meeting on Optics, Proc. SPIE Vol. 2730 (1995), pp. 96-100.
- 64 B. P. Pfister, *Speckleinterferometrie mit neuen Phasenschiebemethoden*, Berichte aus dem Institut für Technische Optik der Universität Stuttgart 18, Ph.D. thesis, Stuttgart, 1993.
- 65 D. W. Robinson, *Unwrapping Methods*, Chapter 6 in [47].
- 66 W. Osten, W. Jüptner, *Digital Processing of Fringe Patterns in Optical Metrology*, Chapter 3 in [38].
- 67 J. Strand, T. Taxt, *Performance Evaluation of Two-Dimensional Phase Unwrapping Algorithms*, Applied Optics, Vol. 38, No. 20, pp. 4333-4344.
- Chapter 5 68 S. Waldner, *Removing the Image-Doubling in Shearography by Reconstruction of the Displacement Field*, Optics Communications, Vol. 127 (1 June 1996), pp. 117-126.
- 69 S. Waldner, *Removing the Image-Doubling in Shearography – Theory and Application*, SPIE Vol. 2944, Nondestructive Evaluation of Materials and Composites (1996), pp. 247-254.
- 70 H. M. Shang, F. S. Chau, C. J. Tay, S. L. Toh, *Interpretation of holographic and shearographic fringes for estimating the size and depth of debonds in laminated plates*, SPIE Vol. 1554B, Moiré Techniques, Holographic Interferometry, Optical NDT, and Applications to Fluid Mechanics (1991), pp. 680-691.
- 71 J. N. Petzing, J. R. Tyrer, *In-plane Electronic Speckle Pattern Shearing Interferometry: A theoretical analysis supported with experimental results*, SPIE Vol. 2342, Interferometry '94, Photomechanics (1994), pp. 27-36.
- 72 P. A. Klumpp, E. Schnack, *Shearograms with variable measurement sensitivity*, Experimental Techniques Vol 14, July/August 1990, pp. 42-44.
- 73 N. Krishna Mohan, P. J. Masalkar, R. S. Sirohi, *Electronic speckle pattern interferometry with holo-optical element*, SPIE Vol. 1821, Industrial Applications of Optical Inspection, Metrology, and Sensing (1992), pp. 234-242.
- 74 T. W. Ng, F. S. Chau, *Statistical properties of phase variation in shearing speckle interferometry and its effect on fringe visibility*, Journal of Modern Optics (Optica Acta), Vol. 39 (1992), No. 12, pp. 2463-2469.
- 75 B. Schulz, *Electronic-Speckle-Pattern-Interferometrie through Shearography*, Proc. SPIE Vol. 2358, Vibration Measurements (1994), pp. 153-157.
- 76 S. Timoshenko, S. Woinowsky-Krieger, *Theory of plates and shells*, Second ed., New York (etc.): McGraw-Hill, (Reissued 1987).
- 77 T. Lamarque, *Caracterisation de delaminages par interferometrie de speckle a cisaillement avec sollicitation thermique ou mecanique*, Note technique/ONERA NT 1998-11, Chatillon, 1998.
- 78 A. A. M. Maas, P. A. A. M. Somers, *Two-dimensional Deconvolution applied to Phase-stepped Shearography*, Optics and Lasers in Engineering, Vol. 26, No. 4-5, pp. 351-360, 1997.
- Chapter 6 79 J. W. Newman, *Shearographic Inspection of Aircraft Structure*, Materials Evaluation, Vol. 49 (1991), No. 9, pp. 1106-1109.

- 80 A. Ettemeyer, *Zerstörungsfreie Werkstoffprüfung mit TV-Shearografie*, tm – Technisches Messen, Vol. 60 (1993), No. 7/8, pp. 274-277.
- 81 W. Steinchen, L. X. Yang, M. Schuth, G. Kupfer, *Electronic Shearography (ESPSI) for direct measurement of strains*, SPIE Vol. 2248 Optical Measurements and Sensors for the Process Industry (1994), pp. 210-221.
- 82 K. Creath, *Phase-shifting speckle interferometry*, Applied Optics, Vol. 24 (1985), No. 18, pp. 3053-3058.
- 83 T. Flemming, *Vergleich der mechanischen Eigenschaften und des Umformverhaltens zwischen gerichteten kurz- und langfaserverstärkten Thermoplasten*, Dissertation, Technische Universität München (1994).
- 84 T. Flemming, M. Hertwig, G. Kress, *Speckle Interferometry as a Tool for Verifying FEM-Damage Models*, SPIE Vol. 2342 Photomechanics, Interferometry '94 (1994), pp. 304-313.
- Chapter 7 85 R. Kästle, *Multi-wavelength shearography for two-dimensional strain analysis*, Workshop on New Developments in Shearography, 20 Jan. 1999, EMPA Dübendorf.
- 86 T. Siebert, *Simultaneous Measurement of two Shear Directions*, Workshop on New Developments in Shearography, 20 Jan. 1999, EMPA Dübendorf.
- 87 G. Dymny, M. Kujawinska, S. Waldner, *Modified electronic speckle pattern shearing interferometry for simultaneous derivative map measurements*, SPIE Vol. 3098, European Symposium on Lasers and Optics in Manufacturing (1997), pp. 204-210.
- 88 H. A. Aebischer, P. Rechsteiner, *Theoretical Prediction of the Effect of Shear Distortion in the Michelson Interferometer*, Pure and Applied Optics, Vol. 6 (1997), pp. 303-308.
- Chapter 8 89 M. Hertwig, *Development of new speckle-interferometric measurement methods and construction of according measurement devices*, Zürich, (1998), Diss. Techn. Wiss. ETH Zürich, Nr. 12475.
- 90 *TV-Shearography Non-destructive Testing*, Technical documentation, Steinbichler Optotechnik GmbH, May 1995.
- 91 *Electronic Shearography in a New Light*, Intelligent Systems Center, University of Missouri-Rolla, (<http://www.isc.umn.edu/information/equip/shearography.html>).
- Chapter 9 92 R. E. Peterson, *Stress concentration factors: charts and relations useful in making strength calculations for machine parts and structural elements*, New York (etc.), Wiley, (1974).
- 93 L. Yang, *Grundlagen und Anwendungen der Phasenschiebe-Shearografie zur zerstörungsfreien Werkstoffprüfung, Dehnungsmessung und Schwingungsanalyse*, Fortschritt-Berichte VDI, Reihe 8, Mess-, Steuerungs- und Regelungstechnik, Nr. 682, Düsseldorf, VDI Verlag, 1998, Diss., Univ. Gesamthochschule Kassel.
- Chapter 10 94 L. S. Wang, K. Jambunathan, B. N. Dobbins, Shi Ping He, *Measurement of three-dimensional surface shape and deformations using phase stepping speckle interferometry*, Optical Engineering, Vol. 35, No. 8 (1996), pp. 2333-40.
- 95 Niansheng Qi, S. F. Fulghum, R. R. Prasad, M. Krishnan, *Space and time resolved electron density and current measurements in a dense plasma focus Z-pinch*, IEEE Transactions on Plasma Science, Vol. 26, No. 4 (1998), pp. 1127-1137.

# CURRICULUM VITAE

Stephan Peter WALDNER

Citizen of Basel and Oberdorf (BL), Switzerland  
Date of Birth December 11, 1967

## Education and working positions

- 1974-1986 Schools in Basel.
- 1986 Maturität Typus B, Gymnasium am Kohlenberg, Basel.
- 1986-1991 Study of Mechanical Engineering at the Swiss Federal Institute of Technology Zurich (ETH Zürich), specialization in Mechanics/Robotics and Biomedical Engineering.
- 1991 Diploma in Mechanical Engineering, ETH Zürich, "Evaluation of a Computer-Controlled Flow Model for Ultrasonic Blood-Flow Measurement".
- 1992 Sulzer-Burckhardt, Basel, investigation of gas-pulsations in high-pressure compressor plants, mechanical calculations.
- 1992-1993 Warsaw University of Technology (Politechnika Warszawska), Institute for Biomedical Engineering, "Development of a Simulation Tool for the Ultrasonic Doppler Signal Resulting from Fetal Activity".
- 1994-1999 ETH Zürich, Institute for Design and Construction Methods, scientific employee and Ph.D. student, "Deformation Measurement with Speckle Interferometry and Shearography", acquisition, definition, and management of research projects, coaching of mechanical engineering students in the subject "Product Design".

## Important Publications

- 1 H. A. Aebischer, S. Waldner, *A simple and effective method for filtering speckle-interferometric phase fringe patterns*, Optics Communications, Vol. 162 (April 1999), pp. 205-210.
- 2 G. Dymny, M. Kujawska, S. Waldner, *Modified electronic speckle pattern shearing interferometry for simultaneous derivative map measurements*, European Symposium on Lasers and Optics in Manufacturing, 16-20 June 1997, Munich, Germany, SPIE Proceedings Series, Volume 3098, pp. 204-210.
- 3 S. Waldner, *Removing the Image-Doubling in Shearography – Theory and Application*, Nondestructive Evaluation of Materials and Composites, 3-5 December 1996, Scottsdale, Arizona, Editors: S. Doctor, C. A. Leibowitz, G. Y. Baaklini, SPIE Proceedings Series, Volume 2944, pp. 247-254.

- 4 S. Waldner, *Removing the Image-Doubling in Shearography by Reconstruction of the Displacement Field*, Optics Communications, Vol. 127 (1 June 1996), pp. 117-126.
- 5 H. A. Aebischer & S. Waldner, *Strain Distributions Made Visible with Image-Shearing Speckle Pattern Interferometry*, Optics and Lasers in Engineering, Vol. 26, Nos. 4-5, Special issue on Speckle and Speckle Shearing Interferometry - II, March 1997, pp. 407-420.
- 6 K. Kaluzynski, S. Waldner, T. Palko, *Simulation Tool for the Ultrasonic Doppler Signal Resulting from Fetal Activity*, 4<sup>th</sup> European Conference on Engineering and Medicine (Bridging East and West), Warsaw, Poland, May 25-28, 1997 (European Society for Engineering and Medicine).

# LIST OF IMPORTED FIGURES

Figure 1.1	../Introduction/strain gauge.tif @ 600 dpi	1
	../Introduction/BAe04.tif @ 300 dpi	2
	../Introduction/BAe03.tif @ 300 dpi	2
Figure 1.3	../Introduction/INES04PMa.tif @ 300 dpi	3
Figure 1.4	../Introduction/Diagramm Quanti Shear E.eps	7
Figure 2.1	../Theory/general interferometer gasvik.eps	11
Figure 2.2	../Theory/classic michelson.eps	12
Figure 2.3	../Theory/sphere.tif @ 200 dpi	13
Figure 2.4	../Theory/sphcut.eps	13
Figure 2.5	../Theory/speckle interferometer.eps	14
Figure 2.6	../Theory/Intens.tif @ 150 dpi	15
Figure 2.7	../Theory/Corrello.tif @ 150 dpi	16
Figure 2.8	../Theory/speckle interferometer oop.eps	17
Figure 2.9	../Theory/speckle interferometer ip.eps	17
Figure 2.10	../Theory/michelson shear.eps	18
Figure 2.11	../Theory/michelson.eps	19
Figure 2.12	../Theory/reference state 3.eps	20
Figure 2.13	../Theory/deformed state 3.eps	21
Figure 2.14	../Theory/strain element.eps	23
Figure 3.1	../Phase Determination/temporal phase shifting.eps	28
Figure 3.2	../Phase Determination/CPHASE1.tif @ 150 dpi	29
Figure 3.3	../Phase Determination/tilted wave front.eps	30
Figure 3.4	../Phase Determination/fft flow3.eps	31
Figure 3.5	../Phase Determination/CARRIER.tif @ 200 dpi	32
Figure 3.6	../Phase Determination/dynamic phase shifting.eps	33
	../Phase Determination/addsubcurves.eps	34
Figure 4.1	../Filtering/diagramm sincos 2.eps	36
Figure 4.2	../Filtering/tefshrt5.tif @ 150 dpi	38
	../Filtering/tef5f3_2.tif @ 150 dpi	38
	../Filtering/tef5f15.tif @ 150 dpi	38
	../Filtering/tscsp25.tif @ 150 dpi	39
	../Filtering/tef5pf52g.tif @ 150 dpi	39
	../Filtering/tef5ff.tif @ 150 dpi	40
	../Filtering/tef5f3_2.tif @ 300 dpi	40
	../Filtering/unwrapping.eps	42
Figure 4.7	../Filtering/tef5ffu.tif @ 150 dpi	43
Figure 5.1	../unshear/coordinates.eps	46
Figure 5.2	../unshear/unshear curves.eps	47
	../unshear/unshear program.eps	49
Figure 5.4	../unshear/undeformed area.eps	50
Figure 5.5	../unshear/stsheard.tif @ 200 dpi	51
Figure 5.6	../unshear/sheared.tif @ 75 dpi	51
Figure 5.7	../unshear/isheared.tif @ 75 dpi	52
Figure 5.8	../unshear/unshear3.tif @ 200 dpi	52

Figure 5.9	../unshear/OU SH02P9.tif @ 150 dpi	53
Figure 5.10	../unshear/OU SH02U2.tif @ 150 dpi	53
Figure 5.11	../unshear/OU ES01O.tif @ 150 dpi	54
Figure 5.12	../unshear/epishearcompar.eps	54
Figure 6.1	../Isolation/shear3d.eps	59
Figure 6.2	../Isolation/shsymbelebwe.eps	61
Figure 6.3	../Isolation/SHBRSR08.tif @ 150 dpi	63
Figure 6.4	../Isolation/SHBLSR08.tif @ 150 dpi	63
Figure 6.5	../Isolation/SHSRSU08.tif @ 150 dpi	64
Figure 6.6	../Isolation/strainx1.tif @ 150 dpi	64
Figure 6.7	../Isolation/SHSRAD08.tif @ 150 dpi	64
Figure 6.8	../Isolation/SHLPSU17.tif @ 150 dpi	65
Figure 6.9	../Isolation/strainy1.tif @ 150 dpi	65
Figure 7.1	../Quantitative Evaluation/measurement strategy.eps	68
Figure 7.2	../Quantitative Evaluation/Evaluation procedure.eps	71
Figure 7.3	../Quantitative Evaluation/nonintegershear.eps	75
Figure 8.1	../Equipment/observation.eps	78
Figure 8.2	../Equipment/optocat.tif @ 150 dpi	79
Figure 8.3	../Equipment/promove.tif @ 150 dpi	80
Figure 8.4	../Equipment/tensile.tif @ 300 dpi	81
	../Equipment/ettemeyer.tif @ 150 dpi	83
	../Equipment/steinbichler.tif @ 150 dpi	83
	../Equipment/lti_shearocam.tif @ 150 dpi	83
	../Equipment/shhead_ohne2.tif @ 150 dpi	85
Figure 8.7	../Equipment/illumination_cut.tif @ 300 dpi	87
Figure 8.8	../Equipment/shearotronic.tif @ 150 dpi	87
Figure 8.9	../Equipment/Circuit.eps	88
Figure 8.10	../Equipment/onedeehead.tif @ 150 dpi	89
Figure 8.11	../Equipment/threedeehead.tif @ 150 dpi	89
	../Equipment/screenshot2.tif @ 150 dpi	90
Figure 9.1	../Strain Measurement/inter99add.tif @ 150 dpi	94
Figure 9.2	../Strain Measurement/inter99curves.eps	94
	../Strain Measurement/tensile sample.eps	95
Figure 9.4	../Strain Measurement/zwickmeasurelandsc.tif @ 150 dpi	96
Figure 9.5	../Strain Measurement/i15_snap.tif @ 150 dpi	97
	../Strain Measurement/p7u2.tif @ 150 dpi	98
	../Strain Measurement/p7v2.tif @ 150 dpi	98
	../New Strain Measurements/ns2strainxx2s.tif @ 150 dpi	99
	../New Strain Measurements/ns2strainyy2s.tif @ 150 dpi	99
	../New Strain Measurements/ns2strainxy2s.tif @ 150 dpi	99
Figure 9.8	../Quantitative Evaluation/Evaluation procedure.eps	100
Figure 9.9	../Strain Measurement/i19_pfp.tif @ 236 dpi	100
	../Strain Measurement/i19_add01.tif @ 236 dpi	101
	../Strain Measurement/i19_add02.tif @ 236 dpi	101
	../Strain Measurement/i19_add03.tif @ 236 dpi	101
	../Strain Measurement/i19_add01u.tif @ 236 dpi	101
	../Strain Measurement/i19_add02u.tif @ 236 dpi	101
	../Strain Measurement/i19_add03u.tif @ 236 dpi	101
	../Strain Measurement/i19_ddxp.tif @ 236 dpi	102

	../Strain Measurement/i19_ddyp.tif @ 236 dpi	102
	../Strain Measurement/i19_ddzp.tif @ 236 dpi	102
	../Strain Measurement/i19_u1.tif @ 236 dpi	103
	../Strain Measurement/i19_v1.tif @ 236 dpi	103
	../Strain Measurement/i19_w1.tif @ 236 dpi	103
	../Strain Measurement/p7u2.tif @ 190 dpi	103
	../Strain Measurement/p7v2.tif @ 190 dpi	103
Figure 9.14	../Strain Measurement/uvwdrawing2.eps	104
	../New Strain Measurements/ns2strainyy2s.tif @ 190 dpi	105
	../Strain Measurement/i19_epsx.tif @ 236 dpi	105
	../Strain Measurement/i19_epsy.tif @ 236 dpi	105
	../New Strain Measurements/ns2strainxx2s.tif @ 190 dpi	105
Figure 9.16	../New Strain Measurements/i19_epsxplot.eps	105
	../Strain Measurement/i19_dudy2.tif @ 236 dpi	106
	../Strain Measurement/i19_dvdx2.tif @ 236 dpi	106
	../Strain Measurement/i19_gammaxy.tif @ 236 dpi	106
	../New Strain Measurements/ns2strainxy2s.tif @ 190 dpi	106
	../Strain Measurement/i19_dudx.tif @ 236 dpi	108
	../Strain Measurement/i19_dvdx.tif @ 236 dpi	108
	../Strain Measurement/i19_dwdx.tif @ 236 dpi	108
	../Conventional/pyra2.tif @ 150 dpi	110
	../Conventional/fpyra2.tif @ 150 dpi	110
	../Conventional/B64O03.tif @ 150 dpi	111
	../Conventional/B64OU03.tif @ 150 dpi	111